Diffractive Photoproduction of High p_T Photons at HERA

Matthew Beckingham

December 2004

THE UNIVERSITY *of* MANCHESTER

High Energy Group
Department of Physics and Astronomy

A thesis submitted to The University of Manchester for the degree of Doctor of Philosophy in the Faculty of Science and Engineering

Contents

Abstract

The process $\gamma p \to \gamma Y$, in which the outgoing photon has transverse momentum $p_T^\gamma > 2$ GeV and there is a large rapidity gap between the proton dissociative system Y and the outgoing photon, is studied, using the H1 detector at HERA, for the first time. The measurement is based on 47.6 pb^{-1} of data collected in the 1999–2000 running period. Cross sections are measured differentially in the squared four momentum transfer at the proton vertex, $t \simeq -(p_T^\gamma)^2$, and $x_{I\!P} = (E + p_z)_\gamma / 2E_p$, where E_p is the incoming proton energy. All cross sections are consistent with a perturbative QCD model calculated using the leading logarithmic approximation of BFKL. A fit of the form $A(1/W^2)(1/x_{I\!P})^n$ performed on the $x_{I\!P}$ cross section yields a pomeron intercept of $\alpha(0) = 1.50 \pm 0.12(\text{stat.}) \pm 0.01(\text{sys.})$ and a fit of the form $A\,|t|^{-n}$ performed on the t cross section yields $n = 2.14 \pm 0.41(\text{stat.}) \pm 0.22(\text{sys.})$.

No portion of the work referred to in this thesis has been submitted in support of an application for another degree or qualification of this or any other university or other institute of learning.

This work was supported financially by the Particle Physics and Astronomy Research Council (PPARC) between October 2000 and September 2003.

For Mum, Dad and Lynsey

Chapter 1

Introduction

Of the three forces in the Standard Model of particle physics the strong force is perhaps the least understood, despite successfully describing a large quantity of experimental data. The strong interaction is contrary to the other two interactions, the electromagnetic and weak interactions, in that the coupling constant, α_s, increases in strength with distance. This leads to the concept of confinement – the observation that free quarks and gluons are not seen experimentally. At short interaction distances, corresponding to energies larger than the QCD energy scale, Λ_{QCD}, α_s is small enough to allow perturbative QCD (pQCD) calculations to be made. Calculations with such a hard scale have been extremely successful in describing short distance physics. However total cross sections are dominated by long distance, soft processes meaning that perturbative QCD calculations cannot be made.

Soft hadronic cross sections are however described by Regge theory, a model based on general assumptions of the scattering process with no need for the underlying dynamics to be known. Thus there is the undesirable position that two different models describe the strong interaction in two different regions of phase space. Since QCD describes the underlying dynamics of the strong interaction it should be able to describe interactions within the Regge picture.

Within Regge theory the high energy total cross section is mainly due to the exchange of a strongly interacting colour singlet object with vacuum quantum numbers called the pomeron. The exchange of a pomeron manifests itself with the classic signature of a diffractive exchange – a large region of rapidity between the scattered particles in the final state with no hadronic activity, known as a rapidity gap. The observation of such rapidity gap events in DIS ep collisions at HERA reinvigorated interest in diffraction and the pomeron. The unique nature of the ep collider means that the point-like electron can be used to probe the structure of the pomeron, much like the proton structure is probed in inclusive ep interactions. Additionally the presence of a hard scale due to the high virtuality of the photon, Q^2, that interacts between the electron and the pomeron means that perturbative calculations can be made. Thus by understanding the pomeron within QCD, steps may be made towards understanding the Regge regime within QCD.

Aside from Q^2, both the mass of any vector meson diffractively produced and the four momentum transfer of the diffractive exchange, t, may provide the hard scales to allow pQCD calculations to be made. Previous measurements have been made of diffractive vector meson production where the mass is large enough to give a hard scale, for instance the J/ψ. The rapidity gap between high-p_T jets in dijet events and high t diffractive vector meson production have been measured where the hard scale comes from the large t, as well as the mass in the vector meson case.

The process $\gamma p \to \gamma Y$, where the final state photon carries a large transverse momentum and is well separated from the proton dissociative system, is a uniquely clean process to study diffraction with such a hard scale. By requiring the photon to have a large transverse momentum, $(p_T^\gamma)^2 \simeq -t \gg \Lambda_{QCD}^2$, a hard scale is present and pQCD calculations may be made. Unlike other exclusive diffractive processes, only a single photon is diffractively produced in the final state, meaning that measurements can be made to larger rapidity gaps. Additionally, subsequent soft hadronic interactions between the dissociated proton and the photon are minimised, as the photon is an electromagnetically interacting particle. Finally the theoretical calculation of the process is simplified by the absence of a vector meson wavefunction. Hence the hard scatter can be completely calculated and the only non-perturbative element of the cross section occurs from the well known parton density functions of the proton. This thesis presents the first measurement of this interesting process at HERA.

The following chapters of this thesis begin with a description of the H1 detector and the HERA accelerator in chapter 2, focusing on the parts of the detector used in this analysis. Chapter 3 presents an overview of the proton structure physics observed at the HERA accelerator. Chapter 4 gives an overview of diffractive physics leading to the measurement presented in this thesis. The reconstruction of data and event selection are presented in chapter 5. Chapter 6 shows the steps taken to produce the final cross sections, which are presented and discussed in chapter 7. Finally, conclusions are drawn in chapter 8.

Chapter 2

The H1 Experiment at HERA

The H1 detector [1] is one of two experiments that studies the collisions of electrons and protons in the HERA[1] accelerator at the DESY[2] laboratory in Hamburg, Germany. This chapter begins by describing HERA and giving an overview of H1. Subsequent sections then describe components of the H1 detector – the calorimetry, tracking detectors, muon detectors, time of flight systems and the luminosity system – before describing the trigger and data acquisition system with emphasis on the triggers used in this thesis. Finally the simulation of the detector is described.

2.1 HERA

The HERA accelerator (figure 2.1) is the world's first electron[3]-proton collider. It consists of two 6.3 km circumference storage rings to separately store beams of 27.6 GeV electrons and 920 GeV protons. The two beams are brought together at the northern and southern points of the ring where the H1 and ZEUS detectors are

[1] Hadron-Elektron Ring Anlage

[2] Deutsches Elektronen Synchrotron

[3] HERA uses either electrons or positrons for its operation. In this thesis the beam lepton will be called an electron whether it is an electron or positron.

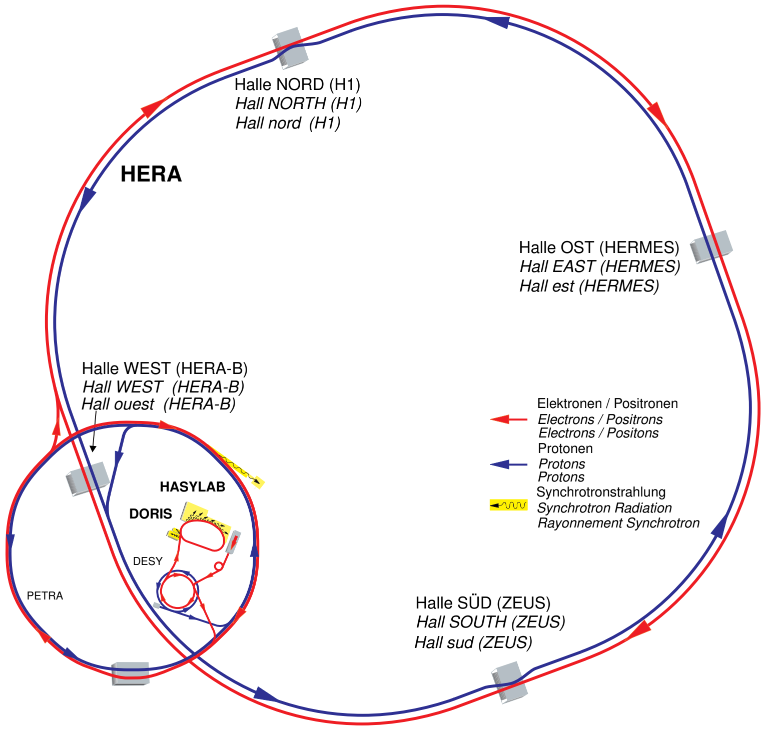

Figure 2.1: A schematic view of the HERA accelerator.

situated, respectively, giving a centre of mass energy of approximately 320 GeV. The two beams are divided into 220 bunches of particles, with a bunch crossing at H1 occurring every 96 ns. However, only 175 of the bunches are collided with bunches from the other beam, the remaining bunches are 'pilot' bunches where the corresponding bunch in the opposite beam is empty. The pilot bunches allow backgrounds from interactions between the beam and any residual gas in the beam pipe (beam-gas) and collisions between the beam and the beam pipe wall (beam-wall) to be studied and their rates estimated.

2.2 The H1 Detector

The main components of the H1 detector are shown in figure 2.2. The H1 detector has dimensions of approximately 12 m $\times$ 10 m $\times$ 15 m and weighs about 2800 tonnes.

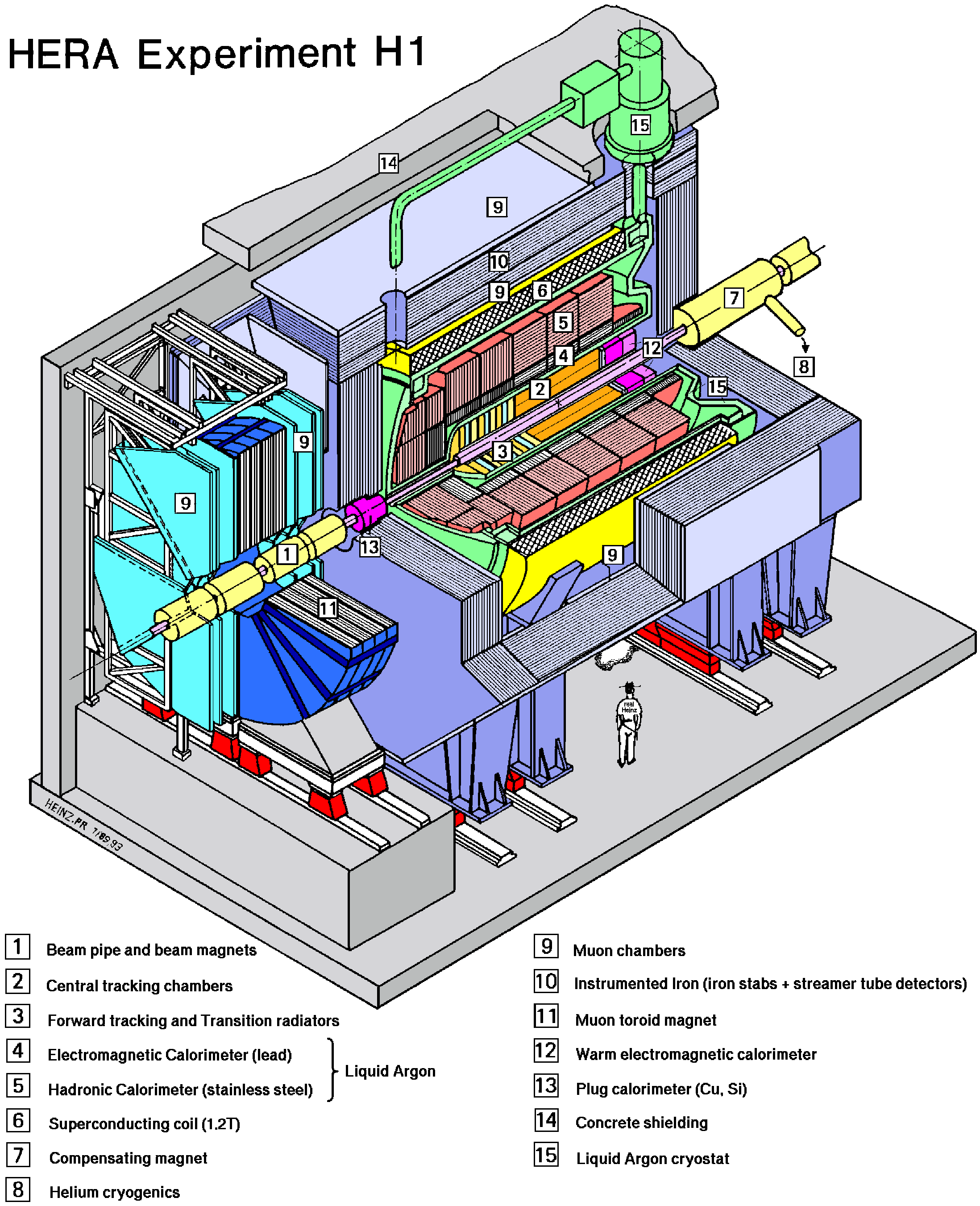

Figure 2.2: A schematic diagram of the H1 Detector.

The interaction point is firstly surrounded by tracking chambers (section 2.3), comprising of the central (CTD), forward (FTD) and silicon trackers, followed by the calorimetry (section 2.4) consisting of the liquid argon, SpaCal and plug calorimeters. Surrounding the calorimeters is a 3m radius superconducting coil that produces a magnetic field of 1.15 T. By placing the coil outside the calorimeters the showering of particles before the calorimeters is reduced, while still providing a magnetic field for the measurement of track momentum in the tracking detectors. The iron return yoke of the magnet (section 2.5.1) is instrumented to allow detection of muons and any hadrons that leak through the hadronic calorimeters. Further detection of muons outside the instrumented iron in the forward direction is provided by the forward muon detector (section 2.5.2). Additional detectors (not shown in figure 2.2) are placed along the beam pipe, in both directions, to detect particles scattered at low angles with respect to the beam axis. Of particular interest to this thesis are the detectors in the electron direction (section 2.7), which allow detection of the scattered electron at very low angles and measurement of the luminosity. Due to the asymmetry of the electron and proton energies the centre of mass system is boosted forwards, giving rise to higher multiplicities in the forward direction. This is reflected in the design of the H1 detector, with extra instrumentation, higher granularity and greater depth of detectors in the forward direction.

A right handed coordinate system (x, y, z) is defined with the nominal interaction point as the origin, the proton direction as the positive z axis, the positive y direction vertically upwards, and the positive x axis pointing towards the centre of the HERA ring. A spherical coordinated system (r, θ, ϕ) is hence defined with $\theta = 0$ along the positive z axis and $\phi = 0$ along the positive x axis. The pseudorapidity, η, of a particle may also be defined as

$$\eta = -\ln \tan\left(\frac{\theta}{2}\right) \tag{2.1}$$

which in the limit that the mass of the particle is zero approximates to the rapidity,

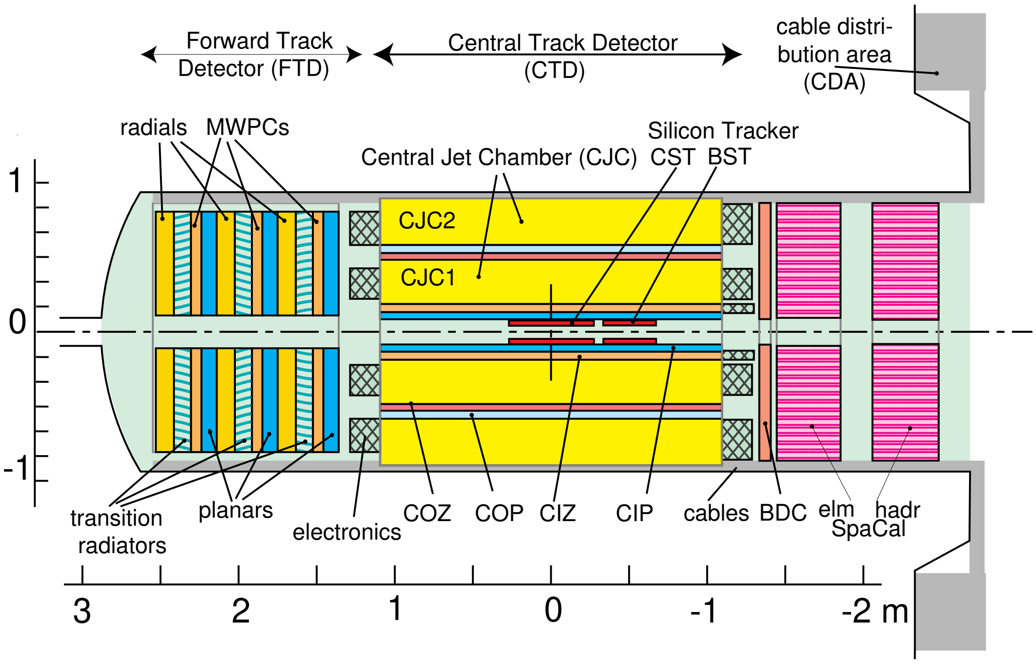

Figure 2.3: A cross sectional view of the H1 Tracking System, showing the central, forward and silicon trackers and the BDC.

Y, given by

$$Y = \frac{1}{2} \ln \left(\frac{E + p_{\parallel}}{E - p_{\parallel}} \right) \tag{2.2}$$

where E is the energy and $p_{\parallel}$ the longitudinal momentum of the particle.

2.3 Tracking

Figure 2.3 shows the tracking detectors used in the H1 experiment. The central track detector consists of two drift chambers, CJC1 and CJC2, with additional drift chambers to measure the z coordinate, the CIZ and COZ, and two multiwire proportional chambers, the CIP and COP. Similarly the forward tracker also consists of drift chambers and multi-wire proportional chambers, but also has layers of transition radiators. Between the central track detector and the beampipe the CST and BST silicon trackers are housed.

Drift chambers are constructed from a series of cells, each of which contain multiple wires and are filled with gas. The cells contain a number of anode sense wires and cathode field wires with additional field shaping wires to ensure a constant electric field throughout the majority of each cell. When a charged particle passes through a drift cell it ionizes some of the gas particles. The resulting ions then drift towards a cathode wire and the electrons towards an anode wire at a constant, known velocity. At distances close to the anode wires the electric field increases giving the drifting electrons enough energy to cause secondary ionization. The subsequent avalanche of electrons causes the original signal to be amplified for readout. From the timing of this pulse and knowledge of the drift time, the distance from the anode wire of the original particle can be found. Typical drift velocities are approximately 50 $\mu \mathrm{ms}^{-1}$ and drift distances are known to $100 - 200$ μm. The movement of the ions also induces a current in the anode wire. From charge division the position of the signal along the wire is also known, although only to an accuracy of 1-2% of the wire length.

Multiwire proportional chambers (MWPC) consist of a series of gas filled cells containing anode wires with cathode pads on the outside of the cell. However, the anode wires are closer together than in drift chambers, with separations of the order of 1 mm, ensuring that the avalanche regions overlap and there are no drift regions. When a charged particle ionizes some of the gas in the chamber an avalanche begins and is read out by a single anode wire. The total charge collected is proportional to the initial ionization. Due to the short drift time, the signal is produced quickly, however the spatial resolution is limited by the separation of the anode wires. For this reason MWPCs are mainly used for fast triggering as opposed to full track reconstruction.

Solid state detectors are made using Group IV elements, in particular silicon.

When a charged particle passes through a layer of Si many electron-hole (e-h) pairs are produced. A lower energy is needed to make an e-h pair (3.6 eV) compared to gas detectors (approximately 30 eV to ionize a gas atom) and the high mobility of the electrons and holes allows for a signal to be read out quickly. However, there is no charge multiplication mechanism, so low noise amplifiers are needed and the number of e-h pairs produced are orders of magnitude smaller than those already present in the intrinsic material. Due to the latter problem Si detectors are doped and depleted by forming a reverse p-n junction.

Doped Si is produced in n and p types by adding elements from adjacent groups into the pure material. Group V elements are added to Si to provide more electrons in the conduction band and make n-type Si. Group III elements are added to Si to produce more holes in the valence band, making p type Si. When brought together electrons and holes diffuse between the n and p type Si, causing a depletion zone with no free charge carriers. By applying a reverse bias voltage the depletion zone extends over the full junction. Thus when a charged particle passes through the p-n junction and creates e-h pairs they are of noticeable quantity, being the only charge carriers. Due to the electric field the electrons drift towards the n-side and the holes towards the p-side, giving a detectable current. By segmenting the p-type Si more accurate position measurements can be made within a single section of the Si detector.

2.3.1 Central Tracking

Figure 2.4 shows a cross sectional view in the r-ϕ plane of the Central Tracking Detector (CTD). The CTD is cylindrical in shape and covers the angular range $15^\circ \leq \theta \leq 165^\circ$. It consists of a series of concentric cylindrical subdetectors. The main subdetectors are the two Central Jet Chambers CJC1 and CJC2. Two thin drift chambers, the Central Inner (CIZ) and Central Outer (COZ) z-chambers, pro-

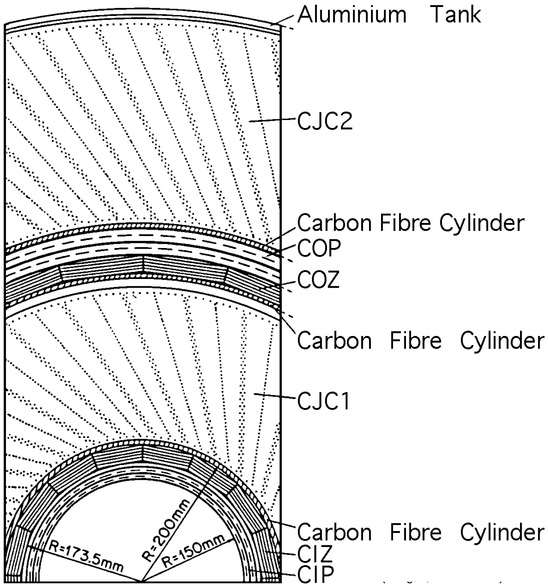

Figure 2.4: A cross sectional view, in the $r-\phi$ plane, of the Central Track Detector.

vide improved measurement of the z coordinate of a track. The CIZ chamber is situated inside the CJC1 and the COZ between the CJC1 and CJC2. Additionally, two multiwire proportional chambers, the Central Inner Proportional chamber (CIP) and the Central Outer Proportional chamber (COP), are situated inside the CJC1 and between the CJC1 and CJC2 respectively. The two concentric drift chambers, CJC1 and CJC2 [2] both have drift wires strung in the z direction to provide the best measurement of tracks in the $r-\phi$ plane. The drift cells are inclined at about 30° to the radial direction to improve the track resolution, as the drift electrons move approximately perpendicularly to high momentum tracks, and ensure that tracks pass through multiple drift chambers to resolve drift time ambiguities. In a single drift cell the position of a track relative to the drift wire is not known, only the distance, leading to such ambiguities. From the drift time of the drift electrons the $r-\phi$ coordinate of the track is measured with a resolution of 170μm. The z coordinate of the track is measured using charge division with a resolution of 2.5cm.

The CIZ and COZ [3] complement the CJC1 and CJC2 by providing improved accuracy for the measurement of the z coordinates of tracks. This is facilitated by having the sense wires perpendicular to the z axis in the $r-\phi$ plane, hence the drift direction is parallel to the z axis. Therefore, by measuring the drift time, the z coordinate is measured with a typical resolution of 300 μm. The combined $r-\phi$ and z measurements of the track trajectory gives a momentum resolution for a single track of $\frac{\sigma(p)}{p^2} \sim 3 \times 10^{-3}$ GeV^{-1}.

The CIP and COP [4] are multiwire proportional chambers that provide triggering over the full solid angle of the CTD. Both chambers consist of double layers of drift cells with sense wires parallel to the z axis. The CIP and COP are not used for offline reconstruction of tracks, but purely for triggering with a response time much faster than the 96 ns bunch crossing interval.

2.3.2 Forward Tracking

The FTD [5], shown in figure 2.3, provides tracking coverage in the region $5^\circ \leq \theta \leq 30^\circ$. It consists of three supermodules, each containing twelve layers of planar drift chambers, a section of MWPC's, transition radiators and twelve layers of radial drift chambers. The planar chambers in each supermodule are split into three layers that contain sense wires in the $r-\phi$ plane. The three layers are oriented at 0°, 60° and -60°, allowing an improved spatial measurement. The radial chambers consist of radial sense wires to provide an accurate measurement of the azimuthal angle, ϕ, from drift time and coarser measurement of the radial coordinate from charge division. The combination of planar and radial chambers ensure a good measurement of the momentum of a track, the single track momentum resolution is $\frac{\sigma(p)}{p^2} < 3 \times 10^{-3}$ GeV^{-1}, and an angular resolution of $\sigma_{\theta,\phi} < 1$mrad.

2.3.3 Backward Drift Chamber

The Backward Drift Chamber (BDC) [6], shown in figure 2.3, is mounted on the front of the SpaCal and hence has a similar acceptance ($153° \leq \theta \leq 177.5°$). The BDC consists of four layers of octagonal shape double drift chambers in the $r - \phi$ plane. The sense wires are strung along the octagonal shape to give a near radial drift direction and hence optimized resolution of the measurement of the polar angle θ. The spacing of the wires decreases with radial distance to provide a uniform resolution in θ of better than 1 mrad.

2.3.4 Silicon Tracking

The Central Silicon Tracker (CST) [7] and Backward Silicon Tracker (BST) [8] are shown in figure 2.3. The CST provides improved vertex information for particles close to the interaction point as well as being able to measure secondary vertices. It consists of two concentric cylindrical layers of silicon sensors with two coordinate readout and covers the angular range $30° \leq \theta \leq 150°$. The $r - \phi$ resolution is 12 μm and the z resolution is 22 μm. The BST provides measurement of particle tracks near to the beampipe in the backward direction. This is particularly useful for measuring the scattered electron when at low angles. The BST consists of eight planes of silicon detector disks in the $r - \phi$ plane. Each disk contains 16 wedge shaped wafers per disk. The BST covers the angular range $162° \leq \theta \leq 176°$.

2.4 Calorimeters

The four calorimeter detectors used in H1, shown in figure 2.5, are the liquid argon (LAr) calorimeter, the SpaCal, the plug and the tail catcher. Only the LAr and SpaCal are used in this thesis and are described in more detail in the remaining

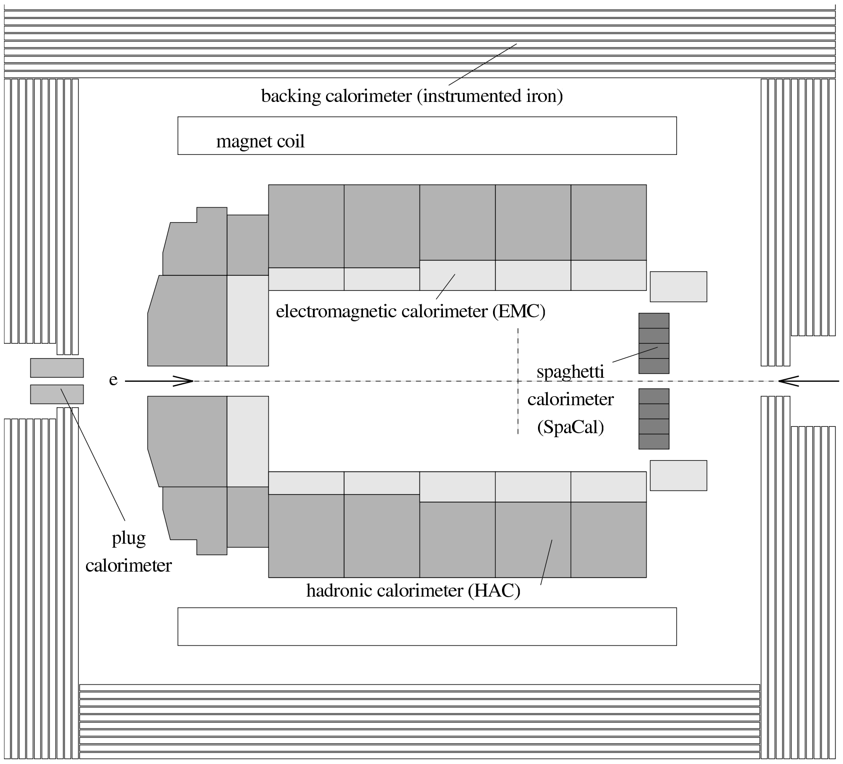

Figure 2.5: A cross sectional view of the H1 calorimetry in the $r - z$ plane

parts of this section. The plug consists of nine copper absorber plates with eight layers of silicon detector interleaved. It was designed to provide detector coverage in the area between the forward LAr calorimeter and the beam pipe in the angular range $0.6° \leq \theta \leq 3.5°$. The tail catcher consists of the eleven of the sixteen layers of limited streamer tubes with pad electrode readout, housed within the instrumented iron of the H1 magnet return yoke. Coverage is provided, over almost the whole H1 solid angle, for coarse measurement of hadronic showers not contained in the more central calorimeters and for the detection of muons.

The four calorimeters used in H1 are sampling calorimeters. Such calorimeters consist of layers of passive absorber material with an active sampling material between the layers. The absorber causes incident particles to lose energy through interactions that produce secondary particles. These particles then similarly interact with the absorber, producing a shower of particles. The sampling material measures the deposited energy from the shower.

Electromagnetically interacting particles (electrons and photons) lose energy through bremsstrahlung while in the electric field of the absorber nuclei ($eA \rightarrow eA\gamma$) and through pair production ($\gamma \rightarrow e^{+}e^{-}$). Subsequent particles undergo the same interactions producing a shower of particles. The number of particles in the shower is proportional to the energy of the incident particle and therefore, if fully contained, the total ionisation measured by the sampling layer is proportional to the energy of the incident particle. The characteristic length of an electromagnetic particle interacting with a material is the radiation length, X_0, which is the mean distance for which the energy of a particle reduces to 1/e of its original value.

Strongly interacting particles lose energy through both elastic and inelastic scattering with nucleons. As with electromagnetic particles, the secondary particles subsequently interact and a shower develops. The shower continues to develop until the energy of secondary hadrons is low enough to be stopped by ionization or nuclear capture. The characteristic length for hadronic showers is the interaction length, λ. This length is typically larger than X_0 and leads to hadronic calorimeters having larger absorbing layers at the expense of a loss of energy resolution.

Due to the different developments of electromagnetic and hadronic showers, different fractions of energy relative to the incident particle energy are detected for hadronic and electromagnetic particles. Most of the hadronic energy in a shower is lost through excitation or break up of nuclei in the absorber. Additionally, the hadronic shower also contains a mix of hadronic and electromagnetic particles, due to electromagnetic decays of neutral pions initiating electromagnetic showers. The response to hadrons is typically $10 - 35\%$ lower than the response to electromagnetic particles. A calorimeter is able to compensate for the difference in response through the design and constituent materials of the calorimeter causing an equal response to hadronic and electromagnetic showers. Alternatively, if a detector has a fine enough granularity, hadronic clusters can be identified and the energy corrected

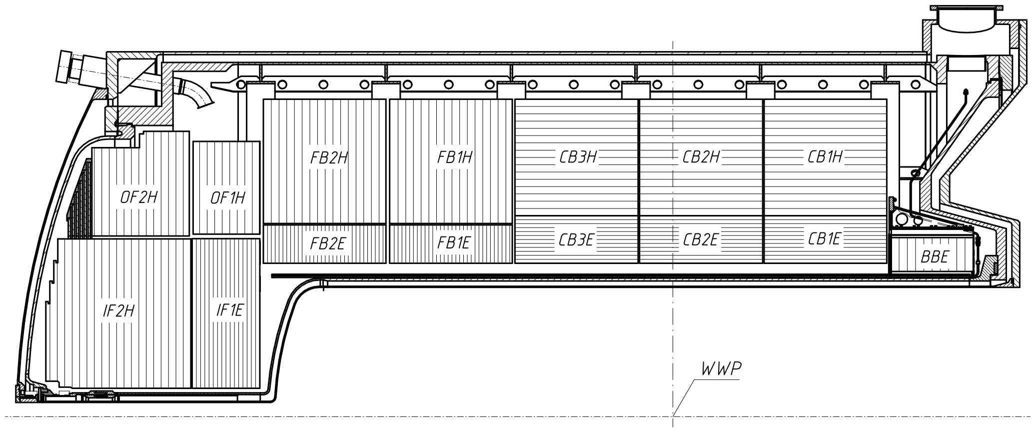

Figure 2.6: A cross sectional view, in the $r-z$ plane, of the liquid argon calorimeter.

during offline reconstruction.

2.4.1 Liquid Argon Calorimeter

The largest of the calorimeters in the H1 detector is the liquid argon (LAr) calorimeter [9]. It main uses are to measure the scattered electron when scattered through a large angle and measurement of the hadronic final state. The LAr calorimeter covers the range $4° \leq \theta \leq 154°$ and the full range of ϕ. The LAr calorimeter consists of two parts, the electromagnetic (EMC) and hadronic (HAC) calorimeters, both of which are housed within the same cryostat. The whole detector is situated within the solenoid magnet, hence the quantity of dead material any particle traverses before entering the LAr calorimeter is reduced. The LAr calorimeter is divided into eight wheels in z (figure 2.6), which are each in turn split into eight identical octants in ϕ. All of the the calorimeter wheels have an electromagnetic and hadronic section, apart from the most backward wheel, called the BBE, which consists of only an electromagnetic section.

Liquid argon is used as the sampling material because the high atomic density leads to high ionization and hence improved sampling of the shower of particles in the calorimeter. Additionally, further inelastic collisions between electrons or ions and the argon atoms are reduced as argon is a noble gas and hence has a high ionization energy. The absorber in the EMC is 2.4 mm thick lead arranged in alternate layers with a similar thickness of liquid argon between. The HAC contains 19 mm steel absorbers with 5 mm liquid argon sampling layers. The charge from the ionized liquid argon atoms is collected by cathode pads and read out through approximately 45 000 read out channels. This provides a fine granularity in the LAr calorimeter which is approximately constant in η and ϕ. The asymmetry of the centre of mass system at HERA is reflected in the thickness of the LAr calorimeter – the thickness of the EMC varies from 30 X_0 in the forward direction to 20 X_0 in the backward direction. Similarly, the HAC varies from 8 λ in the forward direction to 5 λ in the backward direction.

The LAr calorimeter is a non-compensating calorimeter, meaning that the response of the calorimeter is different for electromagnetic particles and hadrons. The charge output from hadrons is approximately 30% less for hadrons than electrons. Corrections to the measured hadronic energy are applied to clusters offline at the reconstruction stage.

The energy resolution of the LAr calorimeter for single particles was measured using test beams. The EMC has a resolution for electrons of $\frac{\sigma_E}{E} = \frac{0.12}{\sqrt{E/\mathrm{GeV}}} \oplus 0.01$ [10]. The energy resolution for pions in the EMC and HAC is $\frac{\sigma_E}{E} = \frac{0.50}{\sqrt{E/\mathrm{GeV}}} \oplus 0.02$ [11].

2.4.2 Spaghetti Calorimeter

The “Spaghetti” calorimeter or SpaCal [12] is shown in Figure 2.7. The detector was designed to provide good measurement of the energy and angle of the scattered electron in DIS events, hence allowing the kinematics of the events to be well reconstructed. Additionally, the SpaCal provides measurements of hadronic activity in the backward region and time of flight information in order to reject background

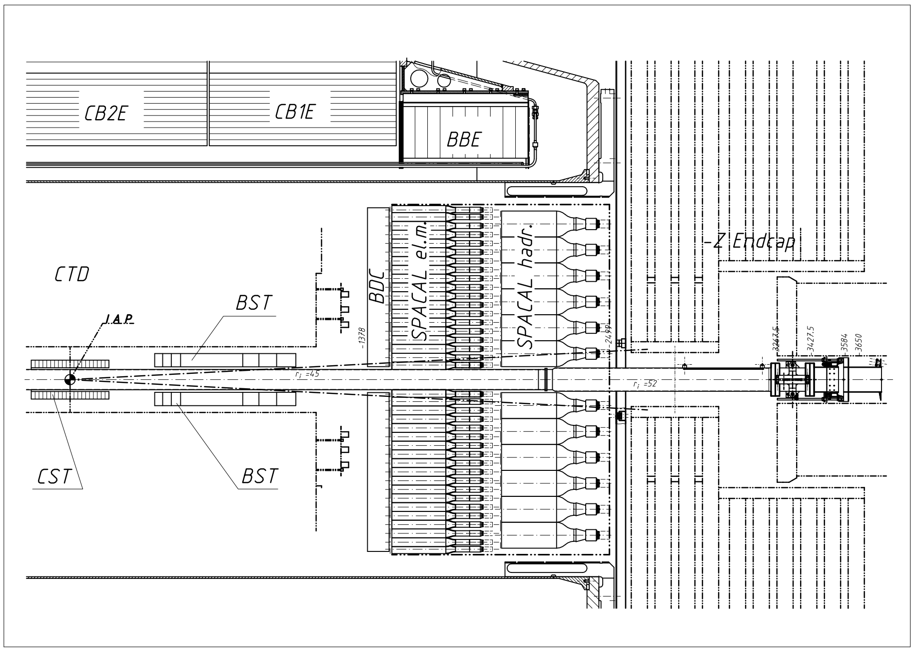

Figure 2.7: A cross sectional view, in the $r - z$ plane, of the SpaCal.

which arrives from upstream with a timing difference of approximately 10 ns. The SpaCal covers the angular region $153° \leq \theta \leq 177.5°$.

The SpaCal consists of two distinct sections, the inner electromagnetic and outer hadronic calorimeters. Such an arrangement improves the electromagnetic energy measurement while maintaining coverage of hadronic particles and longitudinal segmentation. Furthermore, electron and pions can be discriminated to better than one part in a hundred. Both sections of the SpaCal have a similar design, consisting of a series of grooved lead plates as the absorbing material that hold scintillating fibres. The particle showers induced by the lead plates cause the fibres to scintillate, with the light from the fibres collected using photomultiplier tubes. This gives the detector a response of approximately 1 ns, hence time of flight information can be used to distinguish upstream background. The electromagnetic section has scintillating fibres with a radius of 0.5 mm, giving a lead to fibre ratio of 2.3:1, and is 250 mm deep, corresponding 28 radiation lengths. The hadronic section has larger fibres of radius 1.0 mm, giving a lead to fibre radius of 3.4:1, and has a depth of 1.02 interaction lengths in addition to the 1.0 interaction length from the electromagnetic section.

The energy resolution of the electromagnetic section has been measured by test beams to be $\frac{\sigma_E}{E} = \frac{0.07}{\sqrt{E/\mathrm{GeV}}} \oplus 0.01$ [13] with a spatial resolution of 3.4 mm. The hadronic section has an energy resolution of $\frac{\sigma_E}{E} = \frac{0.13}{\sqrt{E/\mathrm{GeV}}} \oplus 0.04$ [14] for electrons and $\frac{\sigma_E}{E} = 0.56 \pm 0.03$ for pions [14]. When the electromagnetic and hadronic sections are combined the pion energy resolution is $\frac{\sigma_E}{E} = 0.29 \pm 0.02$ [15].

2.5 Muon Systems

2.5.1 Instrumented Iron

The Central (CMD) and Forward (FMD) muon detectors are used to measure muons that generally escape the H1 detector. The CMD consists of the remaining five of the sixteen limited streamer tubes in the instrumented iron not used by the tail catcher. Readout is from a wire running along the centre of the streamer tube and from perpendicular strips. The CMD has a 90% reconstruction efficiency for muons, measured using cosmic ray muons.

2.5.2 Forward Muon Detector

The FMD, shown in figure 2.2, is designed to detect high energy muons in the angular range $3^\circ \leq \theta \leq 17^\circ$, providing reconstruction and triggering in the very active forward region of H1. It is situated outside the forward section of the iron return yoke and consists of two sets of three drift chambers in the $r - \phi$ plane on either side of a toroidal magnet. Four of the drift chamber planes contain wires strung tangentially to allow measurement of the azimuthal angle θ. The remaining two layers of drift chambers have radially strung wires to facilitate measurement of the polar coordinate, ϕ.

2.6 Time of Flight

The rate of background events from beam-gas and beam-wall interactions at HERA is much larger than the rate of *ep* physics events [1]. However, by simply measuring the arrival time of particles at a selection of positions in the z coordinate these backgrounds can be separated from *ep* physics events, as particles from the interaction point will arrive at a different time. Three time of flight (ToF) systems are positioned near the beam pipe in the backward endcap of the iron return yoke, within the plug calorimeter and near to the FMD. The detectors consist of plastic scintillators with photomultiplier tubes to readout the scintillation light. This provides the necessary narrow time resolution to distinguish background sources from *ep* physics. The veto wall, a double layer of scintillators positioned outside the backward iron return yoke, also provides time of flight information. It detects particles from the proton beam halo – particles, mostly muons, that originate from beam-gas or beam wall collisions some distance from the detector. Additionally, the SpaCal is used for time of flight information.

2.7 Luminosity System

The measurement of luminosity is crucial to any particle physics analysis that measures a cross section. At H1 the luminosity is measured by a brace of taggers situated along the HERA beam pipe in the $-z$ direction [17], as shown in figure 2.8. In addition to measuring the absolute luminosity at the interaction point, the luminosity system provides real time luminosity measurement for steering of the HERA beams and measurement of outgoing electrons and photons when scattered through a small

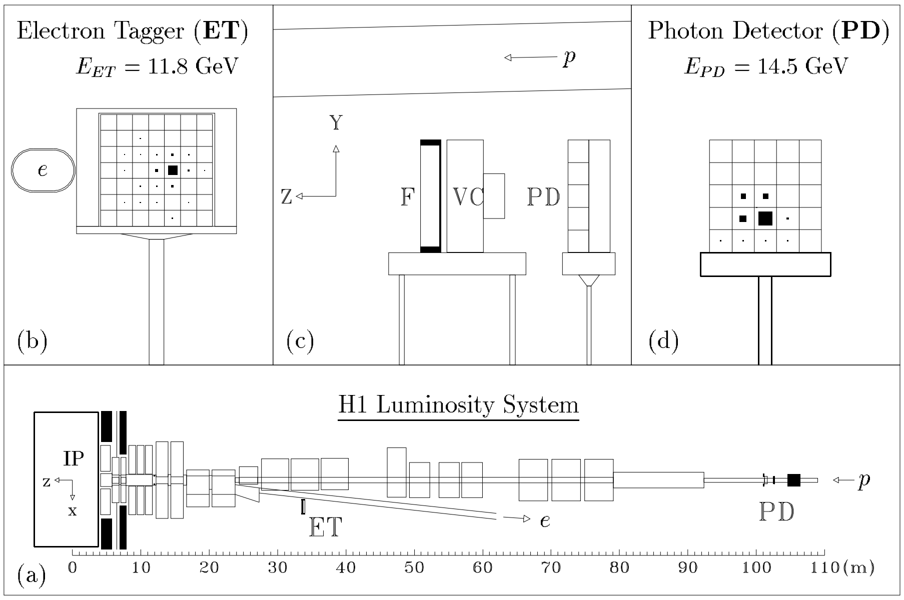

Figure 2.8: A bremsstrahlung event detected in the luminosity system. (a) $z-x$ view of the luminosity system, showing the positions of the electron tagger (ET) and photon detector (PD) relative to the interaction point (IP). (b) $x-y$ view of the ET. (c) $z-y$ view of the PD shielded by the lead filter (F) and water Čerenkov detector (VC). (d) $x-y$ view of the PD.

angle.

The luminosity system consists of an electron tagger (ET) and a photon detector (PD). Both detectors are constructed from TlCl/TlBr crystals with photomultiplier tube readout, have a depth of 22 interaction lengths and have an energy resolution of $\frac{\sigma(E)}{E} \sim \frac{0.10}{\sqrt{E/\text{GeV}}} \oplus 0.01$. Scattered electrons are deflected by HERA beam magnets through an exit window and into the ET situated adjacent to the beam pipe at $z = -33.4$ m. Due to the dependence on the HERA magnets, the acceptance of the ET is particularly sensitive to beam optics and the position of the interaction point, both of which often change. Photons pass through an exit window where the HERA beam pipe begins to curve and into the PD located at $z = -102.9$ m. In front of the PD is a two radiation length deep lead filter and a one radiation length water

Čerenkov detector veto counter to protect the PD from high synchrotron radiation flux. On the positive z side of the PD a 2 m thick iron wall protects the PD.

Luminosity measurements are made using the Bethe-Heitler process [18], $ep \rightarrow ep\gamma$, which has been calculated precisely in QED to an accuracy of 0.5%. The main background to this process is from interactions between the electron beam and gas particles in the beam pipe. This background is subtracted in data using pilot bunches. Online luminosity measurements are made by detecting scattered electrons in the ET in coincidence with outgoing photons in the PD. An additional condition is placed on the sum of the electron and photon energies to be approximately equal to the incident electron energy. The main contribution to the systematic error of the luminosity measurement is due to the tilt of the beams at the interaction point. The offline luminosity is measured from only the outgoing photon, as the acceptance of the PD is much less dependent on beam optics than the ET. An additional correction for the background from protons in satellite bunches, which can be as large as 10%, is made. The luminosity measurement used in this thesis is known to an accuracy of 1.5%.

In addition to the ET and PT, taggers are located at $z = -8$ m and $z = -44$ m to detect the scattered electron in slightly different kinematic ranges to the ET. Neither of these taggers are used in this thesis.

2.8 Triggering and Data Acquisition

At HERA bunch crossings occur every 96 ns, however even with sophisticated electronics the H1 detector requires approximately 1.5 μs to read out its $\sim$ 270 000 channels. Such a time difference would lead to an unacceptable amount of dead time when the detector is unable to read out any more information. Hence H1 uses a pipelined trigger and readout system to store the subdetector information in a

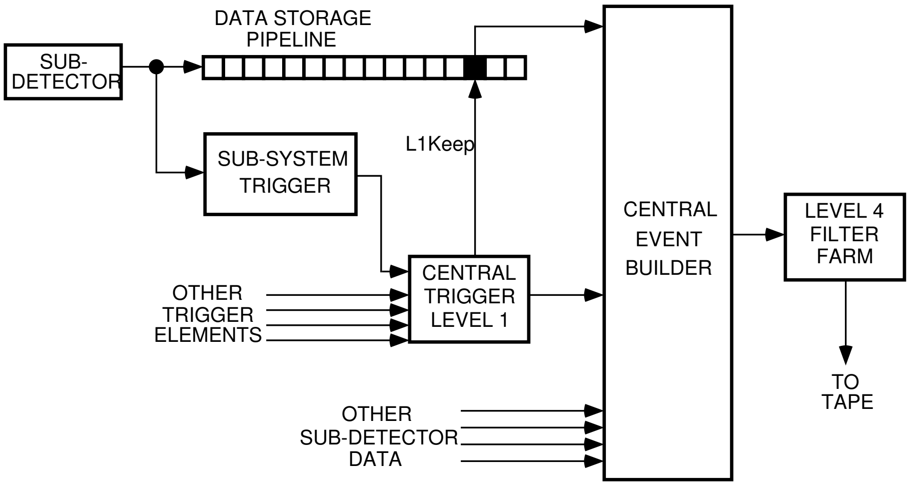

Figure 2.9: A schematic view of the H1 trigger and data acquisition system. Only levels one and four are shown.

buffer while trigger decisions are made on whether to keep or reject the event.

The level one (L1) central trigger (CTL1) [19], shown in figure 2.9, receives groups of trigger elements (TEs) from the majority of subdetectors for every bunch crossing. A total of 24 bunch crossings is needed to readout all of the TEs and produce an L1 decision. Hence, a pipeline buffer capable of storing information for 24 events are used, so that L1 remains deadtime free. Any event that is not kept falls off the end of the pipeline. Approximately 200 individual TEs are combined into 128 subtriggers. Physics subtriggers combine TEs for physics selections with those for background rejection. Other subtriggers are used to monitor specific backgrounds or trigger efficiencies. Some of these subtriggers, along with triggers for some physics processes, have large rates, which would swamp the read out chain at the expense of more 'interesting' physics processes. Hence prescaling is employed at L1 to only retain a preset fraction of events kept by such subtriggers. When an L1Keep signal is sent pipelining stops and the event is passed to level two (L2) triggering. L2 consists of both a topological trigger [20] and neural network trigger [21]. The additional time at L2 allows for different subdectors to be combined for such triggers, however a decision must still be made within 20 μs. When an L2Keep signal is sent the full event information is sent to the level four (L4) central event builder (CEB), the pipeline is then restarted and the deadtime ends. The triggering and reading of an event costs $1 - 2$ μs of dead time. Overall the typical deadtime is approximately 10%.

At L4 a PC farm performs a limited reconstruction of events to make further trigger decisions. Most of the remaining beam-gas, cosmic and trigger noise background events are removed. Furthermore, events are passed which contain a hard scale or an identified exclusive final state. Events classified as 'soft physics' at L4 are downscaled with respect to Q^2 and receive an 'L4 weight'. Hence this weight should be considered when forming final event counts.

The input to L4 is limited to approximately 50 Hz to avoid deadtime from the CEB reconstruction and output is at approximately 10 Hz to tape. Approximately 1% of events that fail L4 are kept to monitor the rejection.

Full reconstruction and classification is carried out offline at level five (L5). At L5 individual detectors are reconstructed, track segments are linked with energy clusters and a complete overall description of the event is produced. Events are classified into groups with similar physics signatures. The full L5 output is then written to storage tape.

The most important subdetector for triggering in this thesis is the SpaCal, which provides an inclusive electron trigger (IET) using the electromagnetic SpaCal, as well as ToF information and energy sums of both the electromagnetic and hadronic sections. The IET considers a sum over a 4×4 cell window within the ToF time period, shown in figure 2.10. The windows overlap with two cells from adjacent windows to ensure no inefficiency from electrons being situated near the edge of windows. The sum is compared to three programmable thresholds to give the trigger elements `SPACAL_IET>n` where `n`=0,1,2. Typical thresholds are 0.5, 2 and 6 GeV,

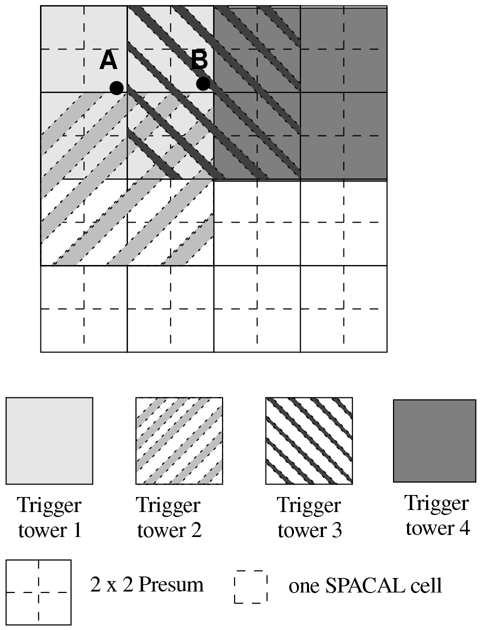

Figure 2.10: A schematic view of the overlapping window technique used for the SPACAL_IET trigger elements. For an electron incident at point A all of the energy deposits are contained within trigger tower 1. For an electron incident at point B energy deposits are contained within both trigger towers 1 and 2, but all of the energy deposits are contained within trigger tower 3.

respectively. Additionally, the SpaCal is divided into two regions – the central region, a 24×24cm region around the beampipe, and the remaining outer region. This is due to the central region having a large trigger rate from an upstream background. This is thought to be caused by the proton beam halo interacting with collimators upstream from the interaction point, causing a background in time with the proton beam.

The luminosity system is also used for one of the triggers in this analysis. The basic trigger element is formed from having a deposit of energy above a certain threshold in the 33m electron tagger in coincidence with no deposit above a threshold in the photon tagger.

2.9 Simulation

For the data produced at H1 to be compared to theoretical predictions and to data from other experiments the effects of the H1 detector acceptance and resolution smearing must be taken into account. For this Monte Carlo (MC) techniques are used. Firstly, an event generator produces a complete list of partons for a given event from relevant Feynman diagrams and parton density functions. The generator then further simulates any short lived partons decaying into stable particles. This stage of the simulation is known as the hadron or generator level. For this thesis the HERWIG event generator [22] is used for simulation of the signal process. A simulation of the H1 detector within the GEANT3 framework [23] is then used to model the interaction of the particles with the detector. The information can then be passed through reconstruction software, as if it were real data, to produce simulated data that is directly comparable to the H1 data. This is known as the detector or reconstructed level. Hence, correction factors can be found by comparing the generator and reconstructed levels of the MC and applied to the H1 data.

Chapter 3

HERA Physics

3.1 HERA Kinematics

The generalised electron-proton interactions at HERA are shown in figure 3.1. In electroweak theory the interaction proceeds via the exchange of either a photon or Z boson in the neutral current (NC) interaction, or the exchange of a $W^{\pm}$ boson in the charged current (CC) interaction. The negative four momentum transfer squared of the exchanged boson is given by

$$Q^2 = -q^2 = -(k - k')^2 \tag{3.1}$$

where q is the four momentum of the exchanged boson and k and k' are the four momentum of the incident and scattered electron, respectively. This is also a measure of the virtuality of the exchanged boson, or how near the exchanged boson is to its mass shell. For massive vector bosons the propagator term $\sim 1/(Q^2 + M^2)$ occurs in the electroweak scattering amplitude. So, unless in the region of the electroweak unification scale ($Q^2 \simeq M_Z^2$, ie. near to the Z mass shell) the NC cross section is dominated by photon exchange.

The negative four momentum transfer squared also represents the spatial resolv-

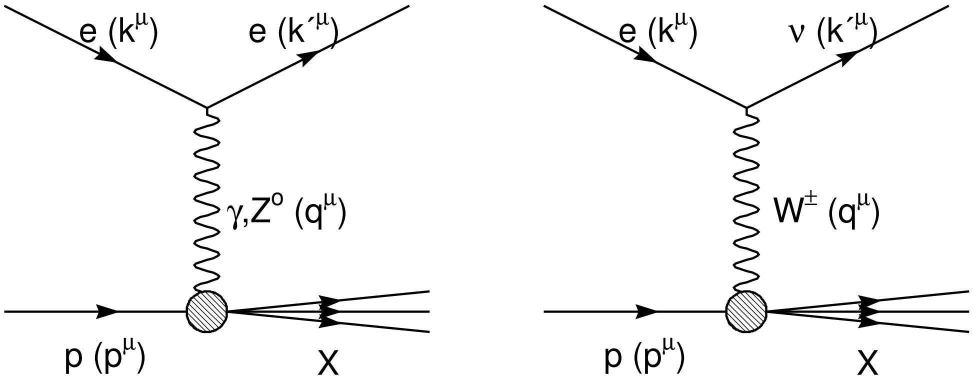

Figure 3.1: Electron-proton scattering via the exchange of (a) a photon or Z^0 boson and (b) a W boson.

ing power of the photon – as Q^2 increases the wavelength of the virtual photon decreases. Hence, when $Q^2 \gtrsim 1$ GeV^2 the photon is able to probe the substructure of the proton[1] and this is the kinematic regime known as deep inelastic scattering (DIS). At the Born level (figure 3.2) this is seen as the exchange of a single photon, Z or W which couples with a point-like constituent within the proton. When the momentum transfer is small, $Q^2 \ll 1$ GeV^2, the photon tends towards the properties of real photons and this is the kinematic region known as photoproduction.

Three independent Lorentz invariant scaling variables are used to describe the kinematics of DIS. Firstly, the dimensionless quantity x

$$x = \frac{Q^2}{2p.q} \tag{3.2}$$

where p is the four vector of the incident proton. If the partons of the proton are considered massless and carry no transverse momentum, x is the fraction of the proton momentum carried by the struck parton. Secondly, the dimensionless quantity y

$$y = \frac{p.q}{p.k} \tag{3.3}$$

[1]The proton radius is of the order 10^{-15}m, corresponding to $Q^2 \simeq 1$ GeV^2

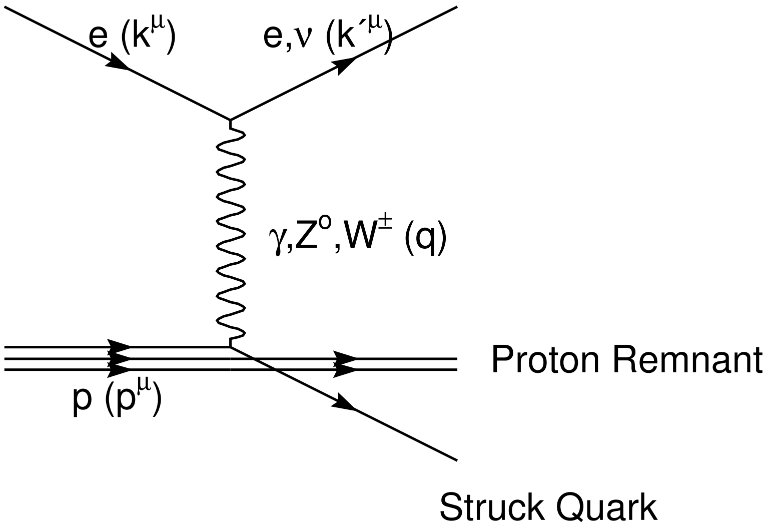

Figure 3.2: Electron-proton scattering at the Born level.

which in the proton rest frame is the fractional energy lost by the incident electron. In addition the square of the ep centre of mass energy, s, is given by

$$s = (k + p)^2 \tag{3.4}$$

and the square of the γp centre of mass energy, W, is given by

$$W^2 = (q + p)^2 \tag{3.5}$$

Since s is fixed at HERA, the scattering can be described by two independent variables through the relation

$$Q^2 = sxy \tag{3.6}$$

when the mass of the incident particles are small compared to the centre of mass energy.

3.2 Proton Structure

The total differential inelastic electron-proton cross section[2] may be parameterised in terms of two[3] structure functions, $F_1(x,Q^2)$ and $F_2(x,Q^2)$, as

$$\frac{d^2\sigma_{ep\to eX}}{dxdQ^2} = \frac{4\pi\alpha_{em}^2}{xQ^4}\left[xy^2F_1(x,Q^2) + (1-y)F_2(x,Q^2)\right] \tag{3.7}$$

where $F_1(x,Q^2)$ and $F_2(x,Q^2)$ are related to the momentum distributions of charged partons in the proton. It is necessary to use two parameters, due to the two independent contributions to the photo-absorption cross section from transversely and longitudinally polarised virtual photons. The structure functions can be related to structure functions for scattering of transversely and longitudinally polarized photons, $F_T(x,Q^2)$ and $F_L(x,Q^2)$, respectively, by

$$F_T(x,Q^2) = 2xF_1(x,Q^2) \tag{3.8}$$

$$F_L(x,Q^2) = F_2(x,Q^2) - 2xF_1(x,Q^2) \tag{3.9}$$

Hence, the total cross section becomes

$$\frac{d^2\sigma_{ep\to eX}}{dxdQ^2} = \frac{2\pi\alpha_{em}^2 Y_+}{xQ^4}\left[F_2(x,Q^2) - \frac{y^2}{Y_+}F_L(x,Q^2)\right] \tag{3.10}$$

where $Y_+ = 1+(1-y)^2$. The structure function $F_2(x,Q^2)$ is extracted from measurements of the total cross section by estimating the small contribution from $F_L(x,Q^2)$ and QED radiative corrections. The contribution from F_L is negligible except at high y and then is still small. Indeed, for the predictions of the Quark Parton Model, $F_L = 0$ due to quarks having a spin of $\frac{1}{2}\hbar$. Recent results for $F_2(x,Q^2)$ from H1 [25] are shown in figure 3.3.

[2] For a detailed discussion see, for instance, [24].

[3] At high Q^2, where Z^0 exchange becomes important, a third, parity violating, structure function $F_3(x,Q^2)$ is needed to describe the neutral current cross section.

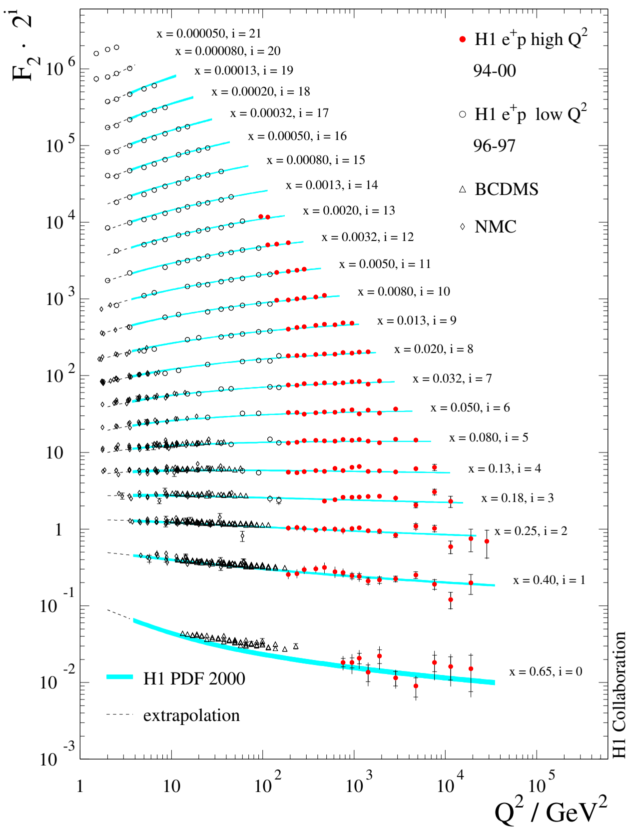

Figure 3.3: The structure function F_2 as measured by H1 and fixed target experiments. The data are compared to the Standard model expectation from a QCD fit to the data (shaded band). The dashed curve shows the extrapolation for Q^2 less than the starting value of the fit.

3.2.1 Quark Parton Model

First measurements of F_2 [26] revealed little, or no, dependence on Q^2 over a wide range of Q^2 and x. This striking behaviour is called scaling [27] and led to the development of the Quark Parton Model (QPM) [28]. The QPM states that the proton has a substructure of non-interacting, point-like constituents called partons. A consequence of having no length scale for partons is then the scale invariance seen in F_2. Additionally, for DIS, the electron should scatter incoherently and elastically off the parton. Hence the QPM is formulated in the infinite momentum frame of the proton, meaning the time scale for interactions between partons is therefore dilated. Thus the photon-parton interaction is instantaneous and incoherent so the partons can be considered free. Any further interactions, for instance to confine the partons into hadrons, occur on a much longer time scale.

By introducing the parton density function (PDF), $f_i(x, Q^2)$, for a parton i with a charge e_i, the total cross section can be written as

$$\frac{d^2\sigma_{ep\to eX}}{dxdQ^2} = \sum_i \int_0^1 dx f_i(x) \frac{d^2\sigma_{eq_i\to eq_i}}{dxdQ^2} \tag{3.11}$$

where $\frac{d^2\sigma_{eq_i\to eq_i}}{dxdQ^2}$ is the differential elastic cross section for electron-parton scattering. Thus the PDF is the probability of a parton i having a momentum fraction x of the momentum of the proton. Within the QPM the proton contains three valence quarks, a sea of quark-antiquark pairs and many gluons. The elastic cross section calculated in QED leads to

$$F_2(x, Q^2) = x \sum_i e_i^2 f_i(x, Q^2) \tag{3.12}$$

and

$$F_2(x, Q^2) = 2xF_1(x, Q^2) \tag{3.13}$$

The second equation is the Callan-Gross equation [29] and is a direct consequence of quarks having spin $\frac{1}{2}\hbar$. From equations 3.9 and 3.13 it follows that F_L is zero. Experiments [30] have measured the ratio $\frac{F_L}{F_2 - F_L}$, known as the photo-absorption ratio, as close to zero, showing that equation 3.13 approximately holds and hence partons have a spin of $\frac{1}{2}\hbar$.

3.2.2 Scaling Violations

Within the QPM the assumption is made that partons are non-interacting, however the experimental fact that free quarks and gluons are not seen is inconsistent with

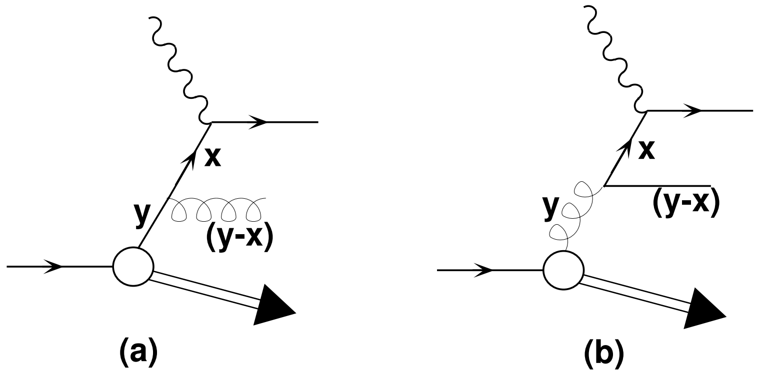

Figure 3.4: Diagrams of the splitting functions (a) $P_{qq}(x/y)$, corresponding to gluon bremsstrahlung from the original quark and (b) $P_{qg}(x/y)$, corresponding to the original gluon splitting into a quark-antiquark pair.

this assumption. Additionally, scaling is only seen for $x \sim 0.15$, whereas there is a clear Q^2 dependence for other values of x. In figure 3.3 F_2 is seen to rise with Q^2 at low x and fall with Q^2 at high x. A solution to these deviations from the QPM is to introduce interacting gluons into the picture. The QPM is zeroth order in QCD. Leading order contributions in QCD come from gluon emission from a quark (figure 3.4 (a)) and quark-antiquark pair production from a gluon (figure 3.4 (b)). To include higher order processes within the description of the proton, a perturbative-QCD (pQCD) expansion in orders of α_s is considered. The expansion is only convergent for small values of α_s, corresponding to values of $Q^2 \gtrsim 3$ GeV^2 or other such hard scales, allowing predictions to be made. The gluon emission and splitting processes result in corrections to F_2 of the form $\alpha_s \ln Q^2$ and $\alpha_s \ln \frac{1}{x}$, where α_s is the QCD coupling constant. For an expansion to a given order, n, in pQCD, F_2 has corrections of the form $\alpha_s^n \ln^m Q^2$ and $\alpha_s^n \ln^m \frac{1}{x}$ where $m \leq n$. A small non-zero pQCD prediction for F_L is also made. A full QCD expansion is however not tractable. Nevertheless, evolution equations to evaluate the value of F_2 at one point in phase space given a starting value elsewhere in phase space are possible. In different regions of the $x - Q^2$ phase space one of the two kinds of term of the expansion dominate.

3.3 Low x Phenomenology

One of the more compelling aspects of the measurements of F_2 is the rise with decreasing x at low x. Two of the schemes to describe this evolution by considering QCD corrections to leading order processes, DGLAP and BFKL, are explained in the following section. The DGLAP mechanism evolves PDFs with Q^2, provided that pQCD is applicable ($Q^2 \gtrsim 1-3$ GeV^2), over a large range of x, even very low x. The BFKL mechanism, however, evolves PDFs only at low x.

3.3.1 The DGLAP Evolution Mechanism

A set of equations were developed by Dokshitzer, Gribrov, Lipatov, Alterelli and Parisi [31] to describe the Q^2 evolution of PDFs. The PDFs are split into valence quark (flavour non-singlet), sea quark (flavour singlet) and gluon distributions. The evolution equations are not calculable for all phase space in QCD. However, they may be used to evolve PDFs from a starting scale, Q_0^2, where pQCD is valid, to higher values of Q^2 with the PDFs at Q_0^2 as starting parameters. A typical starting value is $Q_0^2 \simeq 1$ GeV^2.

The QCD corrections are evaluated through the splitting functions $P_{ab}\left(\frac{x}{y}\right)$, which are the probability of a parton a with momentum fraction x coming from parton b with momentum fraction y. Valence quarks are affected by gluon bremsstrahlung ($q \rightarrow qg$), described by the splitting function P_{qq}. The sea quark distributions are modified by gluon bremsstrahlung and quark-antiquark pair production ($g \rightarrow q\bar{q}$), described by P_{qg}. The gluon distributions are affected by gluon bremsstrahlung and gluon splitting ($g \rightarrow gg$), described by P_{gg}. The resulting DGLAP equations are

$$
\frac{dq^{NS}(x,Q^2)}{d\ln Q^2} = \frac{\alpha_s(Q^2)}{2\pi}\int_x^1 \frac{dy}{y}\left[q^{NS}(y,Q^2)P_{qq}\left(\frac{x}{y}\right)\right] \tag{3.14}
$$

$$
\frac{dq^{S}(x,Q^2)}{d\ln Q^2} = \frac{\alpha_s(Q^2)}{2\pi}\int_x^1 \frac{dy}{y}\left[q^{S}(y,Q^2)P_{qq}\left(\frac{x}{y}\right)+g(y,Q^2)P_{qg}\left(\frac{x}{y}\right)\right] \tag{3.15}
$$

$$
\frac{dg(x,Q^2)}{d\ln Q^2} = \frac{\alpha_s(Q^2)}{2\pi}\int_x^1 \frac{dy}{y}\left[q^{S}(y,Q^2)P_{gq}\left(\frac{x}{y}\right)+g(y,Q^2)P_{gg}\left(\frac{x}{y}\right)\right] \tag{3.16}
$$

Presently the splitting functions have been calculated to leading and next to leading order in QCD.

By solving the above equations and using equation 3.12, a logarithmic dependence of F_2 on Q^2 is found that reproduces the fall of F_2 with Q^2 at high x and the rise with Q^2 at low x. This may be seen as resolving more of the partonic substructure as Q^2 increases – at high x gluon radiation from valence quarks causes F_2 to fall with Q^2, whereas at low x gluon splitting causes F_2 to rise with Q^2.

The full DGLAP evolution equations iterate the leading order splitting processes to give a ladder of parton emissions, hence summing all terms with a maximum power of $\ln Q^2$. When the sum is over terms in $\alpha_s^n \ln^n Q^2$ it is known as the Leading Logarithm Approximation (LLA). This is applicable in the range of large Q^2 and intermediate x, that is $\ln(1/x) \ll \ln(Q^2/Q_0^2)$, and in the range of perturbation theory, $\alpha_s \ll 1$. The partons summed over in the ladder have strong ordering in transverse momentum

$$
k_{Tn}^2 \gg k_{Tn-1}^2 \gg ... \gg k_{T1}^2 \tag{3.17}
$$

and soft ordering in fractional longitudinal momentum

$$
x_n < x_{n-1} < ... < x_1 \tag{3.18}
$$

due to a daughter parton not being able to have a longitudinal momentum larger than the parent parton.

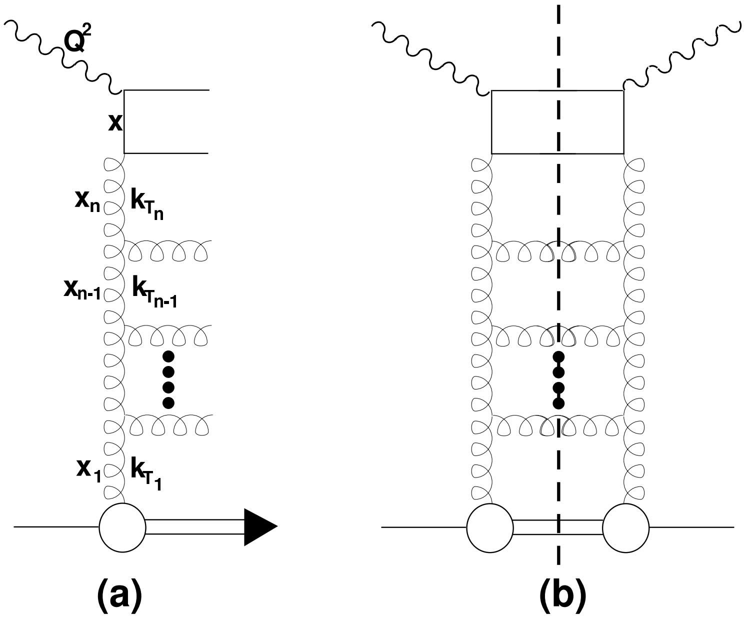

Figure 3.5: (a) A ladder diagram which contributes to $F_2(x, Q^2)$ at low x. In the DGLAP formalism the ladder consists of both quarks and gluons, whereas in the BFKL formalism only gluons contribute. The BFKL equation is formed by summing squared amplitudes such as (b).

3.3.2 The BFKL Evolution Mechanism

When in the low x region of phase space, the $\ln(1/x)$ terms neglected in the DGLAP formalism must be considered. At fixed Q^2 a LLA expansion can be made in terms of $1/x$. The kinematic constraints are hence reversed and calculations are made in the phase space region $\ln(Q^2/Q_0^2) \ll \ln(1/x)$. The resulting evolution equation was developed by Balitsky, Fadin, Kuraev and Lipatov (BFKL) [32]. It is assumed that at low x PDFs are dominated by gluon splitting ($g \to gg$), hence the typical contribution to F_2 is from a gluon ladder, as shown in figure 3.5(a). By summing all squared amplitudes from all gluon interactions, for example figure 3.5(b), the BFKL equation

$$x\frac{\partial f}{\partial x} \equiv K_L \otimes f(x, k_T^2) \tag{3.19}$$

is obtained, where $f(x, k_T^2)$ is the non-integrated gluon distribution and the symbol $\otimes$ implies integration over x and k_T^2. K_L is the Lipatov kernel and symbolises the summation over terms in $\alpha_s^n \ln^n(1/x)$. By solving the BFKL equation analytically at fixed Q^2, F_2 is found to depend on x as

$$F_2 \sim x^{\lambda} \tag{3.20}$$

where

$$\lambda = \frac{12\alpha_s}{2\pi} \ln 2 \tag{3.21}$$

Hence BFKL predicts the evolution with x of F_2 at low x given the input of F_2 measured at a higher x, but the same Q^2. At HERA energy scales $\lambda \sim 0.5$.

In contrast to the DGLAP formalism, the BFKL formalism has strong ordering of fractional longitudinal momenta for partons in the ladder

$$x_n \ll x_{n-1} \ll ... \ll x_1 \tag{3.22}$$

and no ordering of transverse momenta.

Presently, inclusive structure functions at low x are consistent with BFKL evolution within the accuracy of HERA measurements. However, this is also the case for DGLAP predictions. Future measurements may probe regions of $x - Q^2$ phase space that can discriminate between the two presented evolution schemes.

Chapter 4

Diffraction

4.1 Regge Theory

Regge theory describes the scattering amplitude of a two body interaction in the limit of the centre of mass energy of the particles being much greater than the other scales in the process. The theory is based on general assumptions of the scattering process and was developed before QCD. It therefore provides a constraint on the QCD description of scattering at high energy [33]. The following section is a brief overview of Regge theory to introduce the concept of diffractive exchanges and the pomeron. More detailed information may be found in [34].

A general two body scattering process, $ab \rightarrow cd$, may be described in terms of Lorentz invariant scalar products of particle momenta and the particles masses. For instance the Mandelstam variables, s, t and u, defined as

$$s = (p_a + p_b)^2 = (p_c + p_d)^2 \tag{4.1}$$

$$t = (p_a - p_c)^2 = (p_b - p_d)^2 \tag{4.2}$$

$$u = (p_a - p_d)^2 = (p_b - p_c)^2 \tag{4.3}$$

where p_i is the four momentum of particle i, may be used. Through conservation

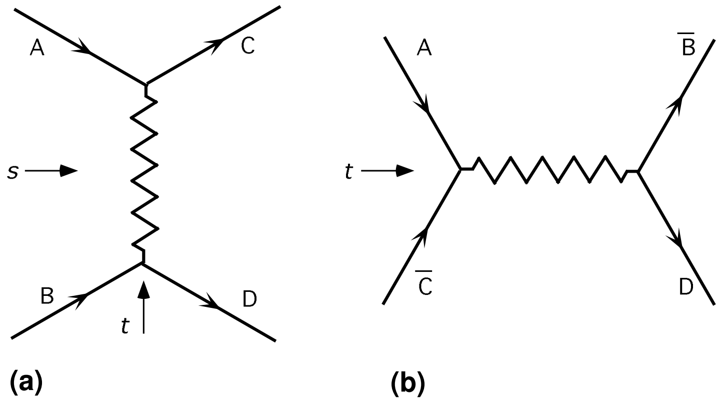

Figure 4.1: (a) The t channel process $ab \to cd$ and (b) the associated s channel process $a\bar{c} \to \bar{b}d$.

of momentum u is not an independent variable, so the scattering amplitude may be written $A = A(s, t)$. The square of center of mass energy is given by s and the square of the four momentum transfer between the two initial state particles is given by t.

Regge theory describes the high energy scattering amplitude in the Regge limit, $s \to \infty$ and $s \gg t$. A further assumption must be made that the scattering amplitude is an analytic function of Lorentz invariant variables, assumed to be complex. This leads to an important property of scattering amplitude – crossing symmetry. The scattering amplitude $A_{ab\to cd}$ has a physical kinematic region for the s-channel process of $s > 0$ and $t < 0$. If the the amplitude is carried into the unphysical region $s < 0$ and $t > 0$ then this is the physical region for the t-channel process $a\bar{c} \to \bar{b}d$. Crossing symmetry states that these two physically different processes have the same scattering amplitude, in other words

$$A_{ab\to cd}(s, t) = A_{a\bar{c}\to\bar{b}d}(t, s) \tag{4.4}$$

The t-channel scattering amplitude for the process $a\bar{c} \to \bar{b}d$ may be expressed as a series of partial waves of different angular momentum

$$A_{a\bar{c}\to\bar{b}d}(s,t) = \sum_{l=0}^{\infty}(2l+1)a_l(s)P_l(\cos\theta) \tag{4.5}$$

where $P_l(\cos\theta)$ is the Legendre Polynomial for angular momentum l, the cosine of the scattering angle between a and c is given by $\cos\theta = 1+\frac{2t}{s}$ and $a_l(s)$ is the partial wave amplitude. When the full partial wave series is summed poles are found for the l^{th} partial wave of the form

$$a_l(t) \simeq \frac{\beta(t)}{l-\alpha(t)} \tag{4.6}$$

giving a 'Regge pole' for $l = \alpha(t)$ with a residue function $\beta(t)$ that gives the coupling of the pole to external particles. In the Regge limit, $s \to \infty$, the leading contribution to the scattering amplitude is given by

$$A(s,t) \to \beta(t)s^{\alpha(t)} \tag{4.7}$$

This may be viewed as the exchange of an object with angular momentum $\alpha(t)$, called a reggeon. This is not a simple particle, as the reggeon angular momentum is complex and a function of t. It does, however, consist of a superposition of all possible exchanged particles with the correct quantum numbers. The t channel process with positive t has an amplitude with poles corresponding to physical particles of spin J_i and mass m_i where $\alpha(m_i^2) = J_i$.

Consider the process $\pi^-\pi^0 \to \bar{p}n$. The amplitude has poles corresponding to the resonant production of physical particles with quantum numbers of the ρ. If the spin of such particles are plotted against the square of the particle masses, as shown in figure 4.2, they are found to lie on the straight line

$$\alpha(t) = \alpha(0) + \alpha'(t) \tag{4.8}$$

where $\alpha(0) = 0.55$ and $\alpha' = 0.86\ \text{GeV}^{-2}$ [35]. Hence from equation 4.7, the scattering amplitude becomes

$$A(s,t) \sim s^{\alpha(0)+\alpha'(t)} \tag{4.9}$$

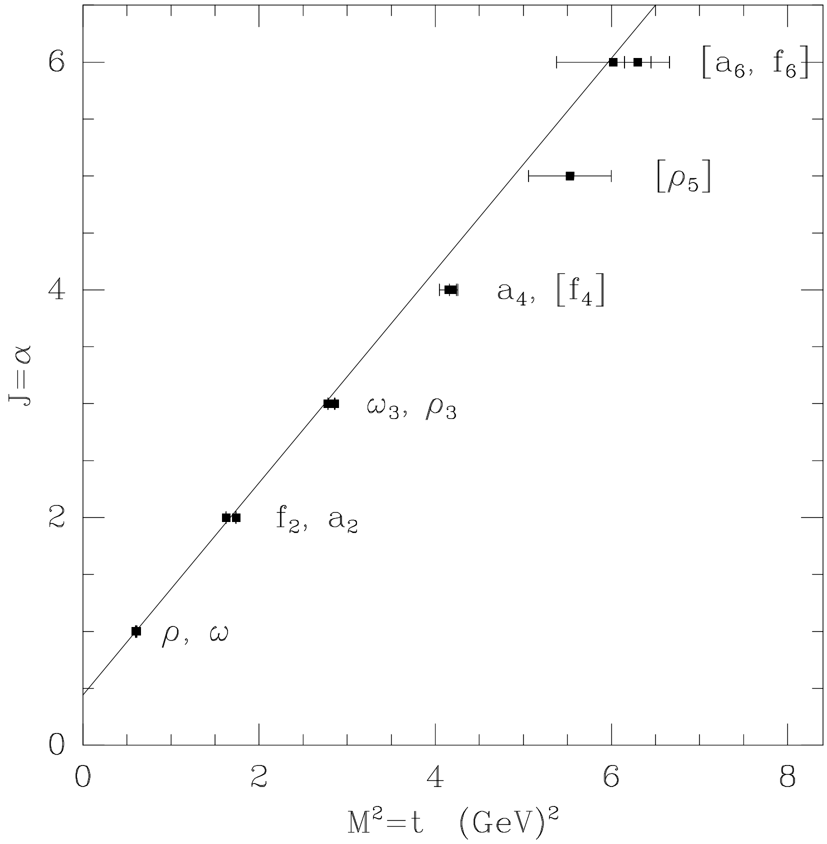

Figure 4.2: The Chew-Frautschi plot of the ρ trajectory.

and as the differential cross section is calculated to be

$$\frac{d\sigma}{dt} \sim \frac{|A(s,t)|}{s^2} \tag{4.10}$$

we find that

$$\frac{d\sigma}{dt} \sim s^{2\alpha(0)+2\alpha'(t)-2} \tag{4.11}$$

This prediction describes the data well in many processes [36]. In particular, the extrapolation of $\alpha(t)$ is able to describe the crossed process $\pi^- p \to \pi^0 n$ in the negative t region [37], shown in figure 4.3, as predicted by crossing symmetry.

The unitarity of the scattering matrix, A, leads to the Optical Theorem which relates the imaginary part of the forward elastic amplitude, A_{el}, to the total scattering

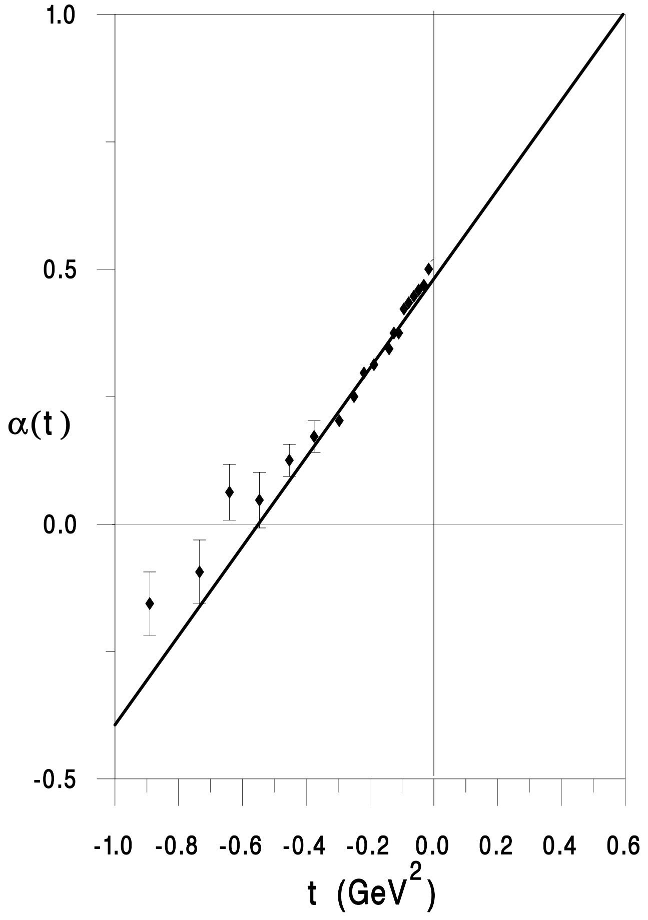

Figure 4.3: $\alpha(t)$ from $\pi^- p \to \pi^0 n$ scattering data (points) compared to the extrapolation of the trajectory from figure 4.2 to negative t (solid line).

cross section through

$$\sigma_{tot} = \frac{1}{s}\Im m[A_{el}(s,0)] \tag{4.12}$$

Hence, using equation 4.9, the Regge prediction for the total cross section is

$$\sigma_{tot} \sim s^{\alpha(0)-1} \tag{4.13}$$

where $\alpha(0)$ is the intercept of the pomeron trajectory. For example, the ρ trajectory has an intercept of $\alpha(0) = 0.55$ and hence the total cross section falls with increasing s for processes involving an exchange of these quantum numbers. A generalisation of this observation is seen in the proof by Pomerančuk and Okum [38] that any

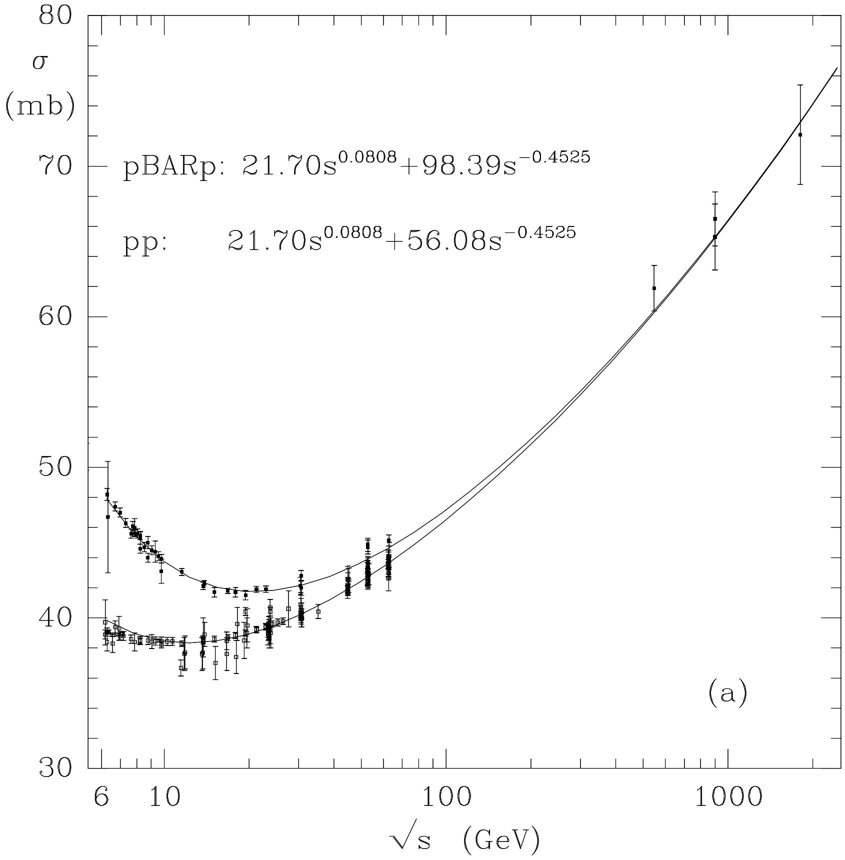

Figure 4.4: The centre-of-mass energy dependence of the proton-proton and proton-antiproton total cross section compared to a fit by Donnachie and Landshoff.

scattering process with charge exchanged has a vanishing cross section as $s \to \infty$, known as the Pomerančuk theorem. Foldy and Peierls [39] reversed this logic to state that if a cross section rises as $s \to \infty$ then the process must be dominated by the exchange of vacuum quantum numbers. The total hadron-hadron cross section has been observed to rise slowly with s, implying a Regge trajectory with intercept $\alpha(0) \geq 1$ and vacuum quantum numbers. This trajectory is known as the pomeron. However, no physical states have so far been found on this trajectory.

The total proton-proton and proton-antiproton cross sections, shown in figure

4.4, have been fitted with the form

$$\sigma_{tot}(s) = X s^{\alpha_{I\!P}-1} + Y s^{\alpha_{I\!R}-1} \tag{4.14}$$

where the first term is due to the pomeron trajectory, $\alpha_{I\!P}$, and the second term is due to the reggeon trajectory, $\alpha_{I\!R}$ [40]. The pomeron intercept is found to be $\alpha_{I\!P}(0) = 1.08$ and common to both processes, as an exchange of vacuum quantum numbers cannot distinguish between particles and antiparticles. The reggeon trajectory is found to have an intercept of $\alpha_{I\!R}(0) = 0.55$ and does distinguish between the two processes. Fits have also been made to the $\pi^- p$ and $\pi^+ p$ total cross sections and to the γp [41] total cross section using the same intercepts, implying that the pomeron may be considered as a universal object.

4.1.1 Diffractive Processes in γp Interactions

For a photon to interact with a proton via pomeron exchange within QCD it must fluctuate into a quark-antiquark pair. Thus the production of vector mesons, as shown in figure 4.5 (a) should be considered. The interaction $\gamma p \to V p$, where V is any vector meson, may be considered as quasi-elastic and accounts for approximately 10% of the total photoproduction cross section [41]. Regge theory predicts that the s dependence of the quasi-elastic cross section should be the same as the total γp cross section. The centre of mass energy dependence for the total photon-proton cross section and the total vector meson production cross sections are shown in figure 4.6. The ρ and ω production cross sections show a similar dependence as the total cross section. However, the J/Ψ, which has a hard scale due to its large mass, has a cross section which is significantly steeper. Inelastic diffraction where one or both of the interacting hadrons dissociates, as shown in figure 4.5 (a), may also be observed. Since no colour is exchanged by the interaction, the dissociated state must preserve the quantum numbers of the incident particle. At $W \sim 300$ GeV diffractive interactions make up approximately 40% of the total γp cross section [41].

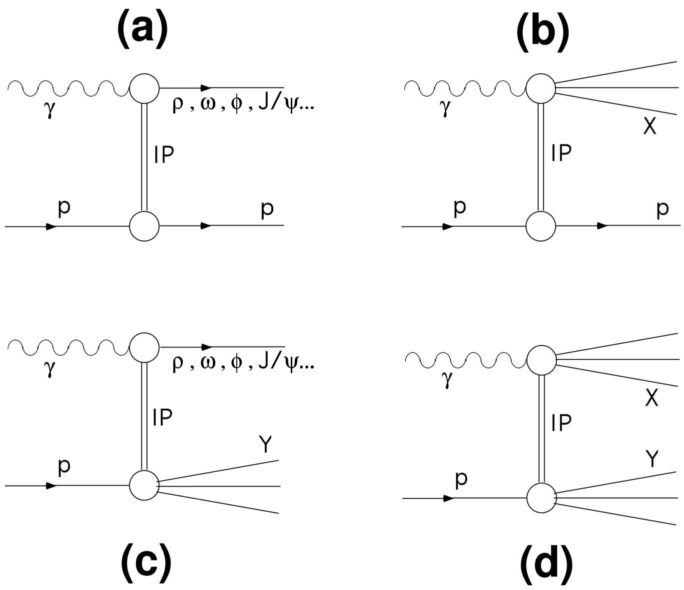

Figure 4.5: Diffractive interactions in γp interactions (a) Quasi-elastic vector meson production $\gamma p \rightarrow Vp$. (b) Single photon dissociation $\gamma p \rightarrow Xp$. (c) Single proton dissociation vector meson production $\gamma p \rightarrow VY$. (d) Double dissociation $\gamma p \rightarrow XY$.

4.2 Diffractive Deep Inelastic Scattering

A special case of DIS events where there is a large rapidity gap between the proton system and rest of the hadronic final state has been observed at HERA [42]. This may be viewed in the contexts of Regge theory, QED and QCD as a highly virtual photon probing a colour singlet object, or pomeron, produced from the proton. Hence analogies may be drawn between DIS and diffractive DIS. The same kinematic quantities as in standard DIS may be used, but by splitting the hadronic final state into two systems, X and Y, separated by the largest rapidity gap in the event (as shown in figure 4.7) the following variables may also be defined

$$M_X^2 = X.X \tag{4.15}$$

$$M_Y^2 = Y.Y \tag{4.16}$$

$$t = (p-Y)^2 = (q-X)^2 \tag{4.17}$$

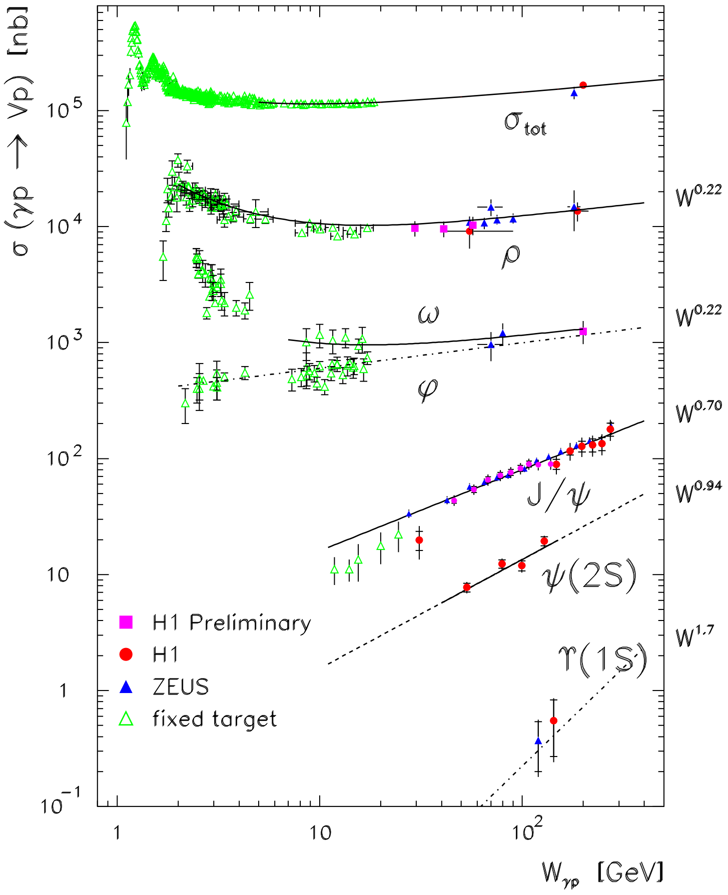

Figure 4.6: The centre of mass energy dependence of the total photon-proton cross section and the total vector meson production cross section at HERA and fixed target experiments.

$$\beta = \frac{-q^2}{2q.(P-Y)} = \frac{Q^2}{Q^2+M_X^2-t} \tag{4.18}$$

$$x_{I\!P} = \frac{q.(P-Y)}{q.P} = \frac{Q^2+M_X^2-t}{Q^2+W^2-M_P^2} = \frac{x}{\beta} \tag{4.19}$$

$$y_{I\!P} = \frac{P.(q-X)}{q.P} = \frac{M_Y^2-M_P^2-t}{Q^2+W^2-M_P^2} \tag{4.20}$$

In the infinite momentum frame of the proton $x_{I\!P}$ is the fraction of the proton momentum carried by the pomeron and β is the fraction of the pomeron momentum carried by the struck parton and is therefore analogous to x for the proton in standard DIS. Both M_X and M_Y are required to be small in the Regge limit and assure

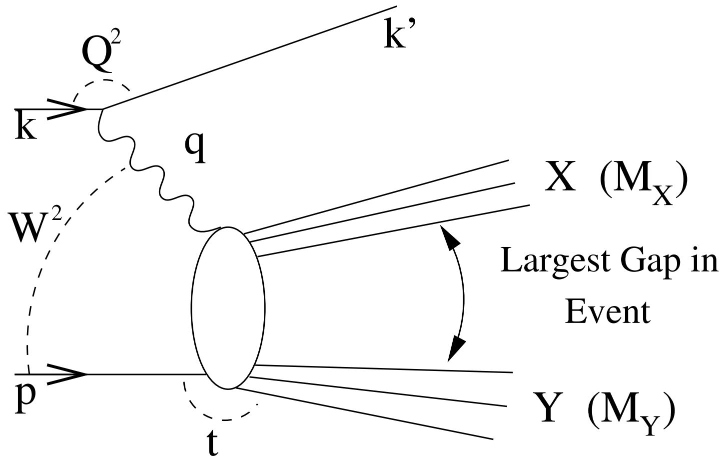

Figure 4.7: A schematic diagram of diffractive deep inelastic scattering at HERA.

a large rapidity gap.

The diffractive cross section for diffractive DIS may be written, by analogy to the total ep cross section from equation 3.10, as

$$\frac{d^3\sigma_{ep\to eXY}}{d\beta dQ^2 dx_{I\!P}} = \frac{4\pi\alpha_{em}^2}{\beta Q^4}\left(1 - y + \frac{y^2}{2}\right)\sigma_r^{D(3)}(\beta, Q^2, x_{I\!P}), \tag{4.21}$$

where the reduced cross section, $\sigma_r^{D(3)}(\beta, Q^2, x_{I\!P})$, is related to the diffractive structure functions $F_2^{D(3)}(\beta, Q^2, x_{I\!P})$ and $F_2^{D(3)}(\beta, Q^2, x_{I\!P})$ by

$$\sigma_r^{D(3)} = F_2^{D(3)} - \frac{y^2}{1 + (1-y)^2} F_L^{D(3)}, \tag{4.22}$$

such that $\sigma_r^D \sim F_2^D$ except at high y. The quantities β, Q^2 and $x_{I\!P}$ are reconstructed from the scattered electron and/or the X system. The Y system is not measured directly, hence t must be measured from the transverse momentum of the X system, which is reconstructed poorly. Therefore measurements at HERA are made over an integrated range of $M_Y < 1.6$ GeV and $|t| < 1.0$ GeV^2, giving the reduced cross section $\sigma_r^{D(3)}(\beta, Q^2, x_{I\!P})$. A measurement of $\sigma_r^{D(3)}(\beta, Q^2, x_{I\!P})$ from H1 is shown in figure 4.8 [45].

In the leading $\log(Q^2)$ approximation, QCD factorisation states that the cross section for the diffractive process $\gamma^* p \to p' X$ can be written as the convolution of

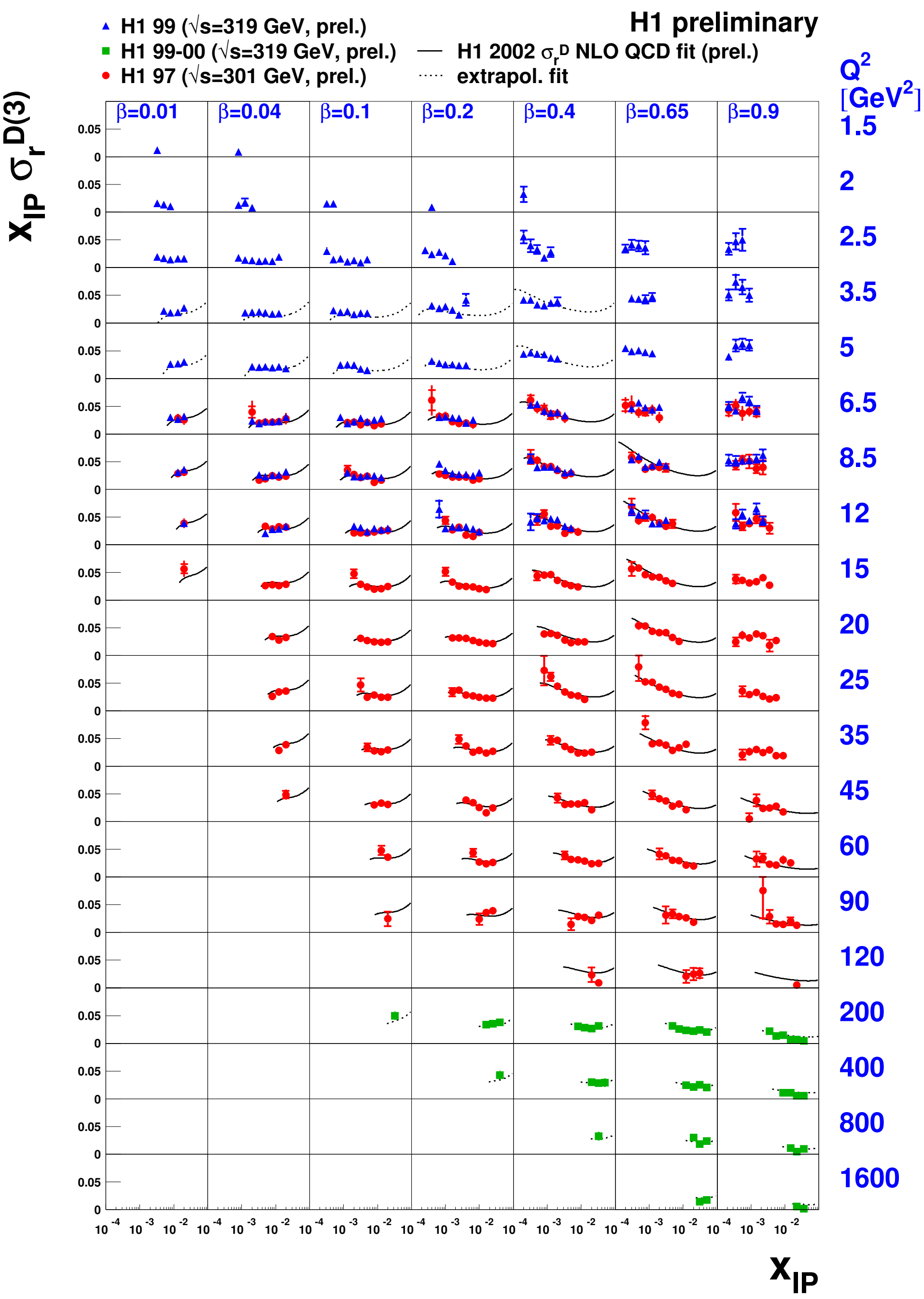

Figure 4.8: The reduced diffractive cross section $x_{I\!P}\sigma_r^{D(3)}(x_{I\!P}, \beta, Q^2)$ shown as a function of $x_{I\!P}$ for fixed β and Q^2. The inner error bars show the statistical error and the outer error bars show the statistical and systematic error bars added in quadrature. The data are compared to a NLO QCD fit performed on the medium Q^2 data.

universal partonic cross sections and diffractive parton distributions [43]. This holds for large Q^2 at fixed x, $x_{I\!P}$ and t. When Regge theory is applied to the diffractive structure functions the Ingelman-Schlein model [44] of a "resolved pomeron" with partonic structure independent of $x_{I\!P}$ and t is obtained. That is the diffractive structure functions may be considered as a flux factor, $f_{I\!P/p}$, for the probability of a pomeron being emitted from the proton and pomeron parton density functions $f_i^{I\!P}$. Therefore the diffractive structure function can be written in terms of a pomeron structure function, $F_2^{I\!P}$, as

$$F_2^{D(3)}(\beta, Q^2, x_{I\!P}) = f_{I\!P/p}(x_{I\!P}) F_2^{I\!P}(\beta, Q^2) \tag{4.23}$$

However, at large $x_{I\!P}$ deviations from equation 4.23 are seen which can be described by adding a sub-leading reggeon term, giving

$$F_2^{D(3)}(\beta, Q^2, x_{I\!P}) = f_{I\!P/p}(x_{I\!P}) F_2^{I\!P}(\beta, Q^2) + f_{I\!R/p}(x_{I\!P}) F_2^{I\!R}(\beta, Q^2) \tag{4.24}$$

where the meson has a reggeon flux $f_{I\!R/p}$ and a meson structure function $F_2^{I\!R}$. A fit of this form to data from the 1994 running period [46], using a reggeon flux factor from previous measurements, yields a pomeron intercept of

$$\alpha_{I\!P}(0) = 1.203 \pm 0.020(\text{stat.}) \pm 0.013(\text{sys.}) \pm^{0.030}_{0.035} (\text{model}) \tag{4.25}$$

Due to the t dependence not being measured a dependence from hadron-hadron data is assumed. The value of $\alpha_{I\!P}(0)$ is much larger than the soft pomeron intercept of 1.08 from hadron-hadron interactions and the value

$$\alpha_{I\!P}(0) = 1.068 \pm 0.016(\text{stat.}) \pm 0.022(\text{sys.}) \pm 0.041(\text{model}) \tag{4.26}$$

from the proton diffractive dissociation cross section in photoproduction [47].

From the factorisation in equation 4.24, $F_2^{I\!P}(\beta, Q^2)$ and $F_2^{I\!R}(\beta, Q^2)$ are the structure functions for deep inelastic scattering off of a pomeron or meson respectively. Therefore, similarly to F_2 for the proton, $F_2^{I\!P}(\beta, Q^2)$ can be expressed in terms of parton distributions

$$F_2^{I\!P}(\beta, Q^2) = \beta \sum_i e_i^2 f_i(x, Q^2) \tag{4.27}$$

where f_i is the parton density function for a parton of family i with charge e_i in the pomeron. This is called the resolved or factorisable pomeron model. With pomeron structure described in terms of parton dynamics evolution equations using pQCD may be applied to the pomeron structure function. The non-perturbative pomeron and meson structure functions can be evolved in Q^2 from a starting point of $Q_0^2 = 3$ GeV^2 using the DGLAP equations. The input distributions used are the quark flavour singlet $zF_q(z, Q^2) = u + \bar{u} + d + \bar{d} + s + \bar{s}$ and gluon $zF_g(z, Q^2)$ distributions, where z is the fraction of the pomeron momentum carried by the struck parton. For a direct coupling of the photon to the parton from the pomeron $z = \beta$, whereas for the photon coupling to a gluon from the pomeron through boson-gluon fusion $0 < \beta < z$. The resulting structure functions show that the pomeron structure is dominated by gluons for the large range of Q^2 measured.

4.3 Diffractive High-p_T Photon Production

In the previous section diffractive DIS events were considered where there is a hard scale present due to a large value of Q^2. Thus it is possible to make pQCD calculations. Another such hard scale is the mass of the particle produced in the X system. This scale becomes important for diffractive production of the heavier vector mesons such as the J/ψ. A further hard scale is provided by the four momentum transfer between the photon and the proton, t, as defined in equation 4.17. Typically diffraction occurs at low t, but at sufficiently large values, $-t \gg \Lambda^2_{QCD}$, a hard scale is present at both the photon and proton ends of the diffractive exchange, not just the photon end. Measurements have been made of double dissociation, rapidity gaps between jets [48] and diffractive vector meson production [49] at large values of t. The measurements of double dissociation and gaps between jets pose theoretical problems due to the possibility of subsequent strong interactions between the hadronic systems destroying the rapidity gap created by the diffractive hard scatter. Diffractive

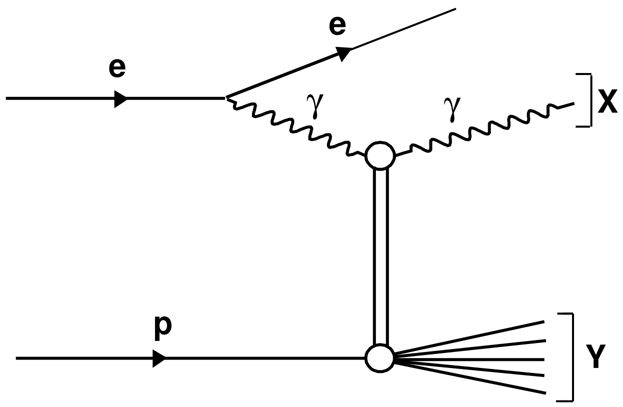

Figure 4.9: Schematic illustration of the process $ep \to e\gamma Y$.

vector meson production $\gamma p \to VX$ avoids such problems but introduces theoretical problems as calculations require knowledge of the vector meson wavefunction.

The diffractive production of photons, $\gamma p \to \gamma Y$ shown in figure 4.9, avoids both the problems of destruction of the rapidity gap and knowledge of the vector meson wavefunction. The X system consists of a single photon so subsequent strong interactions will not occur with the proton remnant. Additionally the splitting of the photon into a quark-antiquark pair is through an electromagnetic interaction. A hard scale is provided from the large transverse momentum of the scattered photon since, from equation 4.17, $(p_T^\gamma)^2 \simeq -t$ in photoproduction. The large momentum transfer also causes the proton to dissociate into the Y system. The hard scatter is hence completely calculable in pQCD and the only non-perturbative input to the calculation is due to the PDFs of the proton.

The scattering amplitude in the high energy (Regge) limit may be written as a convolution of the impact factors for the two external hadronic states at the ends of the diffractive exchange with the BFKL pomeron. The dynamics of the BFKL pomeron are process independent and have been calculated in the leading logarithm approximation. To calculate the $\gamma^\star - \gamma$ impact factor the four couplings of the

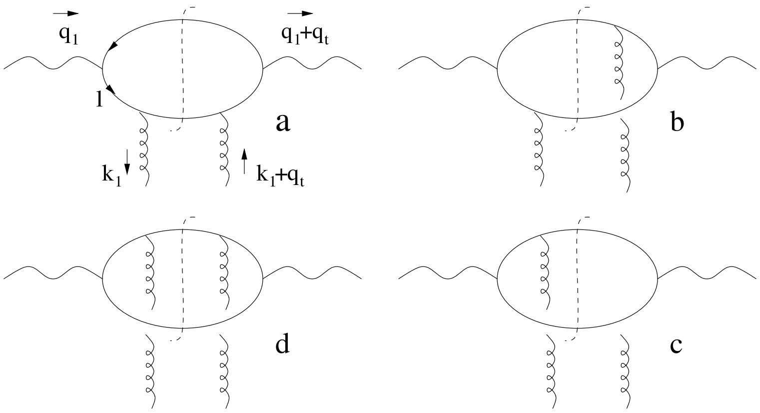

Figure 4.10: The four couplings of two gluons to a quark-antiquark pair from a photon that contribute to the $\gamma^{\star}-\gamma$ impact factor.

gluons from the BFKL pomeron to the quark-antiquark pair from the photon shown in figure 4.10 are considered.

Calculations have been made summing all leading logarithms in the BFKL equation, for the interaction of real incident photons [50] and real and virtual incident photons [51]. A prediction of the process has been included in the HERWIG event generator [52] and is used for the simulation of signal events in this measurement.

Chapter 5

Data Reconstruction and Selection

5.1 Run Selection

The analysis presented in this thesis is based on data collected in the 1999-2000 running period. Data are considered for the analysis if collected in runs in which certain quality criteria were satisfied. The run must have an integrated luminosity of over 0.2 nb^{-1} and must be of a good or medium quality, meaning that all major components of the H1 detector – CJC1, CJC2, LAr and SpaCal – were operational. Additional subdetectors necessary for the analysis must also have their high voltage enabled. For this analysis the iron, time of flight and veto systems must also be operational.

5.2 Subtrigger Selection

The event topology for this analysis, as shown in figure 5.1, consists of three elements – the low Q^2 scattered electron, the backwards final state photon and the dissociated proton system. For the triggering of these events the first two elements

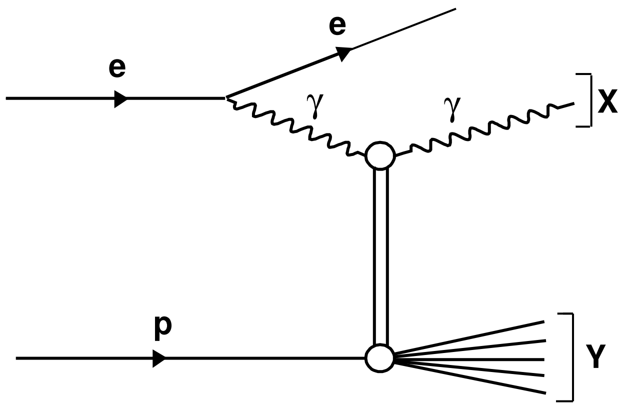

Figure 5.1: Schematic illustration of the process $ep \rightarrow e\gamma Y$.

are considered by using the SpaCal to trigger on the final state photon and the 33 m electron tagger to trigger on the scattered electron. The s0 subtrigger uses the trigger element `SPACAL_IET>2` to trigger on an electromagnetic particle with energy greater than 6 GeV in the SpaCal combined in coincidence with good timing signals from the ToF system and the veto system. The s50 subtrigger uses the luminosity system in addition to the SpaCal by requiring a deposit above threshold in the 33 m electron tagger in coincidence with no signal above threshold in the photon tagger. Hence the SpaCal requirements may be loosened with respect to the s0 requirements. The trigger elements used are `SPACAL_IET>1`, an electromagnetic cluster with energy greater than 2 GeV, or `SPACAL_IET_Cen_2`, a electromagnetic cluster in the central region of the SpaCal above the highest threshold. Additionally there are timing signals from the ToF system and the SpaCal ToF system. At level two the s50 subtrigger also has a requirement that the electromagnetic cluster must be at a radius of greater than 30 cm from the z axis.

Both of the subtriggers used are prescaled, with the s50 subtrigger generally having a lower prescale than the s0 subtrigger. The prescaled rates of the s0 and s50 subtriggers are shown in figures 5.2 and 5.3, respectively. The rate of the s0

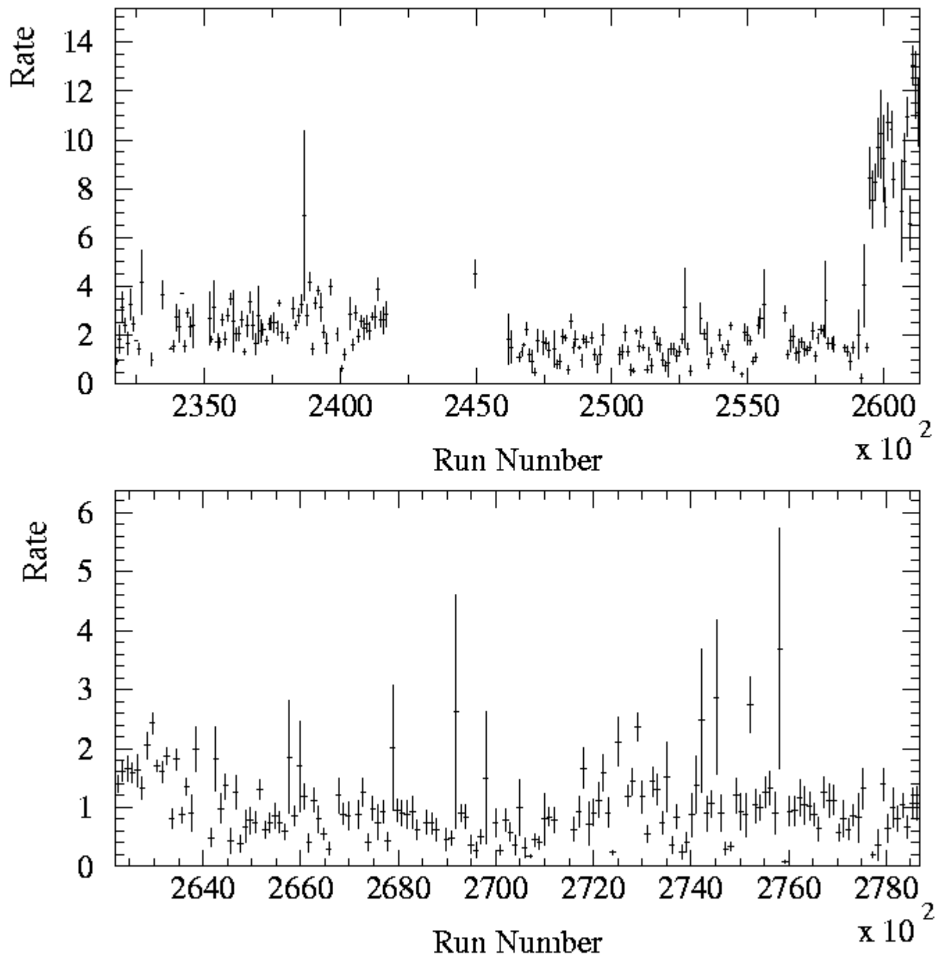

Figure 5.2: The prescaled rate of the s0 subtrigger against run number for the 1999 (top) and 2000 (bottom) running periods.

subtrigger is stable over the running period, with a rate of 2-3 Hz in the 1999 running period and approximately 1 Hz in the 2000 running period. The 'minimum bias' period is seen at the end of the 1999 running by an increase in the s0 subtrigger rate, due to the prescales of all subtriggers being minimised. The s50 subtrigger is stable for the majority of the 1999-2000 running period, collecting data at a rate of 2-3 Hz. However, the subtrigger rate shows more variation in the early 1999 running period.

The integrated luminosity collected by the H1 detector is corrected to account for

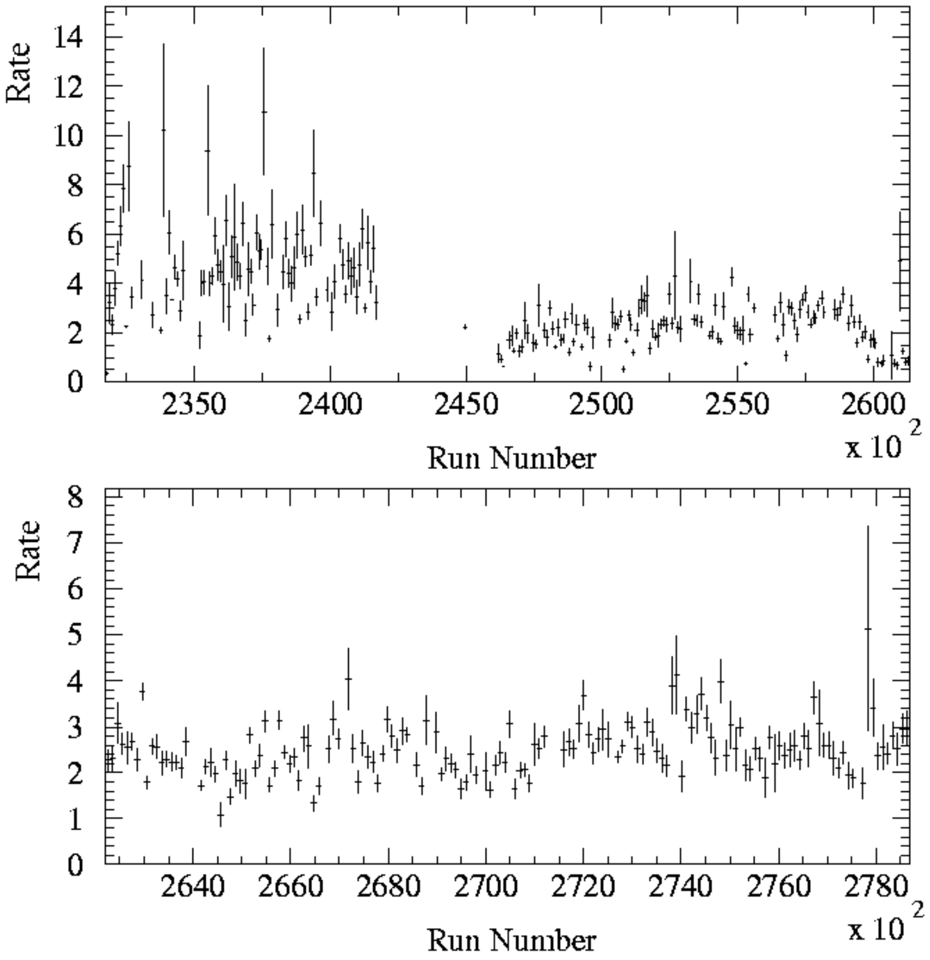

Figure 5.3: The prescaled rate of the s50 subtrigger against run number for the 1999 (top) and 2000 (bottom) running periods.

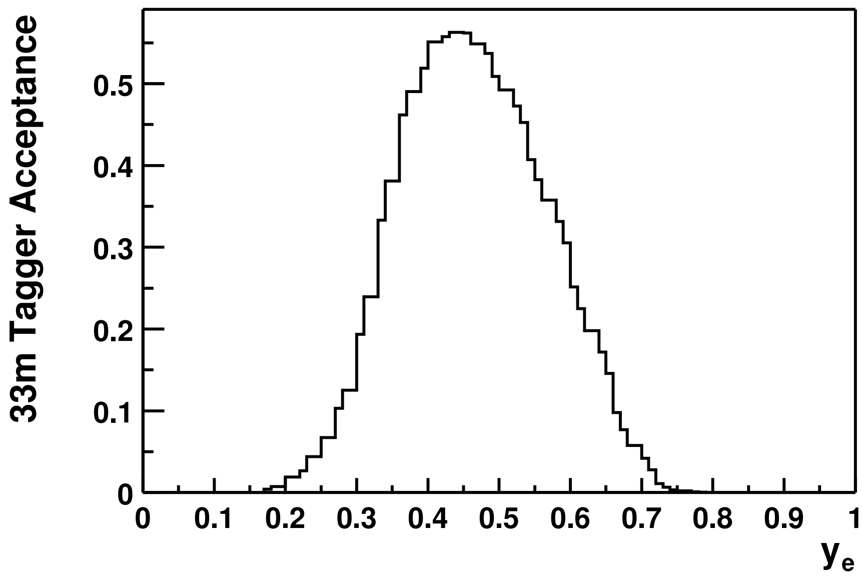

Figure 5.4: The acceptance of the 33 m electron tagger as a function of y_e, averaged over the running period considered.

the prescales of the two subtriggers considered. For each run, the collected luminosity is corrected using the prescale of the enabled subtrigger with the lowest prescale. The corrected integrated luminosity collected in the running period considered by the two subtriggers is 47.6 pb^{-1}.

5.3 Photoproduction Selection

Photoproduction events are selected by detecting the scattered electron in the 33 m electron tagger. This limits the virtuality of the incident photon to $Q^2 < 0.01$ GeV^2. By detecting the scattered electron y may be reconstructed. At a low scattering angle

y may be reconstructed from the energy of the scattered electron by

$$y_e = \frac{E_e - E_{e'}}{E_e} \tag{5.1}$$

Cuts are made to ensure that the tagged electron is within the acceptance of the 33 m tagger. Firstly the x position of the electron cluster must be in the range $|x_{tag}| < 6.5$ cm. Secondly, the event must be within the y acceptance of the 33 m tagger. The average acceptance of the 33 m electron tagger as a function of y_e for the run range considered is shown in figure 5.4. Events are required to be in the range $0.3 < y_e < 0.6$, which restricts the photon-proton centre of mass energy to $175 < W < 247$ GeV . In addition to the 33 m electron tagger, it is required that there are no deposits in the photon tagger above an energy of 2 GeV to veto on background from bremsstrahlung events.

Tagging the scattered electron helps to constrain the kinematics of an event and hence contamination of the event sample by background processes is reduced.

Due to the sensitivity of the electron tagger acceptance to the HERA beam optics, the electron tagger is not described in the simulation of the H1 detector. Hence the scattered electron as measured by the tagger is not available 'out of the box' in any MC used to model tagged photoproduction processes, for instance the signal process measured in this thesis. To provide a pseudo-reconstructed level electron the generator level of the MC may be used. The generator level electron is taken and a smearing applied to reproduce the effect of the tagger resolution. Then a weight is applied using the known acceptance of the 33 m tagger, as shown in figure 5.4, found at the generated value of y_e. Hence the MC event may be nearly as well reconstructed as the data from the H1 detector with the pseudo-reconstructed scattered electron available for the MC.

5.4 Photon Identification and Selection

The scattered photon is detected in the SpaCal and is identified using a SpaCal electron finder. The electron finder identifies electromagnetic particles in the SpaCal by selecting clusters with a small logarithmic weighted cluster radius, $R_{clus} < 4$ cm, and an energy greater than 4 GeV. The electromagnetic particle is then locked to separate the cluster from any subsequent energy sums. The requirement of a small cluster radius helps to separate electromagnetic clusters from hadronic clusters, as generally a hadronic shower has a larger transverse spread than an electromagnetic shower. Only one such isolated electromagnetic particle is required to be found in each event. In addition to cuts on the electromagnetic cluster, the hadronic energy behind the cluster within a radius of 17.5 cm is required to be low, $E_{had} < 0.5$ GeV. This ensures that the cluster is electromagnetic in origin and not a more penetrating hadronic cluster. The electromagnetic section of the SpaCal is approximately 28 interaction lengths deep, so any electromagnetic shower should be fully contained. Thus any deposits of energy in the hadronic section of the SpaCal behind the electromagnetic cluster suggest that the cluster may originate from a hadronic particle. The photon must be detected within the angular range $153° < \theta < 176°$ to avoid leakage of the photon cluster from the edges of the SpaCal and at a radius of $R > 30$ cm to be in the region of the detector allowed by the L2 trigger requirement on subtrigger s50. The photon must also not be in regions of SpaCal cell inefficiency caused by dead or inefficient cells, inefficient trigger channels or varying high voltage. Regions of poor efficiency are determined from data in the 1999 running period [53]. The fiducial cut based on the inefficient cells rejects events when the photon is found in the regions shown in figure 5.5.

The energy of the photon is selected in the range $8 < E_\gamma < 20$ GeV to ensure that the cluster is well measured but without an energy high enough to be close to the energy of a kinematic peak electron.

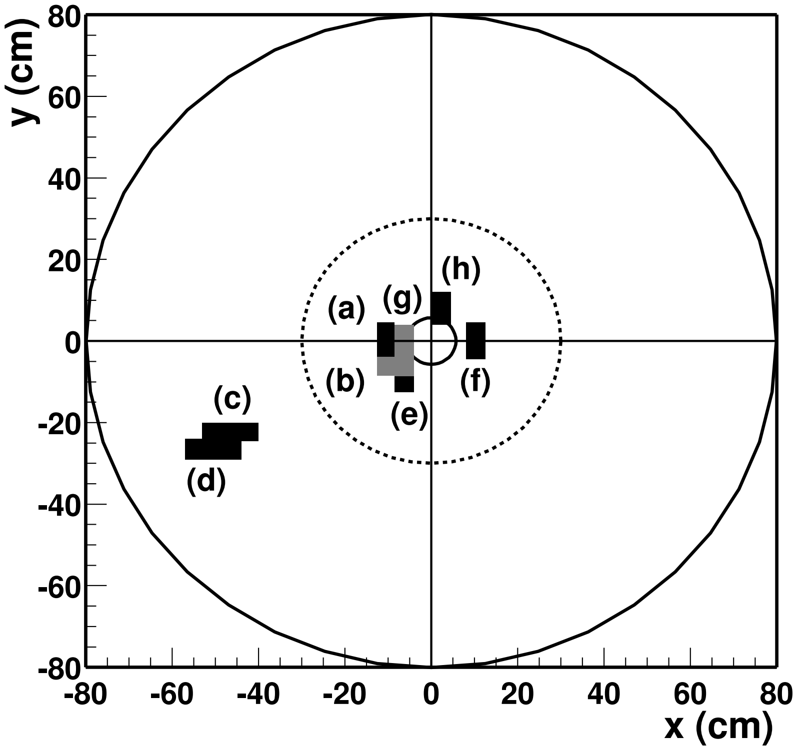

	x_1 (cm)	y_1 (cm)	x_2 (cm)	y_2 (cm)
(a)	-12.5	-4.5	-8.5	4.5
(b)	-12.5	-8.5	-8.4	-4.0
(b)	-53.0	-24.5	-40.0	-20.0
(c)	-57.0	-29.0	-44.0	-24.0
(d)	-8.5	-12.5	-4.0	-8.0
(e)	8.0	-4.5	12.5	4.5
(f)	-8.5	-8.5	-4.0	4.0
(g)	0.0	4.0	4.5	12.0

Figure 5.5: The SpaCal fiducial areas removed from the analysis and the corresponding Cartesian coordinates of the areas. The inner and outer solid circles shown the full volumes of the SpaCal and the dashed line the inner cut on radial position for the scattered photon.

To ensure that the electromagnetic particle is a photon, not an electron, extrapolations of tracks from the CTD and the BST to the electromagnetic cluster are considered. Tracks from both the event vertex and those not associated with the event vertex are extrapolated to the cluster. The electromagnetic cluster is required to have no CTD tracks within a radius of 12 cm to be accepted as a photon. At angles closer to the beampipe the electromagnetic particle is within the angular acceptance of the BST. Hits in the BST associated with the electromagnetic cluster are searched for by considering a "corridor" from the event vertex, or nominal vertex if no vertex is reconstructed, to the electromagnetic cluster [56]. If two or more BST hits are found in the corridor then the electromagnetic particle is validated as an electron. Hence, to identify a photon no validation is required if the cluster is in the angular acceptance of the BST.

Finally, the selected photon must have a large transverse momentum, $p_T^\gamma > 2$ GeV which corresponds to $|t| > 4$ GeV^2, to ensure that a hard scale is present for pQCD calculations.

5.5 SpaCal selection

To ensure that the photon is isolated within the SpaCal requirements are placed on any additional deposits in the SpaCal. The total energy in the SpaCal, after the photon is locked, is required to be less than 2 GeV. In addition the energy of the most energetic cluster in the SpaCal apart from the photon should be less than 200 MeV. This is a comparable value to the noise threshold in the SpaCal.

5.6 Diffractive Variables and Selection

The two important diffractive variables used in this thesis are $x_{I\!P}$ and $y_{I\!P}$, as defined in equation 4.19 and 4.20, respectively. Due to the kinematics of the signal process simplifications to the definitions may be made to allow these quantities to be reconstructed. In tagged photoproduction the photon has a low virtuality, $Q^2 < 0.01$ GeV^2, hence may be neglected. Additionally the proton mass may also be neglected. Therefore equation 4.19 becomes

$$x_{I\!P} \simeq \frac{M_X^2 - t}{W^2} \tag{5.2}$$

If the four momentum transfer squared at the photon vertex is considered

$$t = (q - X)^2 \simeq M_X^2 - 2q.X = M_X^2 - 2E_\gamma \sum (E + p_z)_X \tag{5.3}$$

where the assumption is made that the incident photon only has a z component of momentum. Similarly, $W^2 = 4E_\gamma E_P$. Hence, equation 5.2 becomes

$$x_{I\!P} = \frac{\sum(E + p_z)_X}{2E_P} = \frac{(E + p_z)_\gamma}{2E_P} \tag{5.4}$$

as the X system consists solely of the scattered photon. Therefore $x_{I\!P}$ maybe be reconstructed using only the scattered photon. Similarly, $y_{I\!P}$ may be simplified, firstly to

$$y_{I\!P} = \frac{M_Y^2 - t}{W^2} \tag{5.5}$$

and further by considering the four momentum transfer at the proton vertex to

$$y_{I\!P} \simeq \frac{\sum_Y (E - p_z)}{2E_\gamma^{in}} \tag{5.6}$$

where the sum in the numerator is made over the $E-p_z$ of particles in the Y system, that is all particles in the event apart from the scattered electron and photon, and E_γ^{in} is the energy of the incident photon. Experimentally the sum over the Y system is over the $E-p_z$ as measured by the LAr calorimeter, using a combination of clusters and tracks. A hadronic final state (HFS) algorithm is used that takes the cluster to reconstruct its energy at large energies whereas any track linked to the cluster is used to reconstruct the cluster energy at low energies. This is due to the cluster energy being reconstructed well at high energies but poorly at low energies, whereas the converse is true for tracks, a low energy track is reconstructed well and a high energy track poorly. Further details of the algorithm may be found in [54,55]. Being based on an $E - p_z$ sum, $y_{I\!P}$ is relatively insensitive to losses of particles along the beam pipe in the positive z direction, for which $E \simeq p_z$. The Y system, originating from the dissociated proton, is seen in the positive z hemisphere and is particularly likely to have particles lost along the beam pipe in the positive z direction.

Diffractive events are selected using the variables $y_{I\!P}$ and the rapidity gap between the photon and the edge of the Y system, $\Delta\eta$. A cut is made selecting low values of $y_{I\!P} < 0.018$, to ensure a low mass of the Y system and hence a large rapidity gap.

The size of the rapidity gap between the scattered photon and the edge of the Y system, $\Delta\eta$, is determined by the difference in rapidity between the most backwards HFS particle in the event and the scattered photon. The HFS algorithm, described previously in this section, provides a list of particles with energy greater than 0.05 GeV and the most backwards particle is found. Any particles within a cone of radius $R = 1$ in $\eta - \phi$ space around the scattered photon are not considered due to the possibility of the photon cluster spreading out further than the cluster assigned to the photon. The cut of $\Delta\eta > 2$ ensures a large and clean rapidity gap for the diffractive event.

A further pair of cuts are used to veto against large multiplicities in the central region. The number of vertex and non-vertex fitted tracks in the CTD are each required to be fewer than 10. These cuts are motivated by the low multiplicity expected from the signal events due to requirements for the Y system to have a low mass and be well separated from the scattered photon.

5.7 Event Selection

Several additional event variables are useful in helping to reduce background processes in the final sample of events. The total $E - p_z$ of an event is well known in the initial state of collisions and is conserved. If particle masses are neglected, the initial state proton has four vector $(E_p, 0, 0, E_p)$ and the electron has four vector $(E_e, 0, 0, -E_e)$, where the energy of the proton $E_p = 920$ GeV and the energy of the electron $E_e = 27.6$ GeV for the running period considered. Therefore the proton has $E - p_z = 0$ and the total initial $E - p_z$ is due to the incident electron, given by $E - p_z = 2E_e = 55.2$ GeV. Since $\sum(E - p_z)$ is conserved a good, well reconstructed physics event has a final state with $\sum(E - p_z) = 55.2$ GeV. Any background introduced from cosmic muons, beam halo muons or an additional event overlapping with a good ep physics event will cause extra $E - p_z$ to be reconstructed. Due to detecting the scattered electron in the 33m electron tagger, the scattered electron has a low scattering angle. Hence the total $E - p_z$ is given by

$$\sum(E - p_z) = \sum(E - p_z)_{det} + 2E_{e'} \tag{5.7}$$

where $\sum(E - p_z)_{det}$ is a sum over the main H1 detector and $E_{e'}$ the scattered electron energy as measured by the electron tagger. A cut of $45 < \sum(E - p_z) < 65$ GeV is used to select events for the final sample.

Another useful variable for rejecting background is the z position of the event vertex. A good ep physics event in H1 has a vertex near to the nominal vertex position of $(x, y, z) = (0, 0, 0)$ cm. The vertex must be reconstructed from the Y system for the diffractive high t photon events considered in this thesis, as the scattered electron passes along the backward beam pipe and the photon leaves no track. However, it is only possible to reconstruct a vertex when a portion of the Y system passes through the FTD or the forward part of the CTD. The cut on $y_{I\!P}$ places an upper limit on M_Y, but not a lower limit. Thus there is no requirement that the Y system must be seen in the H1 detector, so a vertex may not be reconstructed. Therefore only if a vertex is reconstructed is it required to be in the range $|z| < 35$ cm.

5.8 Selection Summary

The full list of reconstructed cuts used for the selection of diffractive high t photons in this thesis is shown in table 5.1.

5.9 Kinematic Selection

A kinematic selection is placed on the hadron level of the Monte-Carlo events used to simulate the signal and any background processes. This selection is defined by the kinematic cuts used at the detector level which are based on both the acceptance of the H1 detector and theoretical phase space requirements. The cross section measured from the data is defined by this phase space and corrected back to the phase space defined by the kinematic selection. The hadron level cuts are as follows:

- $Q^2 < 0.01$ GeV^2
- $175 < W < 247$ GeV
- $0.1 < x_{I\!P} < 0.7 \times 10^{-3}$
- $y_{I\!P} < 0.018$
- $p_T^\gamma > 2$ GeV

The cuts on Q^2 and W are due to the acceptance of the 33 m electron tagger limiting the phase space of the measured data events. The $y_{I\!P}$ cut limits the sample to events with large rapidity gaps. Finally the cut on p_T^γ ensures that the events

Trigger	s50 OR s0
Electron	$0.3 < y_e < 0.6$ $\|x_{tag}\| < 6.5$cm $E_{phtag} < 2$ GeV
Photon	$8 < E_\gamma < 20$ GeV $153^\circ < \theta_\gamma < 176^\circ$ $R > 30$ cm $p_T^\gamma > 2$ GeV $R_{clus} < 4$ cm Hadronic energy behind $\gamma < 0.5$ GeV Track-Cluster Radius > 12 cm No Validation from BST SpaCal Fiducial Cuts
Event	$45 < E - p_z < 65$ GeV $\|z_{vertex}\| < 35$cm (if reconstructed) Number EM Particles = 1 SpaCal Energy < 2 GeV E(SpaCal HFS) < 200 MeV
Diffractive	$y_{I\!P} < 0.018$ $\Delta\eta > 2$ Number Vertex Fitted Central Tracks < 10 Number Nonvertex fitted Central Tracks < 10

Table 5.1: A summary of the reconstructed level selection for diffractive high t photon events.

have a large four momentum transfer so there is a hard scale present for pQCD calculations.

5.10 Background Processes

Physics processes that may fake the signal process, therefore forming a background, must be investigated to quantify the effect of such backgrounds on the number of events selected as the signal process. Two important forms of background processes are investigated here – firstly those which may produce a similar or identical final state, in this case the Bethe-Heitler and DVCS processes, the diffractive production of ω vector mesons and the overlap of two events to give a tagged electron and a final state photon. Secondly those background processes where elements of the final state are mis-identified, therefore mimicking the signal, in this case inclusive diffraction in photoproduction.

5.10.1 DVCS and Bethe-Heitler

Deeply Virtual Compton Scattering (DVCS), shown in figure 5.6 (a), is the diffractive process $ep \rightarrow e\gamma p$ and therefore consists of a final state similar to that of the signal process if a low mass Y system is produced from the dissociated proton. However the kinematics of DVCS are different to those for the high t diffractive photon production considered in this thesis and hence the event topologies are different. The DVCS process is in the phase space of Q^2 greater than a few GeV^2, hence the 'virtual' part of the name, and generally at small values of t. Therefore the hard scale in the event is provided by Q^2 and not the four momentum transfer t. Experimentally the scattered electron is seen in the main part of the H1 detector, the SpaCal or perhaps the LAr, instead of passing along the backwards beampipe and the photon is seen more forward in the LAr calorimeter. For this reason the DVCS

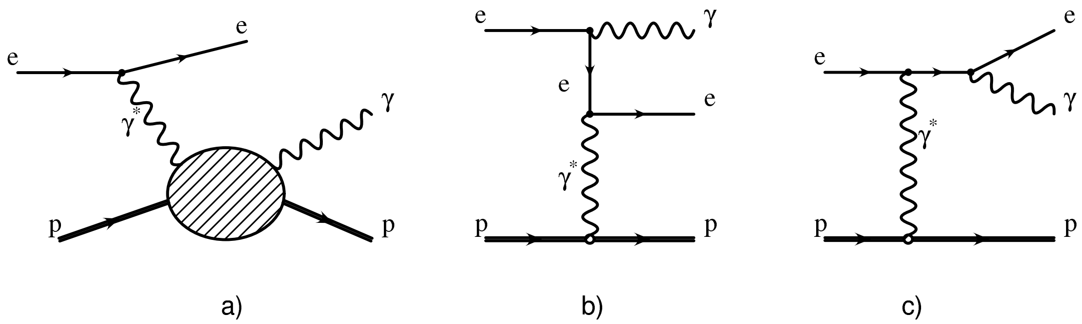

Figure 5.6: Schematic diagrams of (a) the DVCS and (b) and (c) the Bethe-Heitler processes.

contribution to the signal process is negligible.

The same final state $ep \rightarrow e\gamma p$ may be produced by the Bethe-Heitler process, as shown in figure 5.6 (b) and (c). The process is purely electromagnetic and proceeds via bremsstrahlung from the electron line either before or after interaction with the proton. Hence the cross section is largest when the final state electron and photon are in the backwards direction. As with DVCS, the kinematics of this process are important in distinguishing such events from the signal process. In the Bethe-Heitler process the transverse momentum of the final state photon, p_T^γ, must balance the p_T of the final state electron. As the scattered electron is tagged in this analysis it effectively has $p_T^e = 0$, hence for a final state with a photon at high p_T the background from Bethe-Heitler is negligible.

5.10.2 Diffractive ω Production

Another diffractive process which may mimic the high t photon final state is diffractive vector meson production with a subsequent decay into electromagnetic particles. Diffractive ω production is considered as it is the lightest of the vector mesons that decays to exclusively electromagnetic particles. This occurs through the direct channel $\omega \rightarrow \pi^0\gamma$, with almost all subsequent decays of the π^0 producing two more photons, and the channel $\omega \rightarrow \pi^+\pi^-\pi^0$, where any photons occur from the subsequent π^0 decay $\pi^0 \rightarrow \gamma\gamma$. These decays represent 8.7% and and 89.1% of the ω decays respectively with the main other contribution coming from the channel $\omega \rightarrow \pi^+\pi^-$ at the level of 1.7%. Only vector mesons may be produced in diffraction, since the diffractive exchange carries vacuum quantum numbers and so the quantum numbers of the photon must be preserved. Thus the ω is the lightest particle which need be considered from diffractive production.

For diffractive ω production to mimic the diffractive high t photon signal the production must also be at high t so that the ω is within the SpaCal acceptance. Additionally the decay product that mimics the candidate photon must have a high energy (greater than 8 GeV). Hence the ω decay products travel backwards and the decay products remaining after the 'photon' has been identified have low energies. Additionally, due to the high energy of the ω, the decay products become collimated and hence some or all of the particles overlap, mimicking the scattered photon in the signal process. A sample of diffractive ω events was produced using the DIFFVM event generator [57]. The cut that requires the most energetic cluster in the SpaCal, after the photon cluster is locked, to have an energy of less than 200 MeV is effective in rejecting any diffractive ω events that pass the rest of the selection. However, due to the non-candidate photon decay particles having low energies, 5 events from the 100,000 generated passed all cuts. Thus the effect on the final sample was estimated.

Unfortunately neither the slope or normalisation of the t dependence are known for diffractive ω production at high t. For instance the ZEUS measurement [58] only extends to $t < 0.6$ GeV^2. However other measurements of diffractive vector meson production may be used to provide an estimate of the cross section and hence the absolute number of events in the final sample. The measurement of diffractive J/ψ production at H1 [49] found a t slope of the form $(-t)^{-n}$ with $n = 3.00 \pm 0.08(\text{stat.}) \pm 0.05(\text{sys.})$. Hence the t slope used in the DIFFVM generator for diffractive ω production was reweighted to this form. The normalisation of the J/ψ t cross section was also considered. Predictions from SU(4) state that the ratio of vector meson production cross sections in the interaction $\gamma \rightarrow V$ is:

$$\sigma_{\rho^0} : \sigma_\omega : \sigma_\phi : \sigma_{J/\Psi} = 1 : 1/9 : 2/9 : 8/9 \tag{5.8}$$

Measurements of the ratios of diffractive vector meson production cross sections at ZEUS [60] show that the SU(4) prediction for ρ^0, ϕ and J/ψ is good at high values of t or Q^2, lending confidence that the ratios in equation 5.8 may be used to estimate the cross section for the diffractive production of ω mesons. Therefore the normalisation of the J/ψ differential t cross section was taken and the ratio of cross sections applied to give a normalisation for the ω. Thus both the slope and normalisation of the ω cross section were estimated. For the luminosity considered the diffractive ω background in this measurement was estimated to be 0.03 events and hence is negligible.

5.10.3 DIS Overlap

Another background that may fake the topology of the signal events is caused by two events overlapping each other. If a DIS event with the scattered electron in the SpaCal is overlapped with a photoproduction or Bethe-Heitler event that contains an electron tagged in the 33 m electron tagger the topology of the high t diffractive photon events is mimicked. The requirement of no track being linked to SpaCal electromagnetic cluster vetoes any electrons with a well reconstructed track. For the Bethe-Heitler process a photon will be seen along the backwards beampipe in addition to the scattered electron. Thus the veto on the photon tagger by requiring the energy $E < 2$ GeV is useful for rejecting this background. Finally the sum of the final state $E - p_z$ is important for rejecting background from overlap events. For two fully reconstructed events overlapping each other $\sum(E-p_z) = 110.4$ GeV, thus outside of the cut range $45 < \sum(E-p_z) < 65$ GeV. The possibility of overlap events

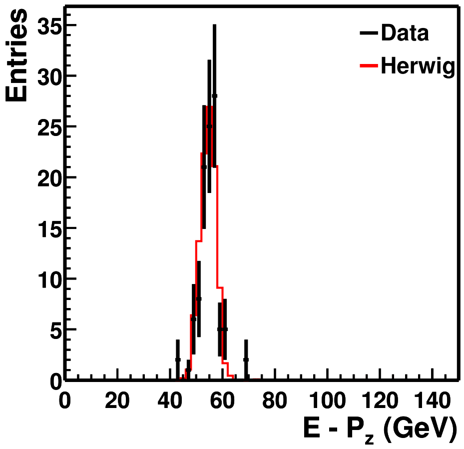

Figure 5.7: The $\sum(E-p_z)$ distribution for the full event sample with the $\sum(E-p_z)$ cut removed. Data (crosses) are compared to the prediction from HERWIG (solid line). The HERWIG prediction is normalised to the data.

contaminating the signal process was investigated by removing the $\sum(E-p_z)$ cut and observing the distribution of $\sum(E-p_z)$, a shown in figure 5.7. The presence of few extra events, and certainly no events in the range where overlap events are expected to be seen, leads to the conclusion that the background from DIS overlap is negligible.

5.10.4 Inclusive Diffraction

The background contribution from inclusive diffractive processes $\gamma p \to Xp$ in photoproduction was also considered. It is possible that a single electromagnetically interacting particle from such processes may fake the photon candidate in the SpaCal and all other hadronic activity either falls below noise cuts in the SpaCal or is not detected. To investigate this possibility the PHOJET event generator [59] was used to simulate these inclusive diffractive processes. From 11 pb^{-1} of simulated events

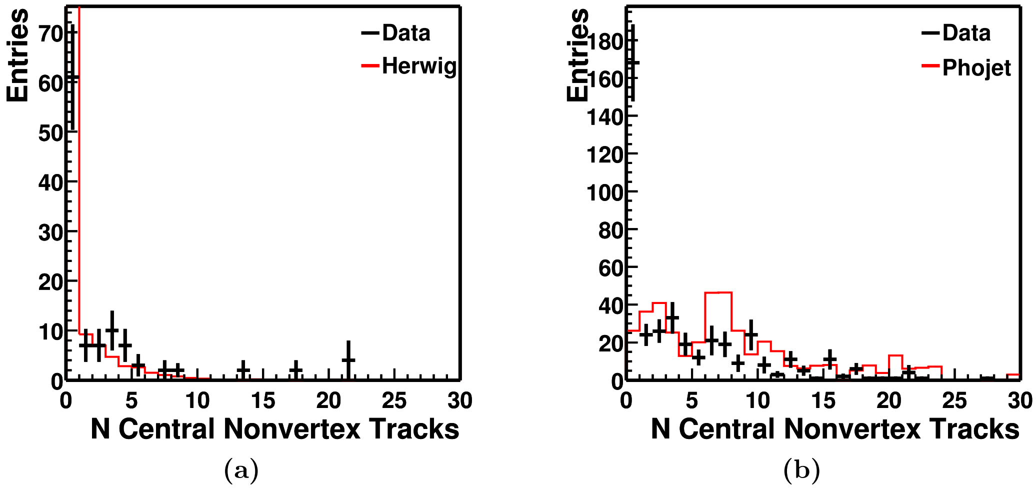

Figure 5.8: The multiplicity of non-vertex fitted central tracks for (a) the full selection, as stated in table 5.1, with the track multiplicity cuts removed, comparing data (points) to the HERWIG prediction and (b) the loose selection defined in section 5.10.4, comparing data (points) to the PHOJET prediction.

no events passed the full analysis cuts. However, an estimate was made of any contribution that could be made to the signal events by investigating this background further by loosening the cuts to only

- $8 < E_\gamma < 20$ GeV
- $153^\circ < \theta_\gamma < 176^\circ$
- $p_T^\gamma > 2$ GeV
- Track link cuts (no vertex or non-vertex tracks and no BST validation)
- $0.3 < y_e < 0.6$
- $45 < \sum(E - p_z) < 65$ GeV
- $\Delta\eta > 2$

These loosened cuts provided a sample of events from the PHOJET generator which could be compared to data. Of particular interest were the distributions of the number of tracks found in the CTD. Both the distributions of vertex fitted tracks and non-vertex fitted tracks (figure 5.8(b)) show events with large multiplicities which are also seen in the data with the full selection, but no cut on track multiplicities (figure 5.8(a)). In the full selection a cut is placed requiring both of these multiplicities to be less than 10. Thus the PHOJET sample with the loosened cuts was normalised to the data using the number of events with tracks above a multiplicity of 10. From this an estimate of the background in the $x_{I\!P}$ and t distributions may be formed from the PHOJET distributions of these variables with the loosened cuts and the normalisation. A correction for this estimated background was then made on a bin-by-bin basis by subtracting half of the background from the signal events and assigning the other half of the background as a systematic error.

5.11 Control Distributions

This section shows the data selected by the full cuts listed in table 5.1 and the description of this data by the HERWIG prediction of the signal process. The data points take into account the L4 weight of each event w_i, as described in section 2.8, and hence the error bars show the appropriate statistical error given by $\sqrt{\sum_i w_i^2}$. The selection, listed in table 5.1, selects a sample of 66 events which, when the L4 weight is taken into account, corresponds to 99 weighted events.

Figure 5.9 shows the energy, p_T, θ and ϕ distributions for the scattered photon measured in data compared to the HERWIG prediction. The HERWIG prediction is normalised to the data. The photon energy distribution is described reasonably by the MC, especially the position of the peak. The photon p_T distribution is also reasonably described, with the steeply falling distribution seen in both the data and MC. However, it should be noted that the slope of the p_T distribution is very

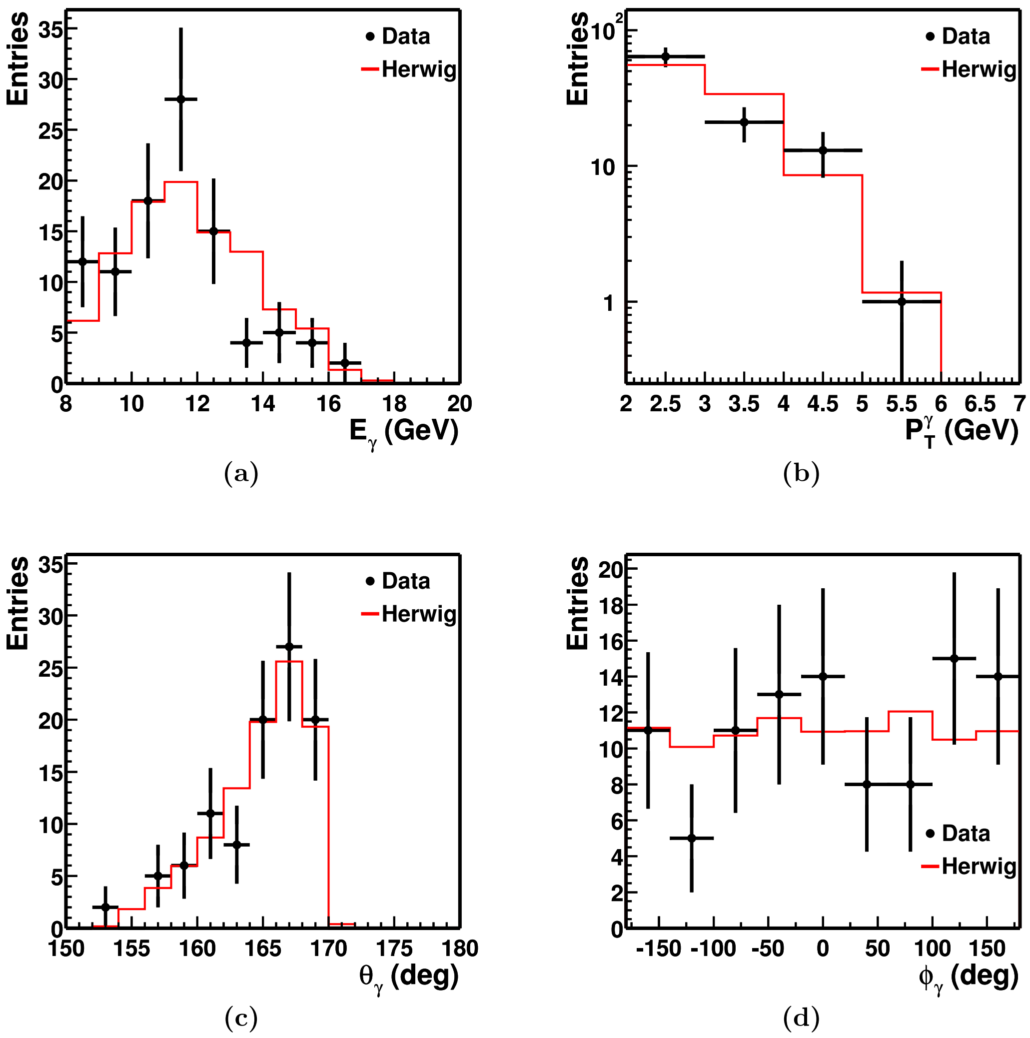

Figure 5.9: The (a) energy, (b) transverse momentum, (c) theta and (d) phi distributions of the scattered photon for data (crosses) compared to the prediction from HERWIG (solid line). The HERWIG prediction is normalised to the data.

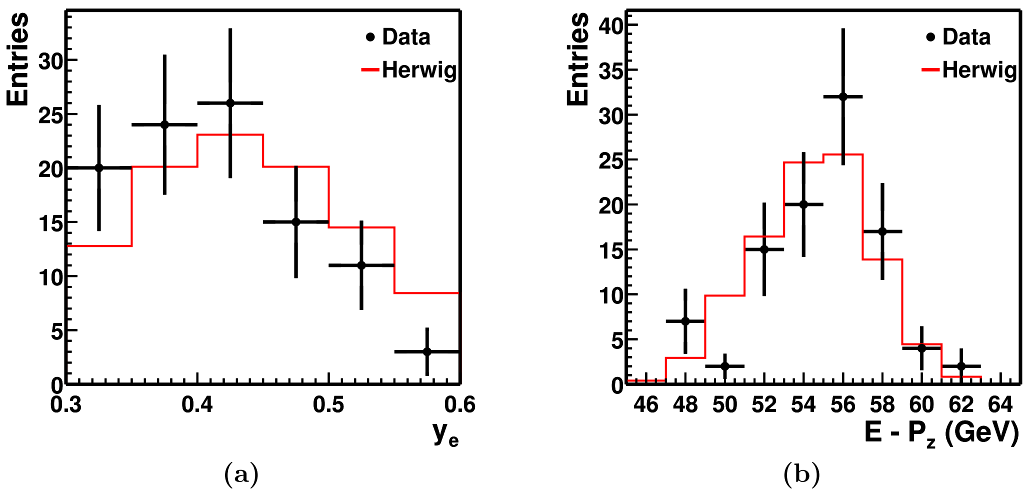

Figure 5.10: The (a) y_e and (b) $\sum(E-p_z)$ distributions for data (crosses) compared to the prediction from HERWIG (solid line). The HERWIG prediction is normalised to the data.

sensitive to the input variables to the HERWIG simulation, in particular the value of α_s. Both the photon θ and ϕ distributions are well described. The θ distribution peaks high values of θ, where the photon is closer to the scattered electron direction, corresponding to lower values of p_T. The effect of the $R > 30$ cm cut is seen by the sharp cutoff at approximately 170°. The ϕ distribution is flat over the full range, as expected. However, with the low statistics and hence the wide binning, any ϕ structure of the SpaCal seen in other analyses is not observed.

Figure 5.10 shows the y_e distribution and the $E - p_z$ distributions of the data compared to the HERWIG prediction. The y_e distribution is reasonably described. The shape of the distribution shows the effect of the 33 m electron tagger acceptance in both the data and the MC, with a peak at $y_e \simeq 0.4$. However the MC does seem a little shifted compared to the data distribution. The $\sum(E - p_z)$ distribution is also reasonably described – a peak is seen at $\sum(E-p_z) \simeq 55$ GeV in both the data and the MC.

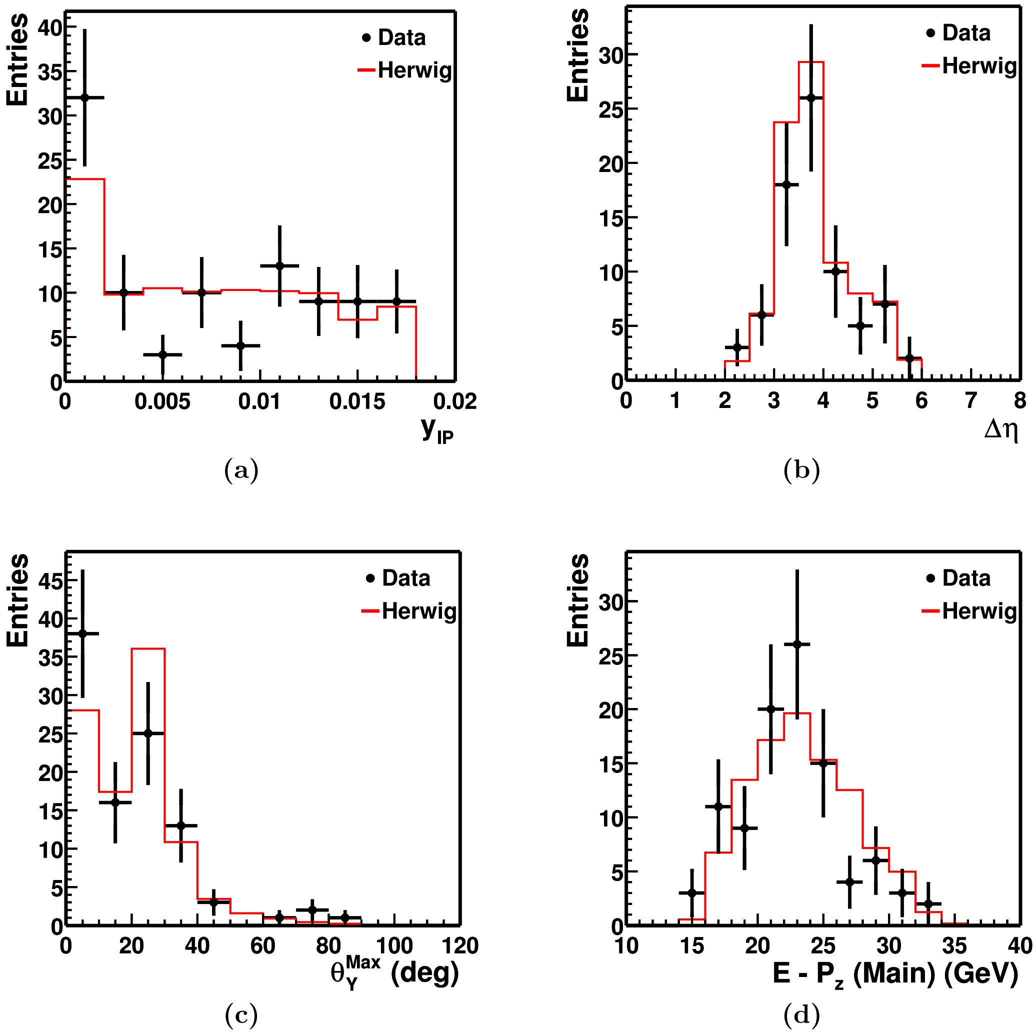

Figure 5.11: The (a) $y_{I\!P}$, (b) $\Delta\eta$, (c) angle of the edge of the Y system and (d) $\sum(E - p_z)$ excluding the electron taggers distributions for data (crosses) compared to the prediction from HERWIG (solid line). The HERWIG prediction is normalised to the data.

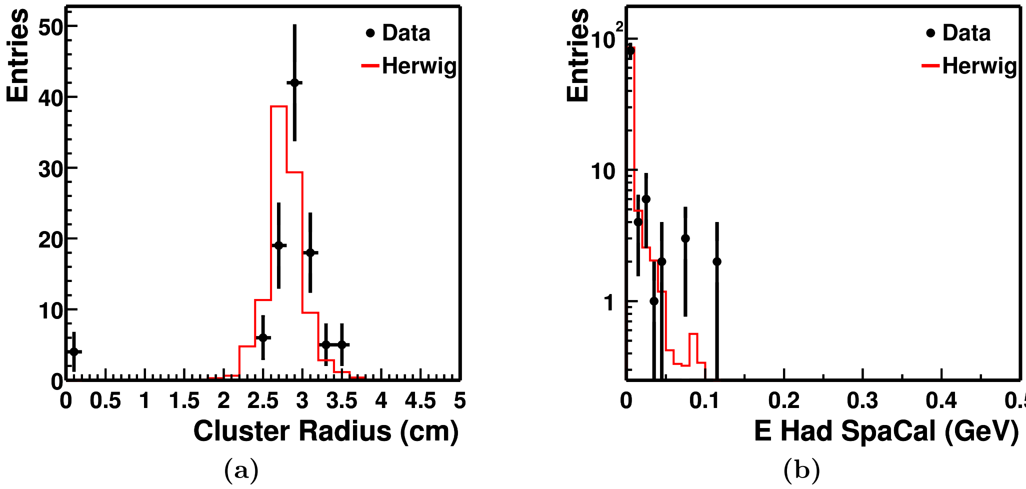

Figure 5.12: The distribution of (a) cluster radius of the photon cluster and (b) hadronic energy behind the photon for data (crosses) compared to the prediction from HERWIG (solid line). The HERWIG prediction is normalised to the data.

Figure 5.11 shows the distributions of $y_{I\!P}$, $\Delta\eta$, angle of the edge of the Y system and $\sum(E - p_z)$ for the main part of the H1 detector for data compared to the HERWIG prediction. The $y_{I\!P}$ distribution is well described by the MC. Both distributions show a flat dependence for most of the range with more events in the lowest bin. This is due to the Y system not dissociating enough to be seen in the forward section of the LAr calorimeter, hence the reconstructed value of $y_{I\!P} = 0$. The $\Delta\eta$ distribution is well described showing that the relative positions of the photon and the edge of the Y system in the detector are well modelled. This is seen in the distribution of the angle of the edge of the Y system which is well described. The peak at $\sim 20°$, arising from the angular acceptance of the CTD, is seen in both data and MC. While the peak at low values of θ_Y^{Max} is seen for both data and MC there is an excess of data over the MC. Again this is due to the Y system passing along the forward beampipe, hence not being detected. The $\sum(E - p_z)$ without the electron tagger is also decently described by the MC, showing that main part of the H1 detector is understood and any treatment of the electron tagger acceptances does not produce untoward effects.

Figure 5.12 shows the distributions of the cluster radius of the photon and the energy in the hadronic SpaCal behind the photon. The photon cluster radius is small, showing that the photon clusters are due to electromagnetically induced showers. The hadronic energy behind the photon is also low, again showing that the hadronic content of the photon shower is low.

Chapter 6

Cross Section

The one dimensional cross section for a bin i in a distribution is defined as

$$\sigma_i = \frac{N_i}{A_i \varepsilon_i b_i \mathcal{L}} \tag{6.1}$$

where N_i is the number of events reconstructed in bin i of the distribution, A_i is the detector acceptance of the bin, ε_i is the trigger efficiency, b_i is the width of bin i and $\mathcal{L}$ is the integrated luminosity. The photon-proton cross section, $\sigma_i^{\gamma p}$, may be considered by calculating the flux of photons at the electron-photon vertex for each bin in the cross section, f_i, therefore relating to the electron-proton cross section, σ_i^{ep}, by

$$\sigma_i^{ep} = f_i \sigma_i^{\gamma p} \tag{6.2}$$

The following sections describe the acceptance, purity and stability measurements, the trigger efficiencies, systematic error analysis and photon flux calculations used in the measurement of the final cross sections presented in chapter 7.

6.1 Resolution, Acceptance, Purity and Stability.

Any detector used to make a measurement, no matter how well designed and constructed, has a finite geometric acceptance, non-zero resolution and inefficiencies. This causes inaccuracy in measuring the final state of a particle physics event and hence inaccuracies in the values of interest for a measurement. Therefore, migrations may occur between bins of cross sections and across cut boundaries. By using a MC that describes the observed data well, the resolutions of measured quantities and acceptances of bins in cross sections may be estimated and hence the detector effects can be corrected for. Thus the cross section at hadron level, rather than detector level, may be measured. In this thesis the HERWIG event generator is used to model the signal events.

The binning of the final cross sections should be chosen such that the bin widths are larger than the width of the resolution of the given variable, thus reducing the effects of migrations. They should also have a reasonable acceptance, again showing that migrations are not too large. Finally each bin should contain enough data for the cross section to be reasonably measured.

6.1.1 Resolution

The resolution for a variable x, σ_x, is calculated by taking the ratio of the value at reconstructed level x_{REC} to the value at generator level x_{GEN} using the MC simulation of the signal events

$$\sigma_x = \frac{x_{REC}}{x_{GEN}} \tag{6.3}$$

The resolution for $x_{I\!P}$ and t are shown in figure 6.1. The $x_{I\!P}$ resolution has an RMS width of $\sigma_{x_{I\!P}} = 0.251$ and the t resolution has an RMS width of $\sigma_t = 0.255$. For both distributions the width of the resolutions measured are smaller than the bin widths used in the final cross sections.

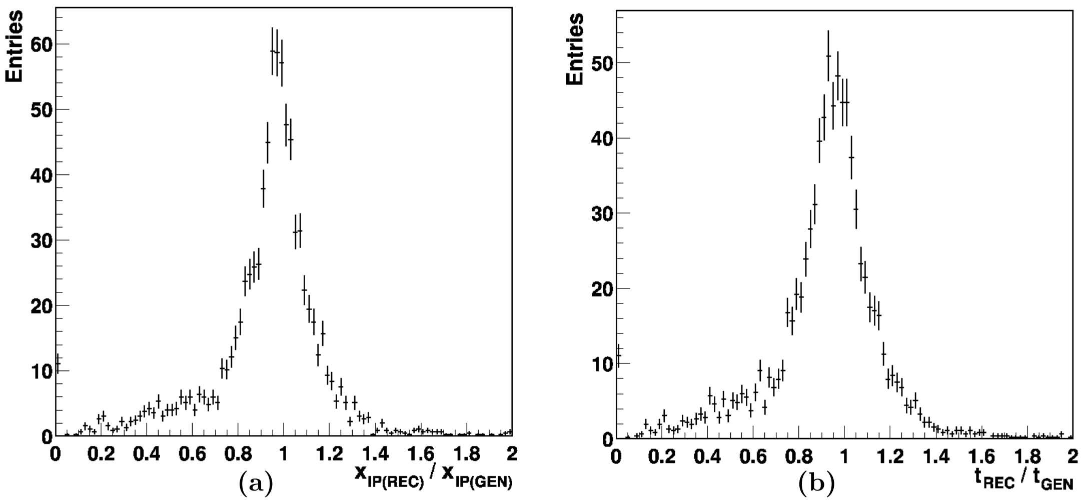

Figure 6.1: The (a) $x_{I\!P}$, and (b) t resolutions.

6.1.2 Acceptance

The acceptance, A, compares generator level events and reconstructed events of a MC simulation on a bin-by-bin basis for a cross section. It is calculated for a bin i by taking the ratio

$$A_i = \frac{N^i_{REC}}{N^i_{GEN}} \tag{6.4}$$

where N^i_{REC} is the number of events in bin i at reconstructed level and N^i_{GEN} is the number of events in bin i at generator level.

The acceptances for the $x_{I\!P}$ and t cross sections are shown in figure 6.2. The acceptance of the $x_{I\!P}$ distribution is above 35% and the acceptance of the t distribution is at least 40% in the measured range.

Both distributions have the middle bin or bins with a higher acceptance due to the steeply falling distributions causing smearing into the bin from lower bins. The highest and lowest t bins have lower acceptances due to being at the edges of the angular range of the final state photon. At low p_T, hence low t, the photon is near to the radius cut, whereas at high t the photon is towards the outer edge of the

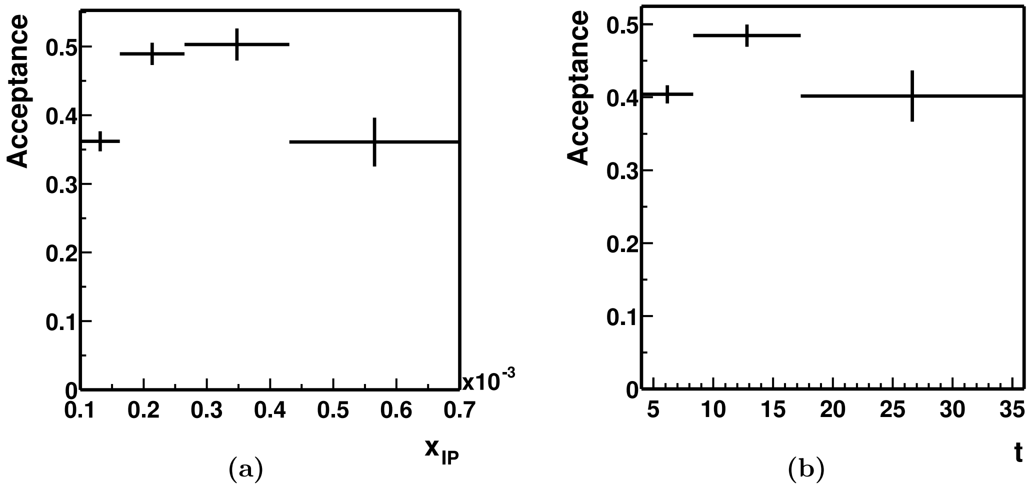

Figure 6.2: The (a) $x_{I\!P}$, and (b) t acceptances.

SpaCal.

6.1.3 Purity

The effect of migrations from a bin may be quantified using the purity, P. This is given for a bin i by the ratio

$$P_i = \frac{N^i_{GEN+REC}}{N^i_{GEN}} \tag{6.5}$$

where $N^i_{GEN+REC}$ is the number of events reconstructed in a bin i that were also generated in the same bin. Thus the purity of a bin is complementary to the acceptance. For instance, the acceptance may be unity if all generated events that have smeared out of the bin are replaced by the same number of events from other bins. However, this would result in a purity of zero.

The purities for the $x_{I\!P}$ and t cross sections are shown in figure 6.3. Both purities are high, but slowly decrease over the range measured.

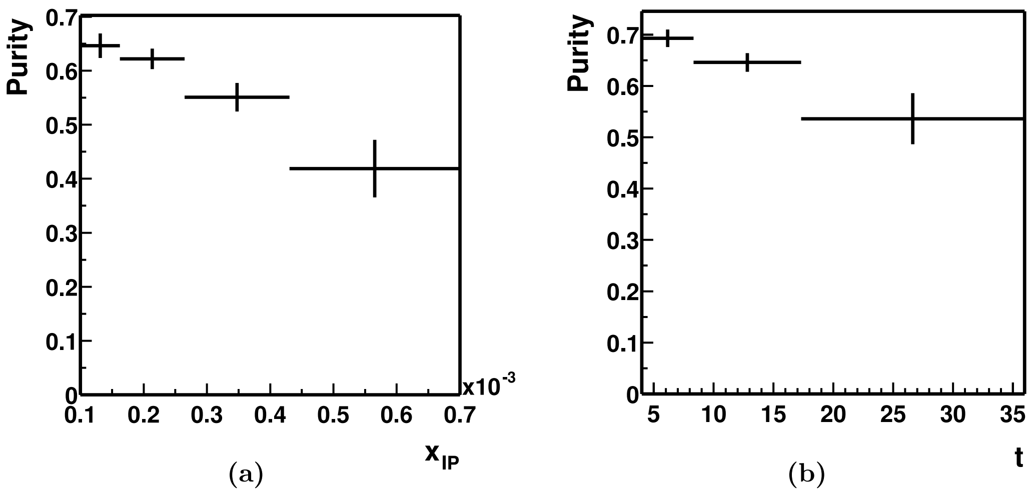

Figure 6.3: The (a) $x_{I\!P}$, and (b) t purities.

6.1.4 Stability

The stability, S, also quantifies the effect of migrations between bins, but considers that events may migrate out of the sample. This is calculated by taking the ratio of events that are reconstructed in the same bin as they are generated without taking into account events that are lost from the event sample. In other words for a bin i the ratio

$$S_i = \frac{N^i_{GEN+REC}}{N^i_{GEN+REC'}} \tag{6.6}$$

where $N^i_{GEN+REC'}$ is the number of events generated in bin i that were reconstructed somewhere within the event sample.

The stabilities for the $x_{I\!P}$ and t cross sections are shown in figure 6.4. The stability of the t distribution is of a similar shape to the stability distribution, but with a higher normalisation, whereas the $x_{I\!P}$ distribution is a little flatter than the purity.

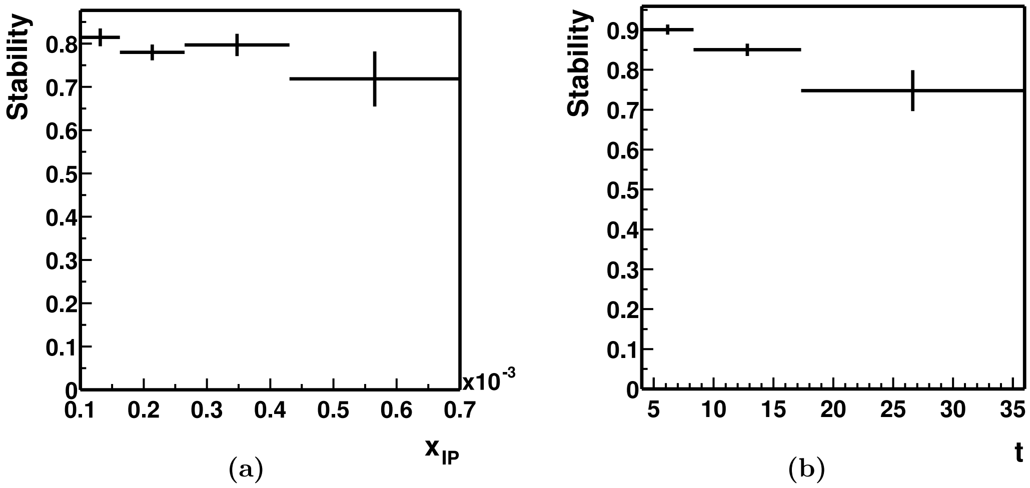

Figure 6.4: The (a) $x_{I\!P}$, and (b) t stabilities.

6.2 Trigger Efficiency

The triggers used to collect data at high energy physics experiments are not necessarily 100% efficient, therefore the efficiency of each trigger should be investigated and corrected for in the measurement of cross sections. The trigger efficiency is measured using an independent subtrigger (or monitor trigger) for each of the two triggers used in the analysis. The electron tagger contribution need not be considered, however, as it well known and accounted for in the treatment of the MC.

The efficiency of a subtrigger s measured using a monitor trigger m in data is given by

$$\varepsilon_s = \frac{N_{m\&\&s}}{N_m} \tag{6.7}$$

where N_m is the number of events passing the monitor trigger and $N_{m\&\&s}$ is the number of events passing both the monitor trigger and the subtrigger being investigated.

The s0 subtrigger consists of `(SPCLe_IET>1 || SPCLe_IET_CEN2)` with veto conditions in addition. The efficiency is calculated using the s71 subtrigger which con-

$E_e > 8$ GeV	$11 < R < 67$cm	$E - p_z > 35$ GeV
$y > 0.05$	Cluster Radius < 4cm	Central Vertex
$Q^2 > 1.25$ GeV^2	$E_{VETO} < 1$ GeV	$\lvert z_{vertex} \rvert < 35$cm
$153^\circ < \theta_e < 176.5^\circ$		SpaCal Fiducial cut

Table 6.1: A summary of the selection of low Q^2 neutral current events used to calculate trigger efficiencies.

sists of (`zVtx_sig_1 && DCRPh_Tc && LAr_BR`). The s50 subtrigger consists of (`eTAG && (SPCLe_IET>1 || SPCLe_IET_CEN2)`) with additional veto conditions. The efficiency of this subtrigger is measured using subtrigger s83 which consists of (`eTAG && zVtx_sig_1 && DCRPh_Tc`). The new trigger elements introduced in the monitor triggers are `zVtx_sig_1`, a significant peak in the z vertex histogram at L1 trigger level, `DCRPh_Tc`, at least 3 masks fired in the central tracking – equating to at least 3 tracks being found in the CTD at trigger level, and `LAr_BR`, a tower above threshold in the LAr validated by a MWPC track. The s83 subtrigger contains the same electron tagger requirement as s50, hence cannot be used to test this part of the s50 subtrigger. However, as previously stated, the acceptance of the 33m electron tagger is well known and accounted for in the MC.

To provide greater statistics the trigger efficiencies were calculated using a sample of low Q^2 neutral current events, rather than signal events. These events have the scattered electron detected in the SpaCal and hence may be used to estimate the triggering of photons by the same subtriggers, as both are based on measuring an electromagnetic cluster in the SpaCal. An event selection based on the inclusive selection used for a 1999 minimum bias measurement of low Q^2 diffraction [53] was used. The cuts are summarised in table 6.1.

The sample of events is briefly compared to a sample of DJANGO MC low Q^2 neutral current events (figure 6.5) to ascertain the quality of events selected. Generally there is a good description of the data by the MC. The intention of this

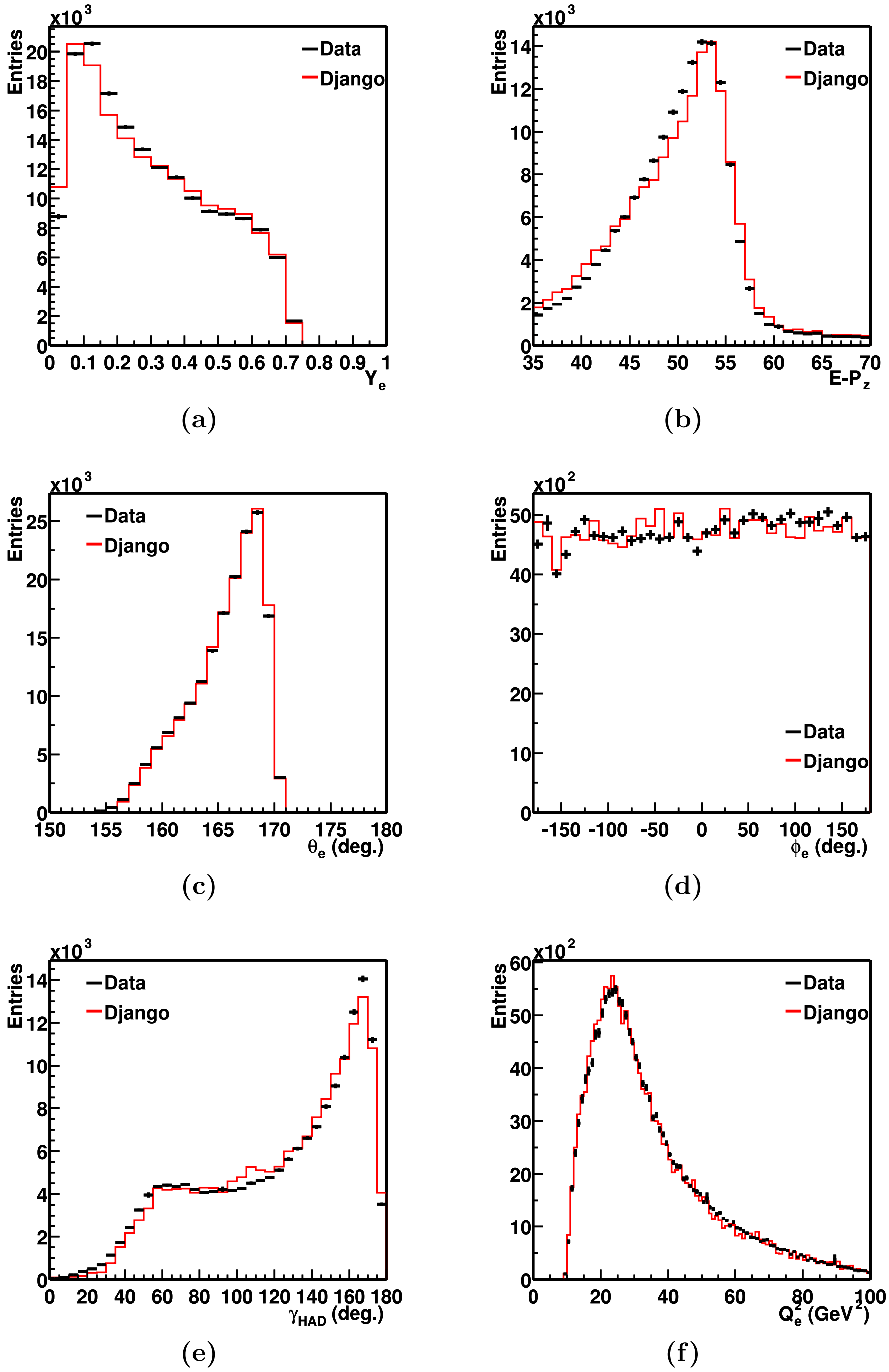

Figure 6.5: The (a) y, (b) $\sum(E - p_z)$, (c) electron theta, (d) electron phi (e) theta angle of the hadronic system and (f) Q^2 distributions for the low Q^2 selection for data (crosses) compared to the prediction from DJANGO (red line).

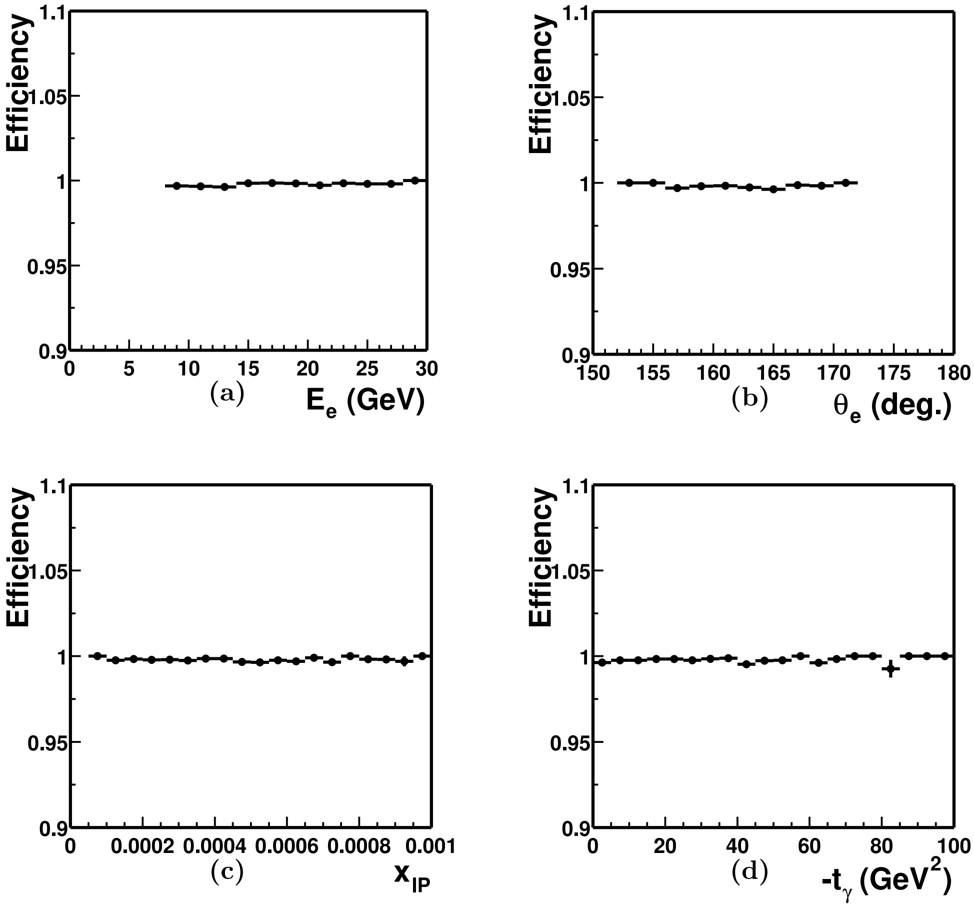

Figure 6.6: The s0 trigger efficiency as a function of (a) energy of the electromagnetic cluster, (b) theta of the electromagnetic cluster, (c) $x_{I\!P}$ and (d) t.

study is not to fully understand the backgrounds to the neutral current process, so the fact that there is good overall agreement between the data and the MC is sufficient.

The trigger efficiencies for the s0 and s50 subtriggers are shown in figure 6.6 and figure 6.7, respectively. The error bars shown are binomial errors. As expected, the trigger efficiencies are consistent with 100% across the full range being considered. Thus no correction is made for trigger efficiencies in the cross section calculation.

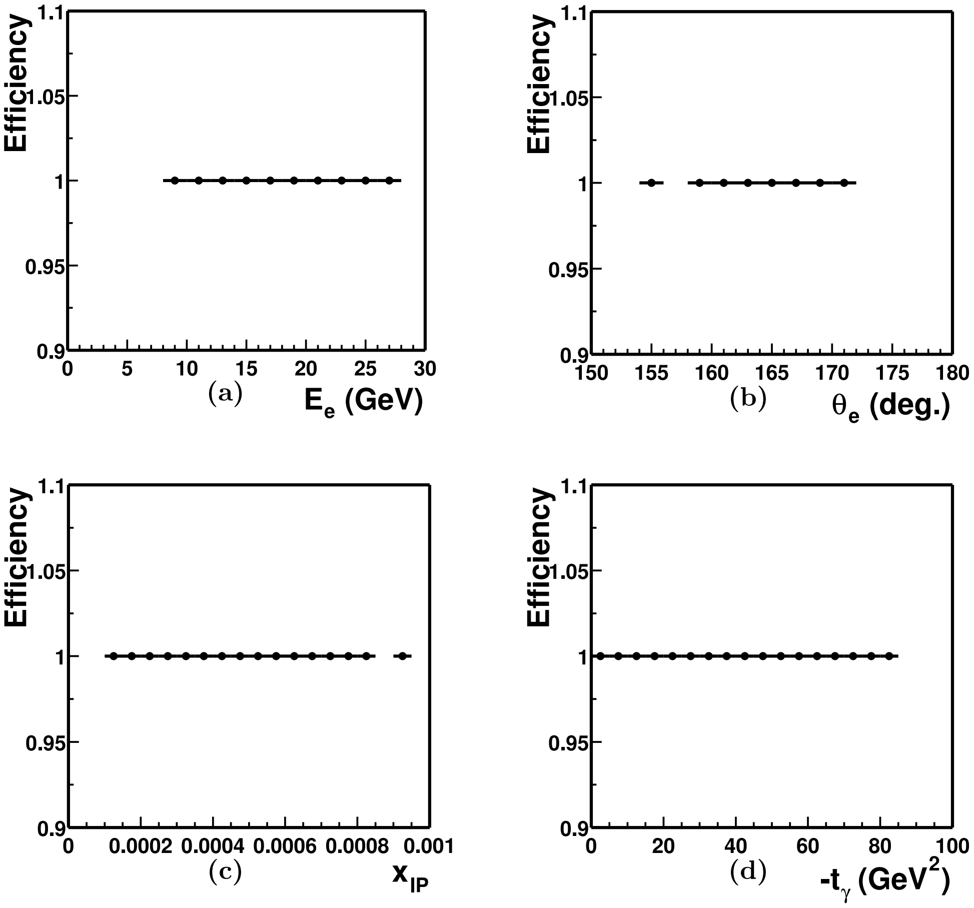

Figure 6.7: The s50 trigger efficiency as a function of (a) energy of the electromagnetic cluster, (b) theta of the electromagnetic cluster, (c) $x_{I\!P}$ and (d) t.

6.3 Evaluation of Errors

The errors on the measured cross sections are split into two contributions – the statistical and systematics errors. The statistical errors are assumed to follow Poisson statistics and, as will be seen, are the dominant errors in the measurement. The systematic errors quantify the systematic uncertainty on quantities measured by the detector and on inputs to the MC model used to simulate the signal process. The systematic errors are considered on a bin-by-bin basis and consist of two types – correlated systematic errors, which affect each bin equally, and uncorrelated errors, which affect each bin independently. The error in each bin was estimated using the MC simulation of signal events. Each quantity in question has its value shifted up by its estimated error and the cross section is recalculated. The quantity is then shifted down by the same error and the cross section recalculated. Half of the difference between the two shifted cross sections is then taken as the systematic error for that quantity. Finally all of the systematic errors are combined in quadrature.

The systematic errors considered are:

- **Photon energy**

  The energy of an electromagnetic cluster measured by the SpaCal is known to an accuracy of $\pm1\%$ [12].

- **Photon angle**

  The theta angle of an electromagnetic cluster measured by the SpaCal is known to an accuracy of ±1mrad [61].

- **LAr energy**

  The hadronic energy scale of the LAr calorimeter is known to an accuracy of $\pm4\%$ [62].

- **ETag 33 energy**

  The energy scale of the 33m electron tagger is known to $\pm1.5\%$ [63].

- **Luminosity**

  The luminosity is measured with an accuracy of $\pm1.5\%$ [25].

- **Noise Subtraction**

  The total four vector of the noise subtracted from the calorimeters is varied by $\pm30\%$ and added into the hadronic final state [55].

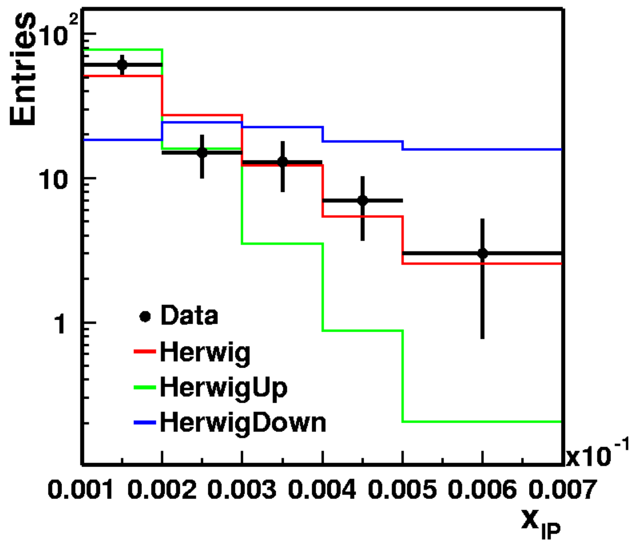

Figure 6.8: The $x_{I\!P}$ distribution for data (crosses) compared to the prediction from HERWIG (red central line). The HerwigUp and HerwigDown lines show the effects of reweighting the $x_{I\!P}$ slope used in the HERWIG MC by $(1/x_{I\!P})^{2.2}$ and $(1/x_{I\!P})^{-2.2}$, respectively, as described in the text.

Only one MC was used to model the signal process and its measurement by the H1 detector. Hence systematic errors were estimated for some of the key distributions used in the model. The MC prediction is weighted by the same form as the slopes in question, but with a new constant determined from the spread of the data points around the measured slopes. This concept is demonstrated in figure 6.3, which shows the $x_{I\!P}$ distribution for data (crosses) compared to the unweighted prediction from the HERWIG MC (red central line). Also shown are the predictions from the HERWIG MC reweighted upwards by $(1/x_{I\!P})^{2.2}$ (HerwigUp) and downwards by $(1/x_{I\!P})^{-2.2}$ (HerwigDown). The two reweighted distributions form an envelope around the data points and hence are used to calculate the systematic error on the $x_{I\!P}$ cross section from the MC model. The systematic errors considered are:

- $x_{I\!P}$ **slope**

  The $x_{I\!P}$ slope was weighted by the form $(1/x_{I\!P})^{\pm a}$ with $a = 2.2$.

- t **slope**

  The t slope was weighted by the form $(1/t)^{\pm b}$ with $b = 2$.

- M_Y **slope**

  The M_Y slope was weighted by the form $(1/M_Y^2)^{\pm c}$ with $c = 0.3$.

Finally, as stated in in section 5.10.4, half of the estimate of the background from inclusive diffraction was assigned to a systematic error on a bin-by-bin basis.

For both the $x_{I\!P}$ and the t cross sections the largest systematic error comes from the subtraction of noise in the LAr, with an average value of $\sim 9\%$. This, however, is still small compared to the statistical errors.

6.4 Photon Flux

Thus far only electron-proton cross sections have been considered. However, due to the $1/Q^4$ term in the differential ep cross section, the cross section at HERA is dominated by the interaction of near mass shell photons with protons. Thus HERA may be considered a γp collider. Therefore the final ingredient need for the cross section is to factor out the flux of photons from the electron-photon vertex, giving a relationship between ep and γp cross sections

$$\frac{d^2\sigma_{ep}(s)}{dQ^2dy} = \sigma_{\gamma p}(ys)F(y, Q^2) \tag{6.8}$$

where $F(y, Q^2)$ is the photon flux factor. This is calculable for quasi-real photons using the Weizsäcker-Williams approximation [64]

$$F(y, Q^2) = \frac{\alpha_{em}}{2\pi Q^2}\left(\frac{1 + (1-y)^2}{y} - \frac{2(1-y)}{y}\frac{Q^2_{min}}{Q^2}\right) \tag{6.9}$$

where

$$Q^2_{min} = \frac{(m_e y)^2}{1-y} \tag{6.10}$$

The measured distributions of both $x_{I\!P}$ and t show no dependence on y within errors over the measured ranges. Therefore a constant flux factor is applied to all bins of the cross sections. When integrated over the kinematic range $0.3 < y < 0.6$ and $Q^2 < 0.01$ GeV^2 the flux factor is

$$f = \int F(y, Q^2) dy dQ^2 = 9.66 \times 10^{-3} \tag{6.11}$$

Chapter 7

Results and Discussion

This chapter presents the final cross sections as measured using the techniques described in chapter 6. The cross sections are presented at the level of stable hadrons and in the kinematic region described in chapter 5.9. The cross sections are compared to the LLA BFKL prediction from the HERWIG Monte Carlo generator [52].

7.1 The $x_{I\!P}$ Cross Section

Figure 7.1 shows the γp cross section differentially in $x_{I\!P}$. The inner error bars show the statistical error and the outer error bars the statistical and systematic errors added in quadrature. The systematic errors are small compared to the statistical errors. The data are compared to the LLA BFKL prediction for a choice of $\overline{\alpha_s} = 0.17$. The prediction is normalised to the measured data cross section, as within the LLA BFKL calculation there is an uncertainty in normalisation, even for a fixed choice of $\overline{\alpha_s}$ [65].

Figure 7.2 shows the γp cross section differentially in $x_{I\!P}$ compared to a fit of the form $A(1/W^2)(1/x_{I\!P})^n$. A mean value of $W = 206.1$ GeV is used for the fit. The

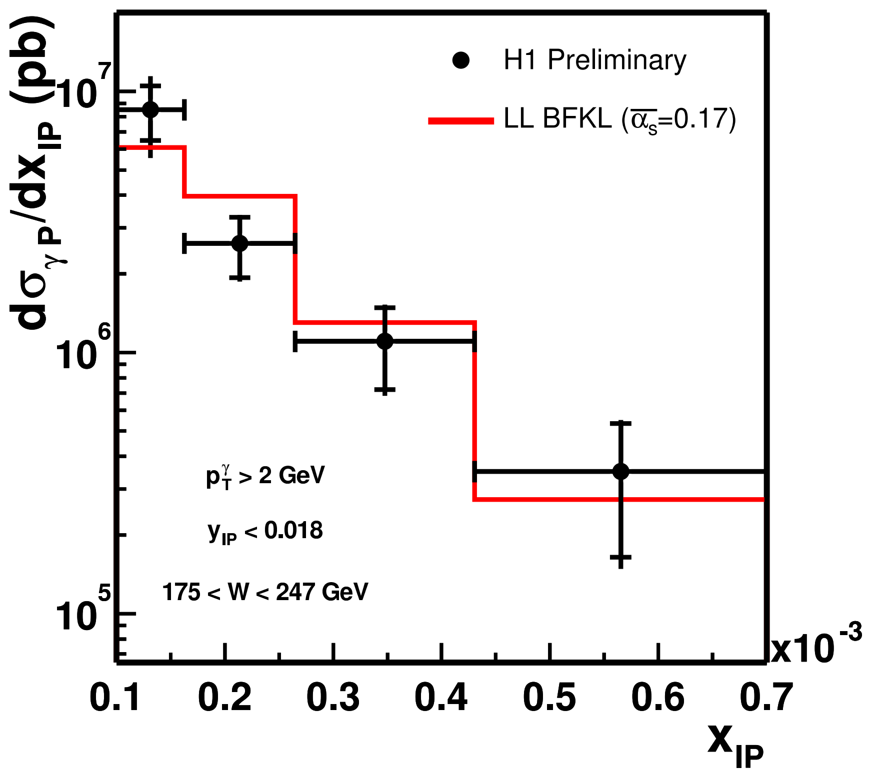

Figure 7.1: The γp cross section differential in $x_{I\!P}$. The inner error bars show the statistical error and the outer error bars show the statistical and systematic error bars added in quadrature. The line shows the LLA BFKL prediction from the HERWIG event generator for a choice of $\overline{\alpha_s} = 0.17$, as described in the text.

form of the fit is motivated by the prediction that the differential $x_{I\!P}$ cross section varies as

$$\frac{d\sigma_{\gamma p}}{dx_{I\!P}} \sim \frac{1}{W^2}\left(\frac{1}{x_{I\!P}}\right)^{2\omega_0+2} \tag{7.1}$$

where $\omega_0 = (3\overline{\alpha_s}/\pi)4\ln 2$ [52]. Thus the fit yields values of the pomeron intercept, $\alpha(0) = 1 + \omega_0$, and $\overline{\alpha_s}$ which may be compared to other measurements of diffractive processes. The data shown in figure 7.2 are described by the values $n = 2.99 \pm 0.24(\text{stat.}) \pm 0.03(\text{sys.})$ and $A = 0.99 \pm 2.07(\text{stat.}) \pm 0.05(\text{sys.})$, with a $\chi^2/NDF = 3.26/2$. This corresponds to a pomeron intercept of

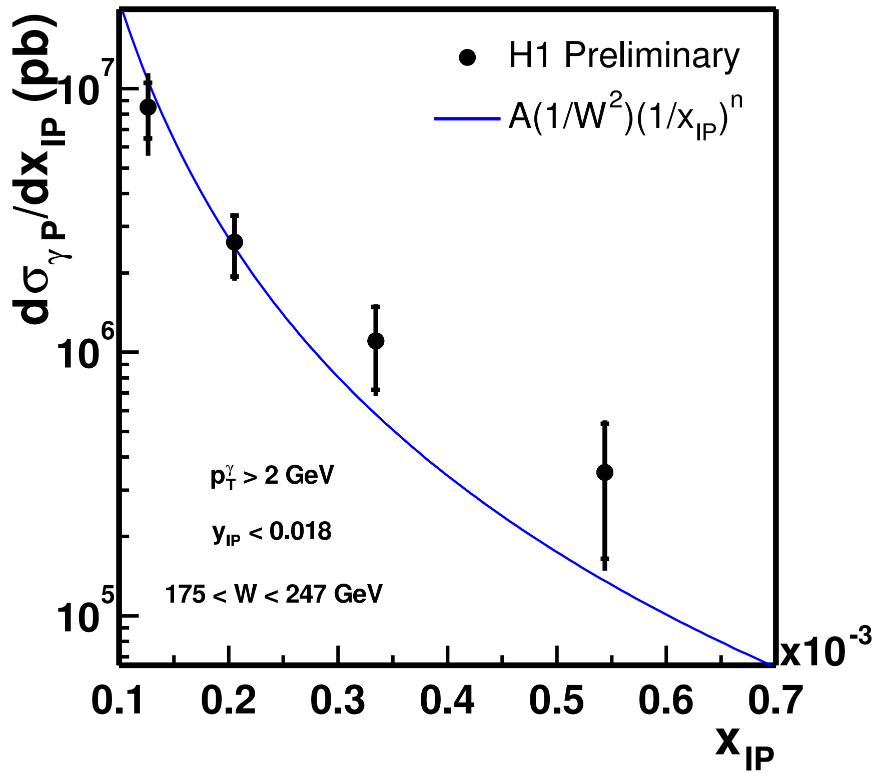

Figure 7.2: The γp cross section differential in $x_{I\!P}$ compared to a fit of the form $A(1/W^2)(1/x_{I\!P})^n$, with $n = 2.99 \pm 0.24(\text{stat.}) \pm 0.03(\text{sys.})$. The inner error bars show the statistical error and the outer error bars show the statistical and systematic error bars added in quadrature.

$\alpha(0)^{FIT} = 1.50 \pm 0.12(\text{stat.}) \pm 0.01(\text{sys.})$ and $\overline{\alpha_s}^{FIT} = 0.187 \pm 0.045(\text{stat.}) \pm 0.005(\text{sys.})$.

7.2 The t Cross Section

Figure 7.3 shows the γp cross section differentially in t, the squared four momentum transfer between the incident photon and the proton. The inner error bars show the statistical error and the outer error bars the statistical and systematic errors added in

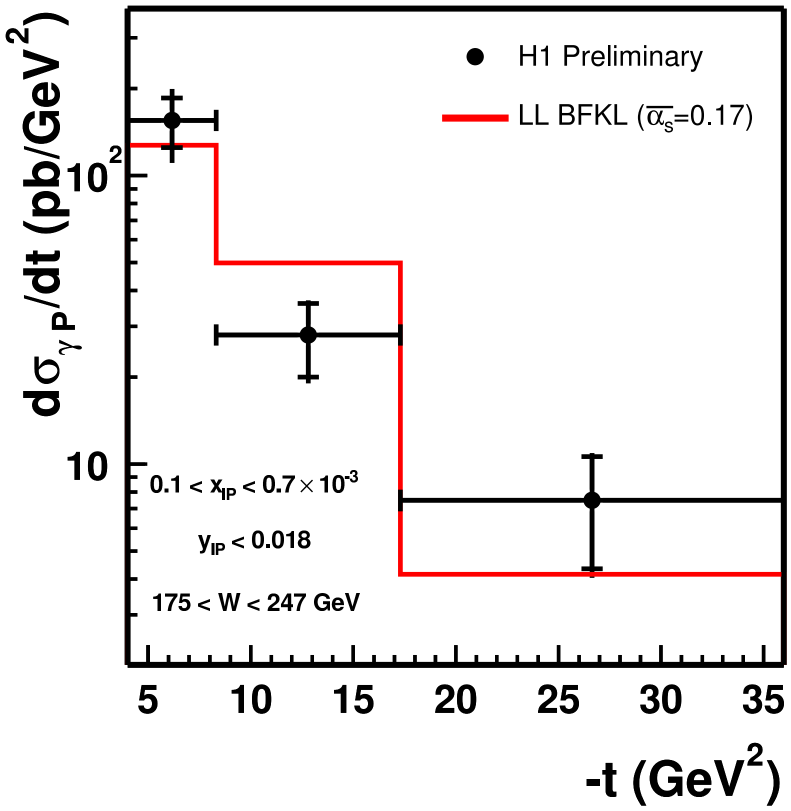

Figure 7.3: The γp cross section differential in t. The inner error bars show the statistical error and the outer error bars show the statistical and systematic error bars added in quadrature. The line shows the LLA BFKL prediction from the HERWIG event generator for a choice of $\overline{\alpha_s} = 0.17$, as described in the text.

quadrature. The systematic errors are again small compared to the statistical errors. The data are compared to the LLA BFKL prediction for a choice of $\overline{\alpha_s} = 0.17$, with the prediction normalised to the measured data cross section.

Figure 7.4 shows the γp cross section differentially in t compared to a fit of the form $A\,|t|^{-n}$. The data are described by the values
$A = (6.22 \pm 5.8(\text{stat.}) \pm 3.7(\text{sys.})) \times 10^3$ and $n = 2.14 \pm 0.41(\text{stat.}) \pm 0.22(\text{sys.})$, with a $\chi^2/NDF = 0.223/1$.

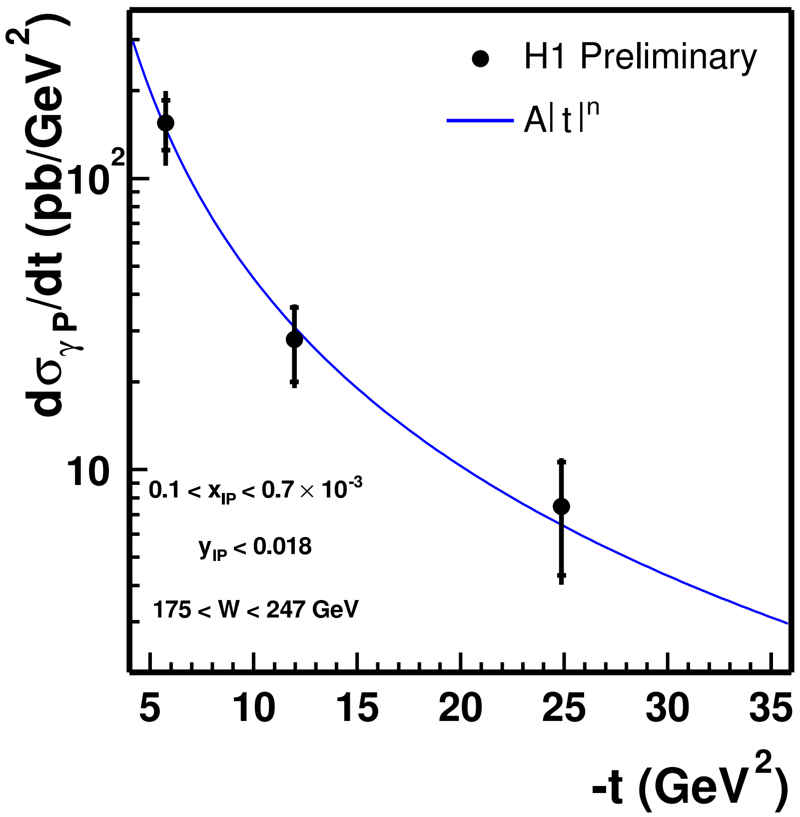

Figure 7.4: The γp cross section differential in t compared to a fit of the form $A\,|t|^{-n}$ with $A = (6.22 \pm 5.8(\mathrm{stat.}) \pm 3.7(\mathrm{sys.})) \times 10^3$ and $n = 2.14 \pm 0.41(\mathrm{stat.}) \pm 0.22(\mathrm{sys.})$. The inner error bars show the statistical error and the outer error bars show the statistical and systematic error bars added in quadrature.

7.3 Discussion

The observation of the $x_{I\!P}$ differential cross section rising steeply with $1/x_{I\!P}$ is an indication of the diffractive nature of the cross section measured. This behaviour is reproduced in the LLA BFKL prediction which does a good job of describing the data. The normalisation uncertainty within the LLA BFKL calculation, even for a fixed $\overline{\alpha_s}$, allows the normalisation of each prediction to be varied. The prediction with $\overline{\alpha_s} = 0.17$ describes the $x_{I\!P}$ cross section reasonably. This is seen

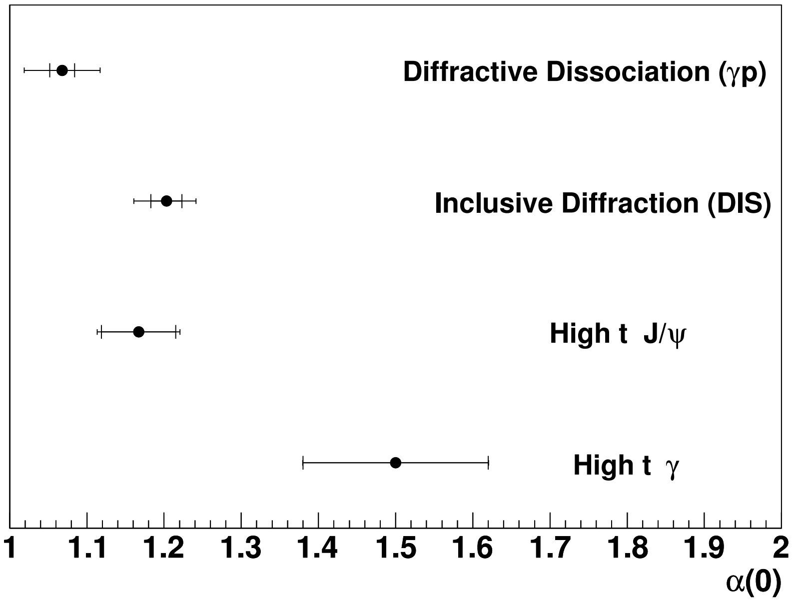

Figure 7.5: The value of the pomeron intercept, $\alpha(0)$, from this analysis compared to those obtained from diffractive dissociation [47], inclusive diffraction [46] and the diffractive photoproduction of J/ψ mesons at large t [49] as measured by H1. The inner error bars show the statistical error and the outer error bars show the statistical and systematic error bars added in quadrature.

in the value of $\overline{\alpha_s}^{FIT} = 0.187 \pm 0.045(\text{stat.}) \pm 0.005(\text{sys.})$ obtained from the fit to the data. The value of $\overline{\alpha_s}^{FIT}$ obtained is similar to the value of $\overline{\alpha_s} = 0.18$ used in recent H1 measurements [48, 49]. Additionally, figure 7.5 shows the measured value of the pomeron intercept $\alpha(0)^{FIT}$ compared to measurements of the pomeron intercept in different diffrative processes. The measured value of the pomeron intercept $\alpha(0)^{FIT} = 1.50 \pm 0.12(\text{stat.}) \pm 0.01(\text{sys.})$ is similar to the value of $\alpha(0) = 1.167 \pm 0.048(\text{stat.}) \pm 0.024(\text{sys.})$ as measured by H1 in the diffractive photoproduction of J/ψ mesons at large t [49]. However, it should be noted that the value of $\overline{\alpha_s}^{FIT}$ and hence the pomeron intercept measured here is larger than those in the other H1 measurements, corresponding to one of the steepest energy dependences measured in diffraction at HERA. Both the values of $\alpha(0)^{FIT}$ from this measurement and from the J/ψ are larger than that found from the total pp and $p\bar{p}$ cross sections. It should also be noted that the form of equation 7.1 is found at constant W and t, whereas the fit is performed on the measured cross section where no account has been made for any dependence. The measurement is made over a somewhat small range of W, but over a large range in t.

The description of the t differential cross section is perhaps a little worse than the description of the $x_{I\!P}$ differential cross section, although it is still reasonably described. The fit of the form $A\,|t|^{-n}$ with $n = 2.14 \pm 0.41(\text{stat.}) \pm 0.22(\text{sys.})$ describes the data well, but is a little shallower than the value of
$n = 3.78 \pm 0.17(\text{stat.}) \pm 0.06(\text{sys.})$ as measured by H1 in the diffractive photoproduction of J/ψ mesons at large t [49].

There may be important contributions from higher order effects in BFKL calculations beyond the LLA [65], so perhaps it is a little soon to make strong statements about the agreement with the data. However, the measured $x_{I\!P}$ cross section shows a steep rise with energy, which is a striking result, and there is a good overall agreement between the data and the LLA BFKL predictions.

Chapter 8

Summary

The process $\gamma p \to \gamma Y$, where the final state photon carries a large transverse momentum and is well separated from the proton dissociative system Y, has been measured, using the H1 detector at HERA, for the first time. The process provides a uniquely clean test of the underlying QCD dynamics of the diffractive exchange and is compared to a LLA BFKL prediction for the process. The measurement is complementary to the diffractive production of vector mesons and measurements of the rapidity gaps between high transverse momentum dijets, however the presence of a photon in the final state offers some advantages. In particular the absence of a vector meson wavefunction allows the entire hard scatter to be calculated and the lack of a diffractively produced jet helps to reduce the effects of secondary interactions closing the rapidity gap.

Cross sections are presented differentially in the appropriate energy variable $x_{\mathbb{P}}$ and the square of the four momentum transfer of the diffractive exchange t. A full systematic analysis has been carried out, however the statistical errors dominate the error on the measured cross sections. The cross sections are compared to a LLA BFKL calculation as implemented in the HERWIG event generator. A reasonable description of the two cross sections is found. In particular, a steep rise with $1/x_{\mathbb{P}}$

is observed – a classic signature of a diffractive exchange.

A fit of the form $A(1/W^2)(1/x_{I\!P})^n$ performed on the $x_{I\!P}$ cross section yields a pomeron intercept of $\alpha(0)^{FIT} = 1.50 \pm 0.12(\text{stat.}) \pm 0.01(\text{sys.})$, corresponding to $\overline{\alpha_s}^{FIT} = 0.187 \pm 0.045(\text{stat.}) \pm 0.005(\text{sys.})$, similar to the measurement of high t diffractive J/ψ production and the value of $\overline{\alpha_s}$ used in the measurement of gaps between jets. However, the values are a little higher and incompatible within the errors and hence correspond to one of the steepest energy slopes measured in diffraction at HERA. A fit of the form $A\,|t|^{-n}$ yields $n = 2.14 \pm 0.41(\text{stat.}) \pm 0.22(\text{sys.})$, corresponding to a shallower t cross section than seen for the high t diffractive J/ψ production.

As seen from the presented cross sections, the measurement is statistically limited. However, with the upgrade of the HERA accelerator to provide greater luminosity coming to fruition, this situation should be improved in the future. The extra statistics will improve accuracy in the hard to reach high $x_{I\!P}$ and t bins, as well as allowing finer binning to be used for the cross sections. Finally, it would be interesting to observe the W cross section, which at this point is not presented. The upgrade of H1 will also allow new ranges of W to be accessed, due to the taggers along the electron direction being moved.

Bibliography

[1] H1 Collaboration; I. Abt *et al.*, *The H1 Detector at HERA*, NIM, **A386** (1997) 310; 348.

[2] J. Burger *et al.*, *The Central Jet Chamber of the H1 Experiment*, NIM, **A279** (1989) 217.

[3] S. Egli *et al.*, *The Central–Inner Z–Drift Chamber of the H1 Experiment*, NIM, **A283** (1989) 487.

[4] K. Müller *et al.*, *Construction and Performance of a Thin Cylindrical Multiwire Proportional Chamber with Cathode Pad Readout for the H1 Experiment*, NIM, **A312** (1992) 457.

[5] S. Burke *et al.*, *Track finding and fitting in the H1 forward track detector*, Nucl. Instrum. Meth. A **373** (1996) 227.

[6] H1 Collaboration; I. Abt *et al.*, *Technical Proposal for the Upgrade of the Backward Region of the H1 Detector*, DESY Internal Report, **PRC-93-02**.

[7] D. Pitzl *et al.*, *The H1 silicon vertex detector*, Nucl. Instrum. Meth. A **454**, 334 (2000).

[8] W. Eick *et al.*, *Development of the H1 backward silicon strip detector*, Nucl. Instrum. Meth. A **386** (1997) 81.

[9] H1 Calorimeter Group; B. Andrieu *et al.*, *The H1 Liquid Argon Calorimeter System*, NIM, **A336** (1993) 460.

[10] H1 Calorimeter Group; B. Andrieu *et al.*, *Beam Tests and Calibration of the H1 Liquid Argon Calorimeter with Electrons*, NIM, **A350** (1994) 57.

[11] H1 Calorimeter Group; B. Andrieu *et al.*, *Results from Pion Calibration Runs for the H1 Liquid Argon Calorimeter and Comparisons with Simulations*, NIM, **A336** (1993) 499.

[12] H1 SpaCal Group; R. D. Appuhn *et al.*, *The H1 Lead/Scintillating–fibre Calorimeter*, NIM, **A386** (1997) 397.

[13] H1 SpaCal Group; T. Nicholls *et al.*, *Performance of an Electromagnetic Lead/Scintillating–fibre Calorimeter for the H1 Detector*, NIM, **A374** (1996) 149.

[14] H1 SpaCal Group; R. D. Appuhn *et al.*, *H1 Backward Upgrade with a SPACAL Calorimeter: The Hadronic Section*, DESY Report, **DESY-96-013**.

[15] H1 SpaCal Group; R. D. Appuhn *et al.*, *Hadronic Response and e/π–Separation with the H1 Lead/Fiber Calorimeter*, NIM, **A382** (1996) 395.

[16] H1 Collaboration; T. Ahmed *et al.*, *The H1 Forward Muon Spectrometer*, NIM, **A340** (1994) 304.

[17] H1 Collaboration, *Luminosity Measurement in the H1 Experiment at HERA*, contributed paper to *ICHEP96, Warsaw 1996*, **ICHEP96pa17-026**.

[18] H. Bethe and W. Heitler, *On the Stopping of Fast Particles and on the Creation of Positive Electrons*, Proc. Roy. Soc. Lond. **A146** (1934) 83.

[19] E. Elsen, *The H1 Trigger and Data Acquisition*, contributed paper to *International Symposium on Electronic Instrumentation in Physics, Dubna 1991*,

H1 Internal Note, **H1-IN-262 (01/1993)**;
F. Sefkow *et al.*, *Experience with the First Level trigger of H1*, contributed paper to *The 1994 IEEE Nuclear Science Symposium, Virginia 1994*, H1 Internal Note, **H1-IN-407 (11/1994)**.

[20] J. C. Bizot *et al.*, *Status of Simulation for a Topological Level 2 Trigger*, H1 Internal Note, **H1-IN-212 (02/1992)**;
J. C. Bizot *et al.*, *Strategy Studies for the H1 Topological L2–Trigger (L2TT)*, H1 Internal Note, **H1-IN-508 (01/1997)**.

[21] J. H. Köhne *et al.*, *Realization of a Second Level Neural Network Trigger for the H1 experiment at HERA*, H1 Internal Note, **H1-IN-509 (01/1997)**.

[22] G. Marchesini, B. R. Webber, G. Abbiendi, I. G. Knowles, M. H. Seymour and L. Stanco, *HERWIG: A Monte Carlo event generator for simulating hadron emission reactions with interfering gluons. Version 5.1 - April 1991*, Comput. Phys. Commun. **67** (1992) 465.

[23] R. Brun *et al.*, *GEANT3 User's Guide*, **CERN-DD/EE-84-1**.

[24] F. Halzen and A. Martin, *Quarks and Leptons*, Wiley (1984).

[25] C. Adloff *et al.* [H1 Collaboration], *Measurement and QCD analysis of neutral and charged current cross sections at HERA*, submitted to Eur. Phys. J. **C**.

[26] E. D. Bloom *et al.*, *High-Energy Inelastic E P Scattering At 6-Degrees And 10-Degrees*, Phys. Rev. Lett. **23** (1969) 930.
M. Breidenbach *et al.*, *Observed Behavior Of Highly Inelastic Electron - Proton Scattering*, Phys. Rev. Lett. **23** (1969) 935.
J. I. Friedman and H. W. Kendall, *Deep Inelastic Electron Scattering*, Ann. Rev. Nucl. Part. Sci. **22** (1972) 203.

[27] J. D. Bjorken, *Inequality for Backward Electron–Nucleon and Muon–Nucleon Scattering at High Momentum Transfer*, Phys. Rev. **163** (1967) 1767.

[28] R. Feynman, *Very High Energy Collisions of Hadrons*, Phys. Rev. Lett. **23** (1969) 1415.

J. D. Bjorken and E. Paschos, *Inelastic Electron–Proton and γ–Proton Scattering and the Structure of the Nucleon*, Phys. Rev. **185** (1969) 1975.

[29] C. G. Callan and D. J. Gross, *High-Energy Electroproduction And The Constitution Of The Electric Current*, Phys. Rev. Lett. **22** (1969) 156.

[30] R. E. Taylor, *Deep inelastic scattering: The Early years*, Rev. Mod. Phys. **63** (1991) 573.

H. W. Kendall, *Deep inelastic scattering: Experiments on the proton and the observation*, Rev. Mod. Phys. **63** (1991) 597.

J. I. Friedman, *Deep inelastic scattering: Comparisons with the quark model*, Rev. Mod. Phys. **63** (1991) 615.

[31] Y. L. Dokshitzer, *Calculation of the Structure Functions for Deep Inelastic Scattering and e^+ and e^- Annihilation by Perturbation Theory in Quantum Chromodynamics*, Sov. Phys. JETP **46** (1977) 641;

V. N. Gribov and L. N. Lipatov, *Deep Inelastic ep Scattering in Perturbation Theory*, Sov. J. Nucl. Phys. **15** (1972) 438 and 675.

G. Altarelli and G. Parisi, *Asymptotic Freedom in Parton Language*, Nucl. Phys. **B126** (1977) 298.

[32] E. A. Kuraev, L. N. Lipatov and V. S. Fadin, *The Pomeranchuk Singularity in Non–Abelian Gauge Theories*, Sov. Phys. JETP **45** (1977) 199;

I. I. Balitsky and L. N. Lipatov, *The Pomeranchuk Singularity in Quantum Chromodynamics*, Sov. J. Nucl. Phys. **28** (1978) 822.

[33] A. Donnachie and P. V. Landshoff, *Small x: Two pomerons!*, Phys. Lett. B **437** (1998) 408.

[34] J. R. Forshaw and D. A. Ross, *Quantum Chromodynamics And The Pomeron*, Cambridge University Press (1997).

[35] G. F. Chew and S. C. Frautschi, *Principle Of Equivalence For All Strongly Interacting Particles Within The S Matrix Framework*, Phys. Rev. Lett. **7** (1961) 394.
G. F. Chew and S. C. Frautschi, *Regge Trajectories And The Principle Of Maximum Strength For Strong Interactions*, Phys. Rev. Lett. **8** (1962) 41.

[36] A. C. Irving and R. P. Worden, *Regge Phenomenology*, Phys. Rept. **34** (1977) 117.

[37] A. V. Barnes *et al.*, *Pion Charge Exchange Scattering At High-Energies*, Phys. Rev. Lett. **37** (1976) 76.

[38] I. Y. Pomeranchuk, Sov. Phys. **3** (1956) 306. L. B. Okun and I.Y. Pomeranchuk, Sov. Phys. JETP **3** (1956) 307.

[39] L. F. Foldy and R. F.Peierls, Phys. Rev. **130** (1963) 1585.

[40] A. Donnachie and P. V. Landshoff, *Total cross-sections*, Phys. Lett. B **296** (1992) 227

[41] S. Aid *et al.* [H1 Collaboration], *Measurement of the Total Photon Proton Cross Section and its Decomposition at 200 GeV Centre of Mass Energy*, Z. Phys. C **69** (1995) 27

[42] M. Derrick *et al.* [ZEUS Collaboration], *Observation of events with a large rapidity gap in deep inelastic scattering at HERA*, Phys. Lett. B **315** (1993) 481.
T. Ahmed *et al.* [H1 Collaboration], *Deep inelastic scattering events with a large rapidity gap at HERA*, Nucl. Phys. B **429** (1994) 477.

[43] J. C. Collins, *Proof of factorization for diffractive hard scattering*, Phys. Rev. D **57** (1998) 3051 [Erratum-ibid. D **61** (2000) 019902]

[44] G. Ingelman and P. E. Schlein, *Jet Structure In High Mass Diffractive Scattering*, Phys. Lett. B **152** (1985) 256.

[45] H1 Collaboration *Measurement of the Inclusive Cross Section for Diffractive Deep Inelastic Scattering at High Q^2*, Conf. paper 090, Intern. Europhysics Conf. on HEP, EPS03, Aachen (2003).

[46] C. Adloff *et al.* [H1 Collaboration], *Inclusive measurement of diffractive deep-inelastic e p scattering*, Z. Phys. C **76** (1997) 613

[47] C. Adloff *et al.* [H1 Collaboration], *Diffraction dissociation in photoproduction at HERA*, Z. Phys. C **74** (1997) 221

[48] C. Adloff *et al.* [H1 Collaboration], *Energy flow and rapidity gaps between jets in photoproduction at HERA*, Eur. Phys. J. C **24** (2002) 517

[49] A. Aktas *et al.* [H1 Collaboration], *Diffractive photoproduction of J/psi mesons with large momentum transfer at HERA*, Phys. Lett. B **568** (2003) 205

[50] D. Y. Ivanov and M. Wusthoff, *Hard diffractive photon proton scattering at large t*, Eur. Phys. J. C **8** (1999) 107

[51] N. G. Evanson and J. R. Forshaw, *Diffractive photon production in gamma p and gamma gamma interactions*, Phys. Rev. D **60** (1999) 034016

[52] B. E. Cox and J. R. Forshaw, *Diffractive production of high-p(T) photons at HERA*, J. Phys. G **26** (2000) 702

[53] C. Johnson *A Measurement of the Diffractive Proton Structure Function $F_2^{D(3)}$ at Low Q^2 at the H1 Experiment at HERA*, Ph.D. thesis, University of Birmangham (2002).

[54] C. Adloff *et al.* [H1 Collaboration], *Measurement of neutral and charged current cross sections in electron proton collisions at high Q^2*, Eur. Phys. J. C **19** (2001) 269

[55] B. Heinemann, *Measurement of Charged Current and Neutral Current Cross Sections in Positron-Proton Collisions at sqrt(s)=300 GeV*, Dissertation, Fachberich Physik der Universität Hamburg (1999).

[56] V. V. Arkadov, Dissertation -*Measurement of the Deep-Inelastic ep Scattering Cross Section using the Backward Silicon Tracker at the H1 Detector at HERA* Mathematisch-Naturwissenschaftlichen Fakultät I der Humboldt-Universität zu Berlin.

[57] B. List and A. Mastroberardino, *Diffvm: A Monte Carlo Generator For Diffractive Processes In E P Scattering*, *Prepared for Workshop on Monte Carlo Generators for HERA Physics (Plenary Starting Meeting), Hamburg, Germany, 27-30 Apr 1998*

[58] M. Derrick *et al.* [ZEUS Collaboration], *Measurement of elastic omega photoproduction at HERA*, Z. Phys. C **73** (1996) 73
J. Breitweg *et al.* [ZEUS Collaboration], *Measurement of exclusive omega electroproduction at HERA*, arXiv:hep-ex/0006013.

[59] F. W. Bopp, R. Engel and J. Ranft, *Rapidity gaps and the PHOJET Monte Carlo*, arXiv:hep-ph/9803437.

[60] S. Chekanov *et al.* [ZEUS Collaboration], *Measurement of proton dissociative diffractive photoproduction of vector mesons at large momentum transfer at HERA*, Eur. Phys. J. C **26** (2003) 389

[61] H1 Collaboration *Inclusive $D^{\star\pm}$ Meson and Associated Dijet Production in Deep-Inelastic Scattering*, Conf. paper 098, Intern. Europhysics Conf. on HEP, EPS03, Aachen (2003).

[62] A. Aktas *et al.* [H1 Collaboration], *Inclusive dijet production at low Bjorken-x in deep inelastic scattering*, Submitted to Eur.Phys.J.C, arXiv:hep-ex/0310019.

[63] Paul Newman. Private Communication

[64] C. F. von Weizsäcker, *Radiation Emitted In Collisions Of Very Fast Electrons*, Z. Phys. **88** (1934) 612.
E. J. Williams, *Nature Of The High-Energy Particles Of Penetrating Radiation And Status Of Ionization And Radiation Formulae*, Phys. Rev. **45** (1934) 729.

[65] B. Cox, J. Forshaw and L. Lonnblad, "Hard colour singlet exchange at the Tevatron," JHEP **9910** (1999) 023

Acknowledgements

The end is nearing and so, as is traditional, the credits should begin to roll. Many people have contributed not only to my doctorate and this thesis, but to other areas outside of my studies (I believe that there is an outside, although presently I don't have any firm evidence). These people are to be warmly and genuinely thanked, perhaps with a witty quip along the way, in the following partially ordered stream of consciousness.

To begin with there are people from Manchester who without them this thesis would not exist. Firstly my supervisor, Robin Marshall, who gave me the freedom to pursue an interesting project for my PhD, but also gave input at just the right places. Secondly, Fred Loebinger, who was instrumental in convincing a wet behind the ears college student to come to Manchester in the first place and has always been helpful ever since. Brian Cox must be thanked for his knowledge, drive and enthusiasm, which without the work here would be considerably poorer. Thanks also to Angela Wyatt who provided help in the early days. At H1, thanks should also go to Paul Newman and the members of the Diffraction group, who I hope haven't developed too many grey hairs. Finally thanks should definitely go out to Nick Malden for saying the right thing at the right time and keeping a good head when those around him (well, me) were losing theirs.

Hamburg is a particularly fine city, but was made even better by the people who I've met during my time there. Some were met at DESY, some in the big world outside, but, as is often the case, many are from the fuzzy area in between. No attempt is made to separate the two in the following unordered list. Dave South (owh), Paul Laycock (one bird man), Ethan-Etienne Woehrling (especially for learning the rules of rugby and the interesting banter that came from that and other random sources), Oliver Henshaw (water tower), Matt Lightwood, Yves Flemming, Andy Mehta, Eram Rizvi, Paul Thompson, Alex Tapper, Eileen Heaphy, James Ferrando, John Lozides, Steve Hanlon, Jo Hamilton and Alexandra Hachmeister (for making the learning of the vagaries of the German language as fun as possible).

There are also people who I left back in Blighty while I had the fortune to come overseas. Firstly in the particle group, Simon Dean (who's been there since the very start at Manchester) and Andy Lyon (white board skills). Thanks also to Kieran Flanagan for the hospitality, Sean Calvert and the Laser Girls. Slightly further afield are the Lewes boys – Chris Moore, Dan Childs, Sam Higton, Ian Harrison, Oliver Maxwell, Dan Wilson, Phil Rowland and Rene Frank – the Harveys tasted sweeter with you. Also to MJ, JL, JR, JW, RH and the others for bringing Bill back home.

Finally, many thanks go to my family – Mum, Dad and Lynsey – for the love, support and encouragement over the years.